Óbuda University

PhD Thesis

New Soft Computing-based Methods in Sensor Fusion and Control: Applications on a Real Mechatronic System

by

Ákos Odry

Supervisor:

Prof. Dr. Róbert Fullér

Applied Informatics and Applied Mathematics Doctoral School

Budapest, 2020

Members of the Defense Committee:

Members of the Comprehensive Examination Committee:

Date of the Defense:

Abstract

The performance of feedback control systems depends on two important algorithms. On one hand, measurements are collected of system dynamics based on sensor data and a state observer algorithm is executed to obtain an estimate of such system states that cannot be determined based on direct observations. This **state estimator algorithm** is the basis in many control engineering applications, since its output (system state estimate) is necessary to solve the control system design problem, i.e., the stabilization of the system around a desired state. As a result, the state estimator is required to provide both reliable and smooth results and thereby its performance directly influences the overall closed-loop dynamics. On the other hand, the **control algorithm** itself determines the performance of the feedback system. This algorithm should be able to satisfy all the essential control objectives based on both the observed and estimated system states. Moreover, the quality of regulation plays an important role, in which robustness against both parameter uncertainties and measurement noises is examined, as well as, smooth control action is addressed. The resultant control action can contribute to high-quality reference tracking, energy-efficient drive characteristics and/or protective (e.g., jerk-free) regulation, which are important aspects in the control of nowadays electro-mechanical systems (robots). In my research work, I analyzed the performance of the preceding algorithms and developed novel soft computing-based techniques to enhance the performance of both state estimation and control. The system to be discussed and controlled is a real wheeled mobile pendulum system, which is a simple two-wheeled mechatronic construction characterized by challenging control problems, such as underactuated, unstable and nonlinear dynamics.

The first group of theses addresses the control system design problem and investigates soft computing-based techniques to enhance the performance of control strategies. First, the realistic mathematical model of the plant is determined and verified based on measurement results of the real system behavior. This realistic model enables the consistent elaboration of stabilizing control strategies, testing of closed-loop dynamics, and the optimization of control parameters. As a result, a novel 8-dimensional mathematical model of wheeled mobile pendulum systems is obtained, which includes both the mechanical nonlinearities and motor dynamics. Then, linear and fuzzy logic-based control strategies are established for the stabilization of the unstable system and the initial performance of these controllers is determined based on both simulation and implementation results. In this stage of development process, the control strategies are designed and tuned heuristically based on the observations related to system dynamics. The development of performance maximizing approaches and the evaluation of the achievable control performances form the next step of the investigation. The quality of the realized control solutions is defined based on transient responses and different error integral formulas. Then, the numerical optimization of control parameters is outlined, where the enhancement of control solutions is realized via the minimization of the quality index (fitness or cost function). This optimization problem is elaborated in four main steps. First, an easily parameterized fuzzy logic control structure is realized in MATLAB/Simulink environment. Second, a complex fitness function is formulated for system dynamics qualification, which evaluates the reference tracking

performance for planar motion, the oscillation of the inner body of the robot, and the energy efficiency of the implemented controllers. Third, the application of particle swarm optimization algorithm is elaborated with the aim to obtain the optimal possible controller parameters. Fourth, the achieved control performances are evaluated and a comparison of optimized linear and fuzzy control strategies is given. This investigation results in a novel protective-type fuzzy logic controller, which provides nonlinear control action based on the sampled current consumption. The structure of the this controller enables to both achieve fast reference tracking dynamics and suppress (limit) the current peaks and jerks in the electro-mechanical parts (motor drive system) of the robot.

The second group of theses deals with the enhancement of state (attitude) estimation performance and derives novel soft computing-based adaptive methods to provide reliable attitude estimates even in dynamic situations. First, the Kalman filter as state estimator algorithm is established for the system and the parameters of the algorithm are tuned heuristically based on real-time measurement results. The performance of this estimator algorithm is mostly influenced by the process and measurement noise covariance matrices, however the noise statistics is difficult to measure in real practical problems, especially in case of micro-electro-mechanical systems-based attitude estimation problem, where the assumed noises are dynamics-dependent. Therefore, the heuristically selected filter parameters yield only a compromise solution between filter accuracy and convergence. To overcome this issue, a filter testing environment is created and numerical optimization is performed to find the performance maximizing filter parameters, where both the raw sensor data and true states are obtained in a novel test environment. Then, new measurement methods are developed to obtain the instantaneous vibration and external acceleration magnitudes (thereby to characterize the system dynamics) and a novel adaptive filter structure is established. This filter structure consistently modifies the noise covariances based on the instantaneous system dynamics via a heuristically defined fuzzy inference machine. The measurement results highlight that the adaptive filter structure provides superior convergence even in extreme dynamic situations based on the comparative assessment of existing popular attitude estimator algorithms. Finally, the generalization of the adaptive filter is derived for quaternion representation of orientation. This filter structure incorporates an extended Kalman filter, three measurement methods for real-time determination of vibration, external acceleration and magnetic perturbation magnitudes, and a sophisticated fuzzy inference machine to vary the filter parameters based on the instantaneous dynamics. A novel test environment is developed for filter performance evaluation, where a six degrees of freedom test bench both enables the execution of various system condition and simultaneously measure the real states and raw sensor data. The experimental results show that the derived filter significantly improves the robustness of state estimation, both in static and extremely vibrating and accelerating environments. The developed dynamic-dependent feature makes the filter structure a suitable candidate for attitude estimation in mechatronic systems operating in variable conditions.

Keywords: *Kalman-filter, Fuzzy Logic Control, Optimization, Adaptive-filter, Attitude Estimation, Inertial Measurement Unit, Self-balancing Robot*

Új lágy számítási módszerek alkalmazása a szenzorfúzióban és irányításban: valós alkalmazások egy mechatronikai rendszeren

Odry Ákos

Kivonat

Mechatronikai rendszerek dinamikus viselkedésének minőségét alapvetően két fontos algoritmus befolyásolja zárt körben. Egyrészt, az állapotbecslő algoritmus szolgáltat hasznos eredményeket a nem mérhető vagy zajos állapotokról. A becslések a rendszer dinamika és a megfigyelhető rendszer kimenetek szenzorfelületen keresztüli méréseit felhasználva kerülnek előállítása. Az algoritmus illesztése a problémához és paramétereinek hangolása egy kritikus mérnöki feladat, hiszen az irányítás (szabályozó tervezés), mely a szakaszt a kívánt állapotok környezetében stabilizálja, az előállított becsléseket felhasználva kerül kidolgozásra. Az állapotbecslő az aszimptotikus becslés mellett különböző tervezési követelményeket kell, hogy kielégítsen valós mérnöki problémákban, ilyenek a minimális hiba dinamika és gyors konvergencia. Ennek következményeként megállapítható, hogy algoritmus performanciája szignifikánsan befolyásolja az elérhető dinamikát zárt körben. Másrészt, az alkalmazott irányítási algoritmus (szabályozó) performanciája határozza meg a zárt kör karakterisztikáját. Ez az algoritmus az irányítási követelmények teljesülését biztosítja a megfigyelt és becsült állapotok visszacsatolásán keresztül. Ezen túl pedig, az irányítás minősége tölt be fontos szerepet a szabályozó tervezése során, hiszen a szabályozók struktúrája robusztusan (a paraméterbizonytalanság, rendszer zaj és külső zavarás mellett) kell, hogy biztosítson stabilizáló bemenő jeleket az irányítandó rendszer számára. A realizált irányítás minősége több szempontból vizsgálható, a minőségi alapjel követésen keresztül, az energia hatékony irányítási karakterisztikán át, az elektromechanikai rendszerek felépítését kímélő megoldás hatékonyságáig. A disszertációban a fenti két algoritmus karakterisztikáit vizsgálom és új lágy számítási módszereken alapuló megoldásokat fejlesztek és alkalmazok, melyek a zárt kör eredő dinamikáját tökéletesítik az állapotbecslési és irányítási performanciák finomításán keresztül. A kutatás során olyan eszközre volt szükség, amely lehetővé teszi a kifejlesztett technikák beágyazását, tesztelését és verifikálását. Az erre alkalmas mechatronikai rendszer a kutatásokban és az iparban is elterjedt kétkerekű önegyensúlyozó robot, hiszen az egyszerű felépítésének ellenére kihívások tömkelegét tárja elénk, a komplex dinamikus viselkedéstől, a nemlineáris hatásokon át, az instabil munkapontig.

Az első téziscsoport olyan fuzzy szabályozók kifejlesztésével foglalkozik, amelyek robusztusabb dinamikus viselkedést és hatékonyabb energiafogyasztást biztosítanak robotikai alkalmazásokban, mint a közkedvelt megoldások. A feladat a zárt kör megtervezését, a mechatronikai rendszer stabilizálását és az elérhető irányítási performancia maximalizálását foglalja magába. A kidolgozás a választott mechatronikai rendszer (robot) valósághű modelljének meghatározásával indul, mely lehetővé teszi az irányítások következetes tervezését, tesztelését, realizálását és későbbi optimalizációját. A kutatás eredményeként megadom az önegyensúlyozó robotok 8-dimenziós nemlineáris dinamikus modelljét, mely a nemlineáris mechanikai hatások

mellett a meghajtó motorok dinamikáját is magában foglalja. A következő kutatási lépésként a lineáris és fuzzy logikán alapuló irányítások - fuzzy logikai szabályozók – tervezésével foglalkozom. A sikeres tervezést pedig a realizáció követi, mely az implementációt és tesztelést foglalja magába a valós mechatronikai rendszeren. Ebben a fázisban az irányítások heurisztikus módon vannak megtervezve a szakasz dinamikus viselkedésének megfigyelésén keresztül. A realizált irányításokkal elérhető irányítási performanciák kiértékelése képezi a kutatás következő fázisát. Az irányítások minőségét a tranziens viselkedések és különböző hiba integrálok kiértékelésével jellemzem. A numerikus optimalizáció esetében az irányítási minőség javítása költségfüggvény (fitness függvény) minimalizációs feladat. Az alkalmazott optimalizációs stratégiát négy fontos részre bontom. Első lépésként létrehozok egy paraméterezhető fuzzy következtető gépet és a hozzá tartozó MATLAB/Simulink teszt környezetet. Ezután, a dinamikus viselkedést egy komplex költségfüggvénnyel minősítem, mely figyelembe veszi a transzlációs mozgás dinamikáját, a közbenső test oszcillációját, valamint az implementált irányítás energia hatékonyságát. Harmadik lépésben alkalmazom a részecskeraj algoritmust az optimális szabályozó paraméterek megtalálása céljából. Végül pedig kiértékelem és összehasonlítom az optimalizált (vagy maximalizált) lineáris és fuzzy irányítási performanciákat. A fenti vizsgálatok eredményeként egy speciális fuzzy logikai szabályozó kerül definiálásra, mely áram tranziens limitáló mechanizmussal van felvértezve. A speciális struktúrának köszönhetően az áram tranziensek és oszcillációk sokkal kisebb mértékben jelentkeznek a robot elektromechanikai rendszerében a realizált fuzzy irányítás esetében, mint a lineáris irányításoknál.

A második téziscsoport az állapotbecslés minőségének tökéletesítését tárgyalja és olyan újszerű, lágy számítási módszereken alapuló technikákat vizsgál, melyek a megbízható becslési eredmények biztosítása mellett finomított performanciát mutatnak extrém dinamikus szcenáriókban is. A választott rendszer esetében a közbenső test orientációja képezi a nem mérhető és zajos rendszer állapotot. Az orientáció becslésére elterjedt megoldás a Kalman-szűrő (állapotbecslő) alkalmazása. Az algoritmus performanciáját az állapotegyenletben definiált zajok kovariancia mátrixai határozzák meg. Azonban, a legtöbb valós alkalmazásban a kovariancia mátrixok értékei nem mérhetők, ezért azok beállítása nem egyértelmű feladat. Továbbá, sok esetben a mérnöki intuíció és/vagy trial-and-error alapú hangolások csak kompromisszumos megoldásokat eredményeznek, mely kritikus kimenetelt eredményezhet instabil rendszerek szabályozása esetén. A téziscsoportban két új megoldást mutatok be az állapotbecslő performanciájának tökéletesítésére. Először kialakítok egy speciális teszt környezetet, melyben a szakasz valós (nem mérhető) állapota mérhetővé válik a realizált állapotértékek mellett. A mérési eredményeket felhasználva a szűrő paraméterek optimalizációját dolgozom ki a kialakított szimulációs környezetben. Ezt követően egy adaptív-fuzzy állapotbecslő struktúrát definiálok, mely a pillanatnyi vibrációk és külső gyorsulások (azaz a rendszer dinamikus viselkedésének) figyelembevételével online módosítja a szűrőparamétereket, ezáltal tovább javítva a becslési konvergencia minőségén. A kifejlesztett adaptív szűrő performanciáját két populáris állapotbecslő algoritmussal hasonlítom össze. A kutatás következő lépésében, ezt az adaptív szűrő struktúrát kiterjesztem és általánosítom kvaternió alapú orientáció becslésre. Az általános szűrő struktúrában kiterjesztett Kalman-szűrőt alkalmazok; a pillanatnyi külső zavarásokat mérőszámokkal jellemzem három új mérési módszer (vibrációk, külső gyorsulások és mágneses zavarások) segítségével, valamint egy

kifinomult fuzzy következtetési gép segítségével HA-AKKOR szabálybázist implementálok a szűrőparaméterek következetes, online módosítására. Az adaptív szűrő orientáció becslésének konvergenciáját a háromdimenziós térben egy új teszt környezetben értékelem ki, ahol egy hat szabadságfokú mechatronikai rendszer lehetővé teszi különböző dinamikus viselkedések szimulálását és mind a valós rendszerállapotok mind pedig az érzékelő adatok szimultán mérését. A különböző szcenáriókban (kevert statikus és extrém dinamikus viselkedések mellett) elvégezett mérési eredmények a kifejlesztett adaptív szűrő robusztus karakterisztikáját bizonyítják. A kiváló eredmények a szűrő dinamika-alapú tulajdonságainak köszönhető, hiszen a szűrő paraméterek konzisztens változtatása az érzékelőkel realizált szögpozíciók előnyös fuzionálását teszi lehetővé.

Acknowledgement

I would like to thank my supervisor Prof. Dr. Róbert Fullér for his regular professional help during my doctoral studies.

I am thankful to the University of Dunaújváros for the financial support granted through the predoctoral fellowship. This work is supported by the EFOP-3.6.1-16-2016-00003 project. The project is co-financed by the European Union.

I also owe special thanks to my girlfriend Nati. Your love, support and patience meant much more than you thought and helped me a lot throughout my doctoral studies.

Finally, I dedicate this work to my loving family, especially to my parents, for their financial and spiritual assistance throughout my life. You have provided me love, understanding and encouragement to chase my dreams. This dissertation would not have been possible without your continuous support.

Contents

Abbreviations

In this study the following notations and abbreviations are used:

PID	proportional–integral–derivative
LQR	linear-quadratic-regulator
LQG	linear–quadratic–Gaussian
SMC	sliding mode control
CARE	control algebraic Riccati equation
T-S	Takagi-Sugeno
PDC	parallel distributed compensation
FLC	fuzzy logic controller
LUT	look-up table
SISO	single-input single-output
SAE	sum of absolute errors
SSE	sum of square errors
STAE	sum of discrete time-weighted absolute errors
STSE	sum of discrete time-weighted square errors
MAE	mean absolute error
MSE	mean squared error
STD	standard deviation
COA	center of area
NED	North-East-Down
SO(3)	special orthogonal group
IIR	infinite impulse response
CF	complementary filter
qNCF	quaternion-based nonlinear complementary filter
KF	Kalman filter
UKF	unscented Kalman filter
MCKF	maximum correntropy Kalman filter
EKF	extended Kalman filter
qAEKF	quaternion-based adaptive extended Kalman filter
FAEKF	fuzzy-adaptive extended Kalman filter
DCM	direction cosine matrix
TRIAD	three-axis attitude determination
QUEST	QUaternion ESTimator
FOAM	fast optimal matrix algorithm
FQA	factored quaternion algorithm
GRNN	general regression neural networks
GA	genetic algorithm
PSO	particle swarm optimization
FFT	fast Fourier transform

MEMS	micro-electro-mechanical system
IMU	inertial measurement unit
MARG	magnetic, angular rate, and gravity
AHRS	attitude and heading reference system
MCU	microcontroller unit
ROS	Robot Operating System
URDF	Unified Robot Description Format
CAD	computer aided design
DOF	degrees of freedom
3D	three dimensional
WMP	wheeled mobile pendulum
TWIP	two-wheeled inverted pendulum
SBR	self-balancing robot
IB	inner body
UAV	unmanned aerial vehicle
GUI	graphical user interface

1 Introduction

The overall performance of a closed-loop system depends on two important algorithms. Namely, the state estimator algorithm contributes to provide useful measurements of the system and the implemented control algorithm produces the control action to stabilize the plant around the desired state (see Fig. 1.1). On one hand, reliable estimation is both an essential and crucial task of the state estimation design problem, since the stabilizing system inputs are calculated based on the estimation results. If the state estimation contains significant errors, then these control signals will drive the system out of equilibrium to unwanted states, which may eventually damage the system and its environment. On the other hand, control system design problem involves the development of such control strategy that tolerates both model uncertainties and noisy input signals, and thereby provides suitable control action that satisfies the control requirements (even if the system dynamics is unknown) Barton (1996); Odry *et al.* (2018, 2020b).

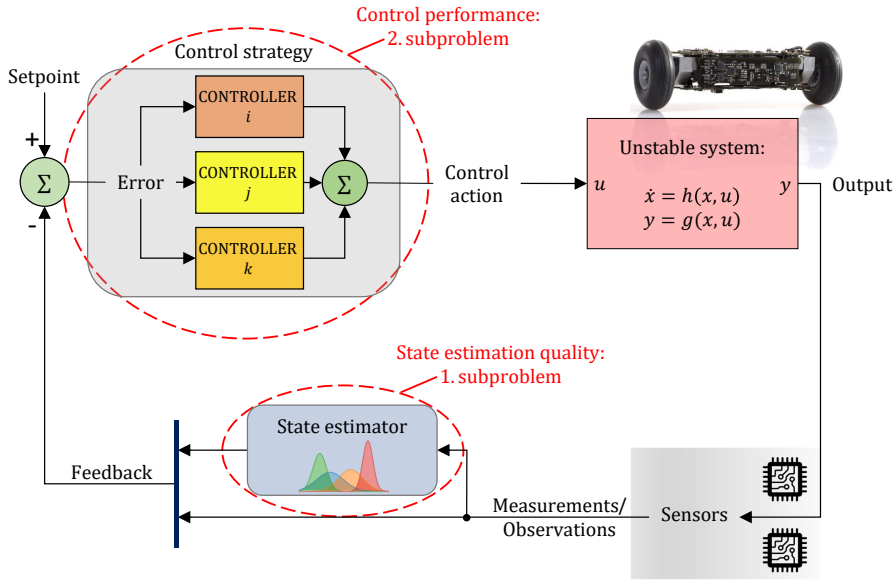

Figure 1.1: General block diagram of closed-loop systems.

Since, the implemented estimator and controller algorithms are linked in a closed loop, therefore, it is a challenging issue to tune these algorithms and thereby maximize the closed loop performance, especially if the system to be controlled is naturally unstable. Moreover, it is also difficult to determine whether a badly designed controller or state estimator results in modest of unsatisfactory system behavior. This discussion illustrates that the procedure for achieving maximized closed loop performance, i.e., providing both maximized estimation convergence and effective (enhanced) control action (such as in sense of response dynamics, current consumption and/or mechanical protection), remains an important issue. Therefore, my work addresses the preceding issues and proposes two distinct approaches to enhance the overall closed-loop performance. Namely, the overall control performance maximization problem has been divided into two sub problems. First, the work separately discusses the enhancement

of control strategies with the aid of soft computing techniques, then the improvement of state estimation performance is addressed with novel adaptive approaches.

This work focuses on the advantageous applicability of both fuzzy logic controllers (FLCs) and fuzzy logic-based inference systems for robotic applications. As a result, the first part of my work addresses the development of such fuzzy control strategies that provide more effective closed-loop performance than the fundamental techniques. Moreover, in the second part of the work, fuzzy-based adaptive solutions are developed for robust state estimation.

Since the research work both involves and fuses separate research fields and applications, therefore the research background (section 1.1) has been divided into four parts. The discussion of each research field is summarized as follows.

1. Subsections 1.1.1 and 1.1.2 discuss the fuzzy logic-based control approaches and common fundamental techniques and then emphasize the advantages of fuzzy based approaches in order to motivate the fuzzy logic-based initiative over the classical methods.

2. Both for the elaboration and analysis of control system design problems, a test environment was required to be selected. The importance of the selected unstable mechatronic system (robot), moreover, the recent developments regarding its control approaches are discussed in subsection 1.1.3.

3. The state estimation problem, characteristics of fundamental approaches and the recent advances are analyzed in detail in 1.1.4.

Each of the aforementioned subsections addresses some issues and confirms some important aspects of both state estimation and control. Moreover, these observations motivated my work throughout the research and development procedure presented in this document. The findings and observations are documented in section 1.2, while the main contributions are summarized in section 1.4. Finally, section 1.3 briefly introduces the robot which was a benchmark mechatronic system on which the closed-loop performance was analyzed in this work.

1.1 Research Background

Nowadays, technological developments face dynamical systems that are getting more and more complex and complicated by the day. These complex systems are characterized by high order dynamics, uncertain parameters, and most often, their nonlinear mathematical model is only approximately known (such as the analyzed system in our work). Over the last few decades, it has been shown that conventional and modern linear control techniques have been extensively applied in control development and industrial automation, however, their performance is always an issue to be carefully analyzed, when systems with uncertainty and unmodeled dynamics are controlled. In general, the linear controllers do not work well for nonlinear vague systems Tang *et al.* (2001).

1.1.1 Fuzzy Logic-based Control Solutions

Zadeh's fuzzy logic and approximate reasoning introduced a new linguistic information based design perspective, where imprecision and uncertainty form the basis of the inference mechanism Zadeh (1965). The application of heuristic IF-THEN rules allows the expert to easily establish

input-output relationships of the system to be designed based on deductions related to system dynamics Wang (1997). Moreover, this approximate reasoning approach gives the appropriate tools to both perform smooth control action and cover model imprecision and uncertainties in the system, and additionally, the inference mechanism formed by these fuzzy rules allows the system designer to neglect the derivation of complex mathematical formulas and even to consider the plant as a black-box model Fukuda and Kubota (1999); Das and Kar (2006); Hou *et al.* (2009); Kecskés and Odry (2014). Due to these advantages, fuzzy logic control plays an important role in systems with unknown structure and has been widely used in automotive control applications López-Guauque and Gil-Lafuente (2020); Tamir *et al.* (2015); Dubois and Prade (2015). Thanks to its rapid progress, fuzzy reasoning is a fruitful research area for the Robotics and Control Community, where the achievable control performance, competitive cont-rol techniques and fuzzy-based engineering solutions are continuously investigated and widely utilized in nowadays technological developments both in industry and scientific research including signal processing, robotics and control Verbruggen and Bruijn (1997); Huang *et al.* (2011); Anisimov *et al.* (2018); Csaba and Vamossy (2012); Kumar *et al.* (2017); Nourmohammadi and Keighobadi (2018). Some potential results in real practical environments are summarized as follows.

The provided flexibility, linguistic information-based design and heuristic knowledge oriented development capability enabled fuzzy control to be a popular technology in the development of unmanned air vehicles (UAVs) McLean and Matsuda (1998); Kumon *et al.* (2006); Santos *et al.* (2010), where the developed fuzzy control strategies provided acceptable station-keeping performance, successful stabilization, wind disturbance rejection and tracking control even in severe turbulences. In references Das and Kar (2006); Hou *et al.* (2009) adaptive FLCs were proposed for the robust control of nonholonomic mobile robots that were characterized with uncertain parameters, and the results proved the robustness of the derived tracking control schemes. Reference Lee and Gonzalez (2008) examined the achieved control performance of both conventional proportional–integral–derivative (PID) and fuzzy techniques for position control of a muscle-like actuated arm. Adaptive fuzzy logic-based stabilization of two-wheeled inverted pendulum systems has also been investigated and effectively used both in simulation environments and on real plants Huang *et al.* (2011); Anisimov *et al.* (2018). Moreover, fuzzy control was successfully applied in the development of walking robots. Reference Kecskés and Odry (2014) optimized the fuzzy controllers of a hexapod robot called Szabad(ka)-II in such a way to simultaneously minimize the current consumption and maximize the walking speed.

Over the past decade, it has been widely investigated weather fuzzy logic-based control solutions can replace the linear approaches. Many applications have been proposed where fuzzy control showed superior performance (e.g., in references McLean and Matsuda (1998); Kecskés and Odry (2014); Ahmed *et al.* (2016); Kecskés *et al.* (2017a)) over using linear techniques, however, the opposite outcome was often claimed as well (such as in works Lee and Gonzalez (2008); Das and Kar (2006)). Similarly, my investigation in Odry *et al.* (2016b) compared fuzzy control and linear–quadratic–regulator (LQR) approaches for the stabilization of a mobile robot. In this work, the measurement results have shown that the former solution provided better overall control performance, while the latter approach showed faster system dynamics for transient events. Since, the controllers were designed heuristically (trial-and-error methods),

therefore a general conclusion could not be stated.
Observation: These results prove that fuzzy logic provides a fruitful research area, however, the effective and beneficial applicability of fuzzy control still remains an important issue to be further addressed.

1.1.2 Fundamental Approaches as Benchmark Control Solutions

The linear control strategy, consisting of one or more PID-type feedback loops, forms the fundamental solution to stabilize the system around a reference state (i.e., desired set point). The parameters of these controller(s) can be derived via numerous techniques, from simple model-based root locus, over black box-based tuning algorithms, to both cost function minimization with LQR or numerical optimization-based tuning Ho *et al.* (1995); Visioli (2001); dos Santos Coelho (2009); Prasad *et al.* (2014).

Among the solutions, the LQR technique is a beloved method in the control of dynamical systems since it provides the optimal state feedback gain based on the well-developed mathematical algorithm Franklin *et al.* (1994). Numerous researches have been dealt with its application and control performance in real embedded environments Divelbiss and Wen (1997); Araar and Aouf (2014); Ji and Sul (1995); Bouabdallah *et al.* (2004); Jeong and Takahashi (2007); Shao and Liu (2010); Li *et al.* (2011); Nagaya *et al.* (2013). Reference Divelbiss and Wen (1997) presented the experimental results of tracking control of a car-trailer system. Similarly, reference Ji and Sul (1995) proposed a linear–quadratic–Gaussian (LQG) speed control method for torsional vibration suppression in a 2-mass motor drive system which gave satisfying performance and robust behavior against parameter variations. The control performances of PID and LQR techniques applied to an UAV were compared in Bouabdallah *et al.* (2004), and it was emphasized that the control performance of the latter technique was significantly influenced by model imperfections. Recent efforts broaden further the set of experimental research results, including the control of inverted pendulum type assistant robot Jeong and Takahashi (2007), self-balancing unicycle robot Shao and Liu (2010), UAVs in uncertain environments Li *et al.* (2011); Araar and Aouf (2014), and wheeled inverted pendulum systems Nagaya *et al.* (2013).
Observation: The aforementioned papers highlight that the LQR technique provides competitive performance in the control of dynamical systems, therefore its control performance is regularly taken into account as a benchmark in comparative analyses Prasad *et al.* (2014); Nasir *et al.* (2010); Al-Younes *et al.* (2010); Márton *et al.* (2008); Xu *et al.* (2014); Guo *et al.* (2014); Dai *et al.* (2015); Sun and Li (2015); Xu *et al.* (2013a).

1.1.3 Wheeled Mobile Pendulum Robots

Wheeled mobile pendulum robots (WMPs), also known as two-wheeled inverted pendulum (TWIP) and self-balancing robots (SBRs), have both gained a great deal of attention and become popular mechatronic systems to be both developed and controlled over the last few decades in research works, commercial utilization and education Nagarajan (2012); Shomin (2016); Lilienkamp (2003); Zhaoqin (2012). WMPs are the descendant of the pendulum-cart systems and provide a big variety of applications due the the advantageous electro-mechanical properties. These properties include the compactness in both construction and footprint, mobility characterized by zero turning radius, as well as, low cost and low energy consumption Li

et al. (2012); Sciavicco and Siciliano (2012). As a result, WMPs are considered both as mobile robot platforms to be effectively controlled and important benchmark systems to verify the theoretically proven control approaches. Moreover, the most successful commercial product is the Segway PT, a two-wheeled, self-balancing electric device used for personal transportation in everyday life Segway (2020).

Since the mechanical structure of the WMP consists of two actuated wheels and an inner body (IB) that forms a pendulum, the fundamental control objective is to simultaneously ensure the planar (longitudinal and rotational) motion of the wheels and stabilize the pendulum around the equilibrium point. Even though numerous control approaches have been proposed for WMP systems both for simple and harsh terrain environments, the Robotics and Control community still investigates both the realization of efficient control performances and the dynamical or stability analysis of the system up to now Chan *et al.* (2013); Lee and Jung (2012); Kim *et al.* (2006); Jeong and Takahashi (2008); Grasser *et al.* (2002); Raffo *et al.* (2015); Yue *et al.* (2014); Xu *et al.* (2014); Guo *et al.* (2014); Dai *et al.* (2015); Ghaffari *et al.* (2016); Zhou and Wang (2016b); Sun and Li (2015); Ruck *et al.* (2016); Maruki *et al.* (2014); Cui *et al.* (2015); Huang *et al.* (2011); Xu *et al.* (2013a); Yang *et al.* (2014); Pathak *et al.* (2005); Zhou and Wang (2016a); Yue *et al.* (2016); Xu *et al.* (2015); Yoshida *et al.* (2016); Vasudevan *et al.* (2015). The interest comes from the challenges the electro-mechanical characteristics of the WMP inherently yields, which are related to the nonlinear underactuated configuration, the presence of nonholonomic constraint and the unstable open-loop behavior Chan *et al.* (2013). The underactuated configuration stems from that the system has three degrees of freedom including the planar motion and the oscillation angle of the pendulum, while the wheels are driven through two control inputs only. This property lowers the realization costs, the power consumption (only two actuators) and the system order, however it also increases the complexity of control system design. The presence of nonholonomic constraint is due the assumption that the wheels move by satisfying the pure rolling constraint, i.e., slipping does not occur. This constraint is a nonintegrable kinematic constraint that restricts the achievable velocities of the system, thus the control laws elaborated for holonomic systems are not utilizable. Furthermore, the system has an open-loop unstable equilibrium point that requires such control approaches which ensure limited oscillation range of the IB, otherwise the pendulum falls and system cannot recover itself. The aforementioned features motivate the development of control approaches that provide both robust stability and satisfying control performance even if uncertain circumstances or external disturbances occur. This motivation is further strengthened by the opportunities nowadays embedded technologies provide, such as the high computational performance, low cost and low power consumption.

Regarding the control system design of WMPs two approaches are prevalent. Linear controllers, such as the classical PID Lee and Jung (2012) or state feedback Kim *et al.* (2006); Jeong and Takahashi (2008); Grasser *et al.* (2002), are designed considering the linearized mathematical model of the plant, and the control parameters are selected based on some observations of the system behavior and tuned often by trial and error. However, the stability of the closed loop system is always an issue when the system leaves the neighborhood of the equilibrium, or uncertainty, unmodeled dynamics and disturbances present in the system. Usually in these

cases, the linear approach does not provide satisfying close loop behavior, therefore to overcome these issues, advanced techniques are proposed. Among the advanced techniques, $\mathcal{H}_\infty$ control Raffo *et al.* (2015), which allows the explicit consideration of uncertainties and noises, or the non-linear sliding mode control (SMC) Yue *et al.* (2014); Xu *et al.* (2014); Guo *et al.* (2014); Dai *et al.* (2015); Ghaffari *et al.* (2016); Zhou and Wang (2016b) that provides parametric robustness are quite common. Moreover, adaptive Sun and Li (2015); Ruck *et al.* (2016) and adaptive backstepping control Maruki *et al.* (2014); Cui *et al.* (2015), soft-computing techniques Huang *et al.* (2011); Xu *et al.* (2013a); Yang *et al.* (2014), and also partial feedback linearization Pathak *et al.* (2005); Zhou and Wang (2016a); Yue *et al.* (2016) based methods are proposed in the literature. Among the investigations, such studies are predominant where theoretical results and simulation figures of the proposed control method are provided. In most cases, a simplified mathematical model is derived and the difficulties that arise in real prototypes are neglected. Due to the complexity of implementation, less control approaches have been implemented and tested on real time platforms. In the following paragraph, a brief description is given of the advances of last decade investigations in the field of practical control of WMP systems.

Reference Jeong and Takahashi (2008) dealt with the work capability of WMP systems as human-assistant robots. A prototype system was proposed and various motions were realized using LQR-based state feedback control. In reference Lee and Jung (2012) practical oriented solutions were proposed for the stabilization of a WMP platform. The control design was based on the mathematical model derived in Pathak *et al.* (2005), and the closed loop was formed by PID controllers. The paper also proposed a tilt angle estimation solution that combines complementary and Kalman filters (KFs). Fuzzy control of a WMP prototype was investigated in Huang *et al.* (2011). The elaborated control approach employed three fuzzy controllers, which were one by one responsible for the position and orientation of the robot and the balance of the pendulum. For the control design, the Takagi-Sugeno (T-S) fuzzy model of the plant was utilized, and the balance standing was solved with a parallel distributed compensation (PDC) controller, moreover, Mamdani type FLCs were defined for the planar motion of the robot. The control structure was constructed such a way, that the position error did not influence directly the control input, instead, the position control was ensured by manipulating the desired pendulum angle. A different fuzzy control approach for WMP systems was proposed in Xu *et al.* (2013a). The set point control task, where the reference was given with a step signal, was converted to trajectory tracking problem in order to limit the initial control values. For the control system design, a T-S type FLC with full-state feedback (four inputs) was adopted. The membership functions were defined based on heuristic knowledge, while the FLC output was determined considering the output of a linear LQR controller. In this way the manual tuning was eased. Through different real-time experiments (including flat and inclined surfaces) the authors showed the effectiveness of the proposed control method against the approach Huang *et al.* (2011). Reference Sun and Li (2015) proposed a neural control method for WMPs which was based on extreme learning machines. In reference Raffo *et al.* (2015) a nonlinear $\mathcal{H}_\infty$ controller was designed and realized for a real WMP vehicle. The elaborated controller took into account the whole dynamics of the system and ensured closed-loop stability. The theoretical results have been verified in practical environment, where the proposed approach provided short response

time and robustness against parametric uncertainties during the stabilization of the system. Reference Dai *et al.* (2015) presented different practical solutions for the development of WMPs, namely, both identification methods for friction and inertia parameters and a pendulum angle estimation technique which takes into account the position of the sensor installation have been proposed, moreover, SMC was designed to stabilize the plant. In the proposed identification procedure, the parameters were identified based on both the measurement results and the equilibrium torque equation of the DC motors. It was shown that that by considering the location of the applied accelerometer, the pendulum angle estimation is enhanced. Finally, the achieved control performance was compared with the classical PID control approach. Similarly, in references Xu *et al.* (2014); Guo *et al.* (2014) SMCs were designed and realized for real WMPs. The proposed techniques were able to stabilize the real-time platform, moreover, the uncertainties that arisen due to the mismatch between the ideal mathematical model and the real plant were handled robustly. The control performance was compared with the LQR controller, in which the feedback gains were re-tuned after the implementation since high vibrations occurred. *Observation:* In many instances, the complex mathematical relations make the implementation difficult and too complicated due to both time variant and unknown parameters. On the other hand, there are many cases where the control action computation takes into account the physical parameters of the plant which are usually not validated. Therefore, a fuzzy control scheme that can be commonly used in practice, less complex and provides both easy implementation and effective control performance for WMPs still remains an important issue to be further addressed. Moreover, both linear and modern control approaches has been elaborated and analyzed for this type of systems (as it was highlighted in the literature overview), however, the design of the controllers was based on trial and error procedures in most cases and the achievable control performance has not been investigated, which also motivated my work.

1.1.4 Attitude Estimation

Since the control objective of WMPs is to simultaneously guarantee the planar motion of the wheels and stabilize the pendulum, therefore providing accurate attitude values as input to the applied control structure is essential for stabilizing the unstable system. However, the relative orientation of a WMP body cannot be measured with encoders, instead, its attitude is estimated with filter (estimation) algorithms based on the measurement results of micro-electro-mechanical systems (MEMS). The process to tune the estimation algorithm is a cumbersome task. Usually trial and error methods are applied to set up the estimator algorithm Dai *et al.* (2015); Lee and Jung (2012); Huang *et al.* (2011), however, this tuning procedure is a challenging issue for WMPs because they are naturally unstable, moreover, the implemented estimator and controller algorithms are linked in a closed loop. Therefore, as it was emphasized earlier, it is difficult to determine whether a badly tuned controller or attitude estimator results in unsatisfactory system behavior. Additionally, there are two main types of disturbances that cause the WMP system attitude estimation to become unreliable: external acceleration and external vibrations. External acceleration can occur as a result of either a predefined planar motion (i.e., following a desired trajectory) or external influences (i.e., the robot is pushed or collides with obstacles). Vibrations also arise during closed-loop behavior, because real systems

encounter driving mechanism backlash that produces unwanted system behavior, especially when larger control signals are applied Xu *et al.* (2013b). Therefore, closed-loop performance usually depends on both ad-hoc estimator tuning (with a virtually unknown convergence quality) and a controller that roughly tolerates estimation that is inaccurate, noisy, or delayed.

The aforementioned discussion highlights that the MEMS-based relative localization problem (where the positions and orientation information of moving objects should be determined) is an important topic, which is widely investigated in many areas including robotics and control Wen *et al.* (2019); Roh and Kang (2018); Battiston *et al.* (2019); Liu *et al.* (2019); Ahmad *et al.* (2019); Wilson *et al.* (2019); Dai *et al.* (2015), health care and rehabilitation Baldi *et al.* (2019); Duraffourg *et al.* (2019); Zhang and Xiao (2018), consumer electronics mobile devices Zhao *et al.* (2019); Michel *et al.* (2018); Gośliński *et al.* (2015), and automated driving and navigation Jouybari *et al.* (2019); Nourmohammadi and Keighobadi (2018); Xiong *et al.* (2019); Khankalantary *et al.* (2019), both in industry and in scientific research. Independent from the application, accurate and robust attitude estimation is a crucial task to be solved, especially if the results are to be incorporated into unstable closed-loop systems, such as the control algorithms of mobile robots and unmanned aerial vehicles (UAVs) Odry *et al.* (2018).

The MEMS inertial measurement unit (IMU), composed of tri-axis MEMS accelerometer, gyroscope, and magnetometer sensors, also known as the measurement system of magnetic, angular rate, and gravity (MARG) sensor arrays, is the most commonly utilized device to track the real-time orientation of mobile platforms at present. The low-cost, low power consumption, and small size characteristics meet technological requirements, and therefore these devices have been widely utilized in embedded systems, where the filtering algorithm is executed by a microprocessor. As a result, an attitude and heading reference system (AHRS) has been formed, which provides the complete orientation measurement relative to the Earth's gravitational and magnetic fields (global reference system), where the attitude denotes the roll and pitch angles, whereas heading refers to the yaw Euler angle Lee *et al.* (2012). The role of the aforementioned filtering algorithm is to combine the individual features of each sensor and provide both properly smoothed and robust attitude results with regard to the global reference system, in either Euler angles or quaternions. The most common method applied in sensor fusion techniques synthesizes the short-term accuracy of gyroscope-based attitude realizations and the accelerometer and magnetometer provide rough, low-frequency attitude corrections. This technique cancels the accumulated error (drift), smooths the signals, and produces long-term stable outputs if the IMU is in stationary states. Significant decrease in estimation performance arises when external disturbances are present, such as external accelerations, vibrations, and magnetic distortions, which prevent the utilization of the pure gravity and local magnetic field vectors in the calculation of the direction cosine matrix (DCM). The following paragraphs discuss the solutions provided in the literature.

Among recent developments, the KF—by different variants, such as stochastic approaches—and complementary filter (by frequency domain methods), both augmented with the intelligent use of deterministic techniques, have become the most popular methods for robust attitude determination Wu and Shan (2019). Deterministic techniques have been shown to solve Wahba's problem Wahba (1965) and provide attitude estimation based on gravity and magnetic field ob-

servations. The fundamental solutions are three-axis attitude determination (TRIAD), which produces suboptimal attitude matrix estimation by the construction of two triads of orthonormal unit vectors, and the QUaternion ESTimator (QUEST), in which the quaternion is found by minimizing a quadratic gain function based on a set of reference and observation vectors. Improved approaches have utilized the fast optimal matrix algorithm (FOAM) Markley and Crassidis (2014), the factored quaternion algorithm (FQA) Yun *et al.* (2008), the Gauss–Newton algorithm Liu *et al.* (2014), Levenberg Marquardt algorithm Fourati *et al.* (2010), the gradient descent algorithm Madgwick *et al.* (2011), and the super fast least-squares optimization-based algorithm Wu *et al.* (2018). Each approach estimates the attitude based on accelerometer and magnetometer measurements and is characterized by reduced computational complexity or more robust performance. As the estimation performance significantly decreases with disturbances (magnetic perturbation and/or external acceleration), the incorporation of gyroscope measurements has thus become a de facto standard for the state propagation.

Complementary filters (CF) use frequency domain information to synthesize signals that have complementary spectral components. This concept enables us to combine the slowly varying signals of the accelerometer and magnetometer with the fast signals of the gyroscope through low- and high-pass filters, respectively. The CF has been widely implemented in the robotics and control community, due to its simple structure and ease of implementation Euston *et al.* (2008); Tsagarakis *et al.* (2017). In Euston *et al.* (2008), a nonlinear CF was developed for UAVs, which also employed first-order vehicle dynamics to cancel the effect of external acceleration. A quaternion-based nonlinear CF (qNCF) for attitude estimation was developed in Mahony *et al.* (2008) (hereafter referred to as the Mahony filter), which corrects the gyroscope measurements with a proportional and integral (PI) controller and provides attitude and gyroscope bias estimates. The popular Madgwick filter Madgwick *et al.* (2011) is a computationally efficient constant gain filter, which was developed originally for human motion tracking applications. The filter has been improved recently in Wilson *et al.* (2019), employing the accelerometer and magnetometer measurements in a gradient descent algorithm to correct the quaternion obtained through the integration of rate measurements. Mahony and Madgwick filters are widely utilized algorithms and their performances have regularly been considered in comparative analyses Cavallo *et al.* (2014); Valenti *et al.* (2015); Mourcou *et al.* (2015); Michel *et al.* (2018); Jouybari *et al.* (2019); Baldi *et al.* (2019). In Tian *et al.* (2012), an adaptive-gain CF was proposed to provide good estimates, even in dynamic or high-frequency situations. The filter gain was modified based on both the convergence and divergence rates of observation-based orientation realization and gyroscope-based orientation propagation, respectively. An improved qCF was designed in Valenti *et al.* (2015), in which two correction sequences were employed based on separating the quaternion into accelerometer- and magnetometer-based realizations. Moreover, the algorithm was augmented with an adaptive gain characterized by two thresholds to reduce the estimation error when dynamic motion is present. The filter performance was validated with experiments containing short external disturbances. This algorithm was adapted in Duraffourg *et al.* (2019), where its real-time performance was evaluated on a microprocessor-controlled lower limb prosthesis. An iteration-free variant of CF has been proposed for efficient attitude estimation calculation in Wu *et al.* (2016), where a linear system was employed for the

accelerometer-based attitude realization. The filter performance was evaluated under different conditions and the effects of vibration and magnetic distortion were examined as well. However, the developed CF was not as accurate as the benchmark KF, especially under highly dynamic conditions. In Fan *et al.* (2018), a two-step qCF was implemented for human motion tracking applications. The algorithm was characterized by two separate tuning parameters; moreover, it contained a finite state machine-based adaptive strategy to cope with external disturbances. The two-step configuration made the attitude output more resistant to magnetometer measurements, as the attitude was obtained based on accelerometer and gyroscope data first, following which the heading angle was updated using both the estimate and magnetometer data.

The KF and its extension for nonlinear cases, the extended KF (EKF), are the most prevalent Bayesian state estimation algorithms utilized for attitude determination. These recursive algorithms deal with statistical descriptions and predict the state of the Gaussian stochastic model of MARG with minimum variance. The main performance, which includes both the filter dynamics and convergence, is determined with the proper covariance matrices that describe the stochastic system. In Sabatini (2006), a qEKF was developed for human movement tracking, in which the state of a rotation quaternion was augmented with the random walk processes of accelerometer and magnetometer bias vectors. Moreover, an adaptive strategy modified the noise covariance matrix if an external disturbance was identified. The filter was improved by modeling the magnetic variations with a Gauss–Markov vector random process, which aimed to reduce the effect of fluctuating magnetic environments Sabatini (2011). Adaptive threshold-based switching strategies have been used to modify the covariance matrices based on the measured stationary-, low-, and high-acceleration modes in Li and Wang (2013); Mazza *et al.* (2012). In Lee *et al.* (2012), an acceleration model was incorporated in the stochastic model, and thus the KF both estimated and compensated for the external acceleration in an attitude determination process. The proposed method was evaluated under dynamic conditions and compared with a threshold-based KF; however, significant improvement in the estimation accuracy was not highlighted. In Gośliński *et al.* (2015); Nowicki *et al.* (2015), smartphone-based human body orientation estimation was addressed with the application of a qAEKF. The proposed adaptive strategy modified the noise covariance matrix based on the variance of input signal. Moreover, the upper and lower bounds of covariance values were selected by numerical optimization. Comparison with both the Android OS algorithm and a simple CF highlighted the benefits of the proposed method. A similar qEKF structure without adaptation laws was proposed for the attitude estimation of UAVs in Zhang and Liao (2017). The filter was set up with experimentally tuned noise covariance matrices; however, its performance was evaluated without external dynamic effects on a multi-function turntable device. A reduced state vector-based qEKF approach was applied in Roh and Kang (2018), in which the measurement noise covariance was tuned in real-time, based on the angle between the predicted and measured gravitational accelerations. A two-step geometrically-intuitive quaternion correction was proposed for a linear KF, which enabled isolation of the pitch and roll estimation performance from magnetic distortion effects by decoupling the accelerometer and magnetometer data Feng *et al.* (2017). In Ligorio and Sabatini (2015), a linear KF was implemented for human motion tracking applications in dynamic environments. In their real-world experiments, the effects of long external accelerations

were addressed and good overall performance was achieved by the filter; however, significant error peaks were present in the estimation as well. A smart detector augmented AEKF was proposed in Makni *et al.* (2015) with similar filter efficiency. The adaptive strategy identified both static and dynamic body motions. Moreover, the effect of external acceleration was suppressed through filter gain tuning. The attitude estimation problem during sports activities was addressed in Yuan *et al.* (2019), where the proposed EKF considered the model uncertainty of active acceleration. Experiments highlighted the robustness of the approach, especially when large accelerations were present during the tests. In Stateczny (2001), the maneuvering target tracking problem was addressed and the application of both General Regression Neural Networks (GRNN) and an additional maneuver detector algorithm was proposed for the state estimation of manoeuvring objects. Moreover, a comparison of the GRNN-based neural filter and KF for target movement vector estimation was presented in Stateczny and Kazimierski (2008); Kazimierski and Łubczonek (2012), where the GRNN-based approach was characterized by superior estimation performance only during steady motions. In Assad *et al.* (2019), a fuzzy inference system was proposed to tune the noise covariance matrix of the EKF based on the filter innovation sequence through a covariance-matching technique. The experimental results showed that the fuzzy rule-based adaptive strategy effectively improved the estimation accuracy with respect to the standard EKF algorithm. In Al Mansour *et al.* (2019), an adaptive analytical algorithm was presented for the determination of UAV orientation angles. The algorithm employed both MARG and GPS-based correction channels; moreover, an UAV maneuver intensity classification method was implemented to increase the orientation estimation performance. Recent studies have proposed the use of unscented KF (UKF) over EKF Chiella *et al.* (2019); Kang *et al.* (2019), and stated that UKF-based approaches better deal with the high-order nonlinear terms of large attitude errors. Attitude estimation has been solved with computationally efficient geometric UKF Kang *et al.* (2019), where a new formulation of the UKF algorithm was proposed in Chiella *et al.* (2019) to maintain fast and slow variations in the measurement uncertainty. The latter algorithm was augmented with both an adaptive strategy to tune the covariance matrices on-the-fly and an outlier detector to reject the effects of external disturbances. An industrial manipulator robot was used to conduct the experiments, where the algorithm provided superior performance over the standard UKF and Madgwick filters. Recent developments have considered the MARG as a non-Gaussian stochastic system and developed maximum correntropy KF (MCKF) for attitude estimation Xi *et al.* (2017); Habbachi *et al.* (2018). These algorithms employed the MC criterion, instead of the minimum mean square error, to estimate the state of the system corrupted by non-Gaussian impulsive noises. However, the comprehensive case study provided in Kulikov and Kulikova (2018) has not highlighted the superior state estimation performance of the MCC-based techniques in non-Gaussian noise environments. These recent developments in the realm of Kalman-type filters are among the important techniques to be utilized in state estimation of non-Gaussian stochastic dynamic systems. Comprehensive overviews of (nonlinear) attitude estimation solutions are provided in Crassidis *et al.* (2007); Markley and Crassidis (2014).

Based on the methods discussed above, it can be concluded that the ultimate attitude estimation quality is determined by three main factors:

1. The first impact is related to the flexibility of the implemented algorithm (i.e., the observation models, equations defining the filter dynamics, and noise models jointly define the algorithm).

2. The filter performance heavily depends on properly selected filter gains (i.e., noise covariance matrices). In general, the statistics of system noise cannot be determined; moreover, external disturbances cause radical measurement noise during attitude realization, which make the assumed noise models inappropriate. This is even more critical problem for MEMS-IMU based orientation calculations of moving objects, since neither the external accelerations nor vibrations are deterministic, resulting in radical measurement noise that cannot be modeled appropriately. As a result, the filter parameters are usually selected based on both experimental and engineering intuition, which result in a compromise between the accuracy and filter dynamics, in which the ultimately determined noise covariance values both roughly describe the measurement noise and cover the model approximations. To enhance the filter performance, numerical optimization-based filter tuning has been proposed in Mazza *et al.* (2012); Gośliński *et al.* (2015); Kownacki (2011). To optimize, a test environment is created (with the assistance of other sensors or filters) in which the true state can be measured along with the IMU data. By evaluating the performance index, the KF noise covariance values are tuned with an optimization algorithm, such as the downhill simplex algorithm Powell (2002), neural-network based approach to tuning the noise statistics Korniyenko *et al.* (2005), simplex search method Kownacki (2011), differential evolution Salvatore *et al.* (2010) and genetic algorithms (GAs) Shi *et al.* (2002), PatternSearch algorithm Mazza *et al.* (2012), and particle swarm optimization (PSO) Gośliński *et al.* (2015).

3. The papers above show that the common methods used to deal with external disturbances (dynamic motions and magnetic perturbations) either work by the application of intelligent adaptive strategies that on-the-fly modify the vector observation methods, filter gains, and covariance matrices; or the compensation is maintained with additional dynamic models that well-mimic the effects of the external forces and magnetic fluctuations.

Observation: The discussion in the previous paragraphs illustrates that the procedure for selecting adequate filter parameters, thus providing maximized filter convergence, remains an important issue. Moreover, the investigation of whether considering the magnitudes of inherent external acceleration, vibrations and magnetic perturbations as disturbance magnitudes in the estimation algorithm can improve filter robustness and accuracy remains also an important issue. Therefore, to develop new algorithms that provide both reliable and robust attitude estimates, especially for extreme dynamic situations motivated the work during my research.

1.2 Research Objectives

Taking into account the continuously emerging potential of fuzzy logic and control, my main research goals has been summarized into two parts.

On one hand, my goal was to both investigate and measure the achievable fuzzy control performance, and moreover, through the optimization and validation steps design novel fuzzy

control structures that provide more robust control performance than conventional techniques. This procedure enabled to investigate whether the flexibility and expert oriented inference nature of fuzzy logic can provide significant benefits over linear control techniques during the stabilization of a real mechatronic system. Additionally, the objective was to derive such fuzzy control strategies that is characterized by simple structure and easy implementation, where such expert oriented design approach is employed which uses those simple heuristic knowledge oriented tools that fuzzy logic meant to offer.

On the other hand, my goal was to address the attitude estimation problem of mobile robots and propose novel soft computing-based approaches that improve the estimation performance. Therefore, such techniques were analyzed that enable to overcome the compromise solution related to ad hoc state estimator tuning by finding such estimator parameters that provide maximized state estimation performance. Additionally, this analysis also includes the development of advanced state estimator structures, where the estimator parameters are modified (via adaptive techniques) based on external system dynamics measures and thereby a superior estimator performance is achieved.

For the aforementioned research objectives, a mechatronic system was required that enables to implement, test, and validate the developed procedures. The WMP robot satisfies these requirements and well fosters the development of novel control and estimation techniques.

The research objectives and the relevant tasks are summarized as follows.

- Deriving a reliable mathematical model of the plant and creating its simulation environment. Then, developing both fundamental linear controller-based stabilization approaches and modern FLC-based solutions for the plant. Additionally, defining the control quality with performance indexes, and giving a detailed comparative assessment of the developed and realized control structures. At this stage the controller parameters are defined heuristically based on observations of the dynamics.

- Defining complex drive quality metrics, i.e., a complex cost (or fitness) function for the evaluation of the overall control quality; and applying numerical optimization to maximize the control performances, as well as, analyzing the advantages of fuzzy logic over linear techniques based on the results. Then, developing advanced FLCs based on heuristic knowledge that both provide efficient trajectory tracking and prevent high current peaks and jerks in motor drive system of robots.

- Developing a state estimator for the noisy states of the plant; and designing a test environment that enables simulations of various (accelerating and non-accelerating) system behaviors as well as measurement and qualification of the filter convergence. Then, analyzing both the state estimation performance based on quality metrics and the anomalies of fundamental estimation approaches. Applying numerical optimization to estimator parameters and achieving an optimized filter performance.

- Deriving a novel adaptive state estimator structure that fuses the magnitudes of the disturbances together and utilizes fuzzy-logic based heuristic IF-THEN rules that modify the parameters based on the dynamic behavior. Then, comparing the achieved estima-

tion performances to popular algorithms and proving that the developed solutions are competitive and even outperform the common methods.

- Extending the aforementioned results and formulating the extended, quaternion-based state estimator structure that incorporates the magnitudes of vibration, external acceleration, and magnetic perturbation by a sophisticated heuristic knowledge-based fuzzy inference machine to provide robust attitude estimation in both static and dynamic environments. Moreover, designing a test platform which enables both the execution of various dynamic (vibrating and accelerating) behaviors in the three-dimensional space and the measurement of true attitude angles along with the raw MARG data. This test environment contributes to both the successful evaluation of state estimation quality and validation of the methods.

1.3 The wheeled mobile pendulum system

The selected WMP system has two contact points with the supporting surface, moreover, the diameter of its IB is smaller than the diameter of the encompassing wheels resulting in two equilibrium points of the system (see Fig. 1.2).

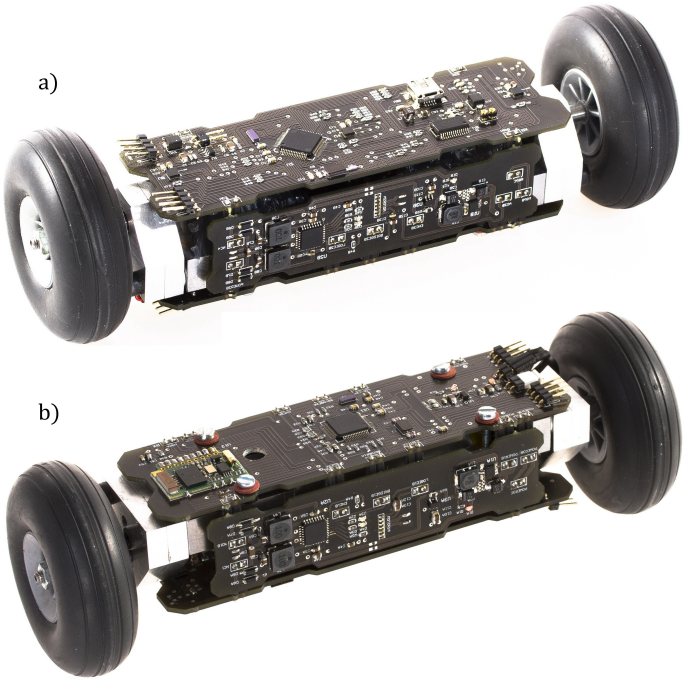

Figure 1.2: Photographs of the WMP system: around the (a) stable and (b) unstable equilibrium points.

Around the stable equilibrium point (when the center of mass is located below the wheel axis) the IB of the robot tends to oscillate when the wheels are actuated, while around the unstable equilibrium point (when the center of mass is located above the wheel axis) the robot self-balances its IB while performing translation motion. The wheels are actuated through DC motors attached to the IB. Due to this mechanical structure, the IB acts as a pendulum between the stator and rotor of the applied DC motors during the translation motion of the robot. Similar constructions are published in Salerno and Angeles (2007, 2003); Cazzolato *et al.* (2011). The

advantage of this mechanical construction is that even if the inverted pendulum falls and the center of mass of the inner body moves under the wheel axis (e.g. the inverted pendulum becomes a physical pendulum) the WMP system can be recovered by applying a swing-up control mechanism. It should be emphasized, that regardless of the chosen equilibrium point, the translation motion of the robot exclusively in closed loop, with the application of control algorithms can be resolved.

The dimensions (length, height and width) of the steel IB are 132, 32 and 34 mm, which is encompassed by 62 mm diameter wheels. The embedded electronic parts are placed around-, while the DC motors that drive the wheels are attached to the IB. In Fig. 1.3 the Solidworks CAD model is depicted which was used in the calculation of the inertia related parameters (the side and top printed circuit boards has been set to invisible in order to indicate the inner parts of the robot).

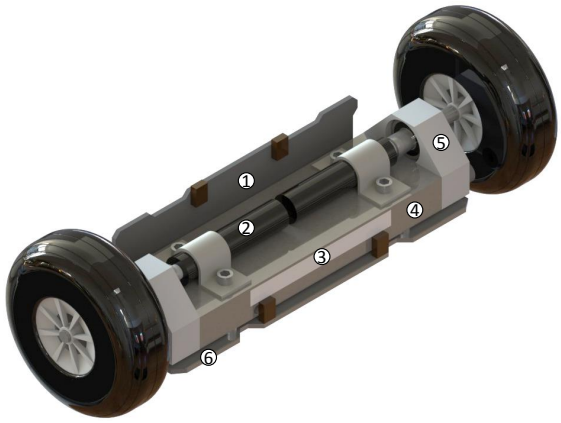

Figure 1.3: Solidworks CAD model of the robot. Inner parts: (1) side PCB, (2) DC motor, (3) battery, (4) chassis (IB), (5) bearings, and (6) bottom PCB.

The hardware construction is built around two 16-bit ultra-low-power Texas Instruments MSP430 F2618 microcontrollers (these MCUs are characterized with 16-bit, 16-MHz, 116-kB Flash, and 8-kB RAM; hereinafter MCU1 and MCU2). The applied sensors are summarized in Table 1.1. Low cost MEMS accelerometer (model No. LIS331DL) and gyroscope (model No. L3G4200D) sensors from STMicroelectronics are employed to measure the dynamics of the IB of the robot, and additionally, current sensors (model No. INA198) and two-channel incremental encoders (model No. PA2-100) are attached to both DC motors. The actuators are 3 V geared DC micromotors (model No. 1024N003S) manufactured by Faulhaber. The motors are driven with PWM signals through Texas Instruments DRV592 drivers. The electronic system is supplied from stabilized 3.3 V, the power source is a 1 cell Li-Po battery.

Table 1.1: The applied sensors in the embedded electronics of the robot.

Sensor	**Manufacturer**	**Type**	**Resolution**
Accelerometer	STMicroelectronics	LIS331DL	8-bit
Gyroscope	STMicroelectronics	L3G4200D	16-bit
Current sensors	Texas Instruments	INA198	0.0008V
Incremental encoders	Faulhaber	PA2-100	0.0141deg

Fig. 1.4 shows the embedded electronic configuration. MCU2 works as an IMU: it 1) collects the measurements from the accelerometer and gyroscope sensors through SPI peripheral, 2) performs the state estimation of the IB orientation and 3) sends the results to MCU1 via its UART interface. MCU1 performs basically the control task. On one hand, it collects the measurements (from incremental encoders, current sensors, and from MCU2 the orientation and angular velocity results). On the other hand, it drives the motors based on the applied control algorithm. MCU1 also sends the measurements to the PC through a Bluetooth module. A 16 MHz quartz oscillator is used as the system clock. A video demonstration of the system dynamics is available in the supplementary online material Odry (2019c).

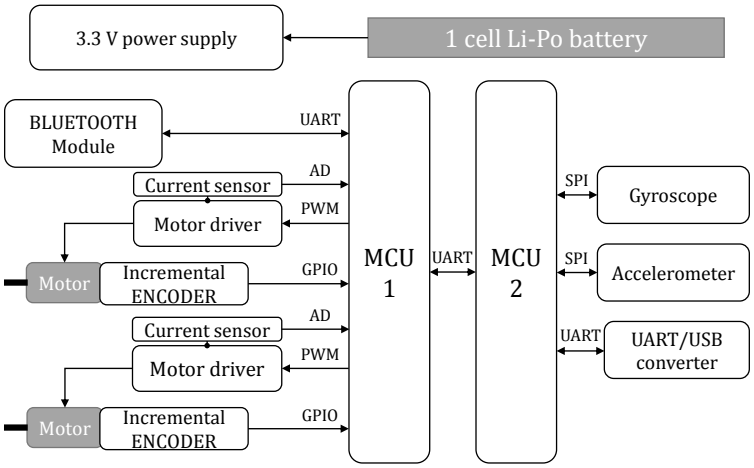

Figure 1.4: The hardware architecture of the robot.

1.4 Document Overview

The dissertation is structured as follows.

- Chapter 1.3: Introduces the selected mechatronic systems (i.e., the WMP robot) and describes both its basic electro-mechanical structure and control objectives. This content has been published in Odry *et al.* (2015a).

- Chapter 2: Describes the complete control system design problem, from mathematical modeling, over the development of both classical and modern control solutions, to both control system optimization and analysis of control performances. These results have been published in Odry *et al.* (2015a,b, 2016a,b, 2017a,b); Odry and Fullér (2018); Odry *et al.* (2020a).

- Chapter 3: Addresses the state estimation problem, analyzes both the fundamental methods and estimation performance enhancement techniques, moreover, the chapter describes the derivation of both a novel fuzzy-adaptive KF structure and its generalization for quaternion representation of orientation. These results have been published in Odry *et al.* (2018, 2020b).

- Chapter 4: Provides the overall conclusions of the previous chapters.

2 Control System Design

This chapter studies the control performances of modern and soft-computing based control solutions. The stabilization of a naturally unstable WMP is elaborated using LQG and cascade-connected fuzzy control schemes. The achieved control performances are analyzed both in simulation environment and with implementation results. A performance assessment of the elaborated control solutions is given based on both transient response and error integral measurements. Based on the comparative assessment, the achieved control performances of both control techniques are analyzed, moreover, the initial results of the resultant control performances are derived. Then, the performance enhancement of the control strategies is addressed, where a novel protective FLC is designed first which ensures both fast reference tracking and reduced jerks in the electro-mechanical parts of the system. Additionally, the achieved initial results of the comparative analysis are employed in control design optimization, where the parameters of each control technique is tuned with the aid of numerical optimization. Finally, the improved control performances are discussed and the advantages of the developed fuzzy control strategy is highlighted.

2.1 Mathematical Modeling

The original source is Odry *et al.* (2015a).

To be able to efficiently design the control algorithms of the system, its mathematical model has to be obtained first. Most of the electrical and mechanical parameters that characterize the robot (e.g., wheel radius, inertia matrix, and resistance of the motors) are quite accurately known from direct measurements, data-sheets or from calculations performed by Solidworks. The rest of the (mainly friction related) parameters were experimentally tuned based on the measurements results. The derived model forms the basis of the research analysis. Moreover, since the mechatronic system is equipped with different sensors that measure its dynamics, therefore both the implementation and validation of the theoretically proven control performances can be performed.

Many researchers use the Newtonian approach based formulation given in Grasser *et al.* (2002), or the formulation based on Euler-Lagrange equations defined in Pathak *et al.* (2005). It is also common to analyze the system dynamics with simplified mathematical models Guo *et al.* (2014); Zhou and Wang (2016b); Xu *et al.* (2013a). In the aforementioned formulations the dynamics of the applied actuators is not taken into account, and the driving torques are considered as inputs of the plant. However, the real input signals of the plant are the applied voltages (or PWM duty cycles) in most cases. In this section, a nonlinear 8-dimensional mathematical model of WMP systems is derived that takes into account the motor dynamics, and its inputs are the terminal voltages of the applied motors.

Based on Fig. 2.1 the geometric variables of the robot are introduced. I indicate with θ_1 and θ_2 the angular displacements of the wheels, while with θ_3 the oscillation angle of the IB. The parameters that characterize the robot are summarized in Table 2.1. The following notations

are used: $\dot{\psi}$ as the rate change of yaw angle of the robot, and $\dot{s}$ as the linear speed of the robot, i.e., $\dot{\psi} = r\left(\dot{\theta}_2 - \dot{\theta}_1\right)/d$, and $\dot{s} = r\left(\dot{\theta}_1 + \dot{\theta}_2\right)/2$, where r is the radius of the wheels, and d denotes the distance between them.

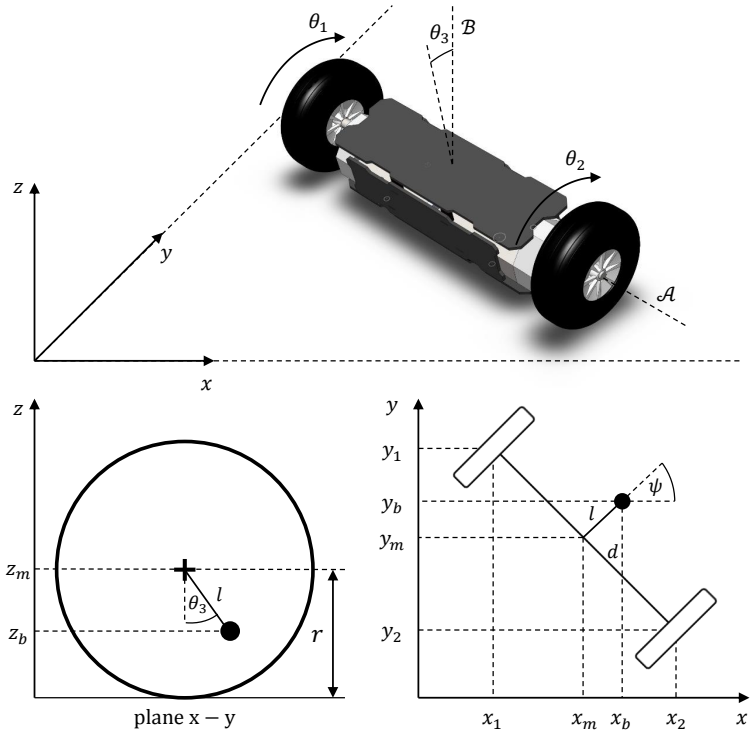

Figure 2.1: Plane and side view of the robot and its spatial coordinates.

Table 2.1: Notation of robot parameters

Symbol	Unit	Value	Parameter name
θ_1, θ_2	rad	-	angular position of the wheels
θ_3	rad	-	angular position of the IB
I	A	-	vector of motor currents I_1, I_2
u	V	-	vector of motor voltages u_1, u_2
τ_a	Nm	-	vector of torques transmitted to the wheels
τ_f	Nm	-	vector of friction torques
l	mm	8.36	distance between the center of mass and wheel axis
r	mm	31.5	radius of the wheels
m_w	g	31.5	mass of the wheels
d	mm	177	distance between the wheels
m_b	g	360.4	mass of the inner body
$J_{\mathcal{A}}$	gmm^2	81367	moment of inertia of the inner body about $\mathcal{A}$ axis
$J_{\mathcal{B}}$	gmm^2	574620	moment of inertia of the inner body about $\mathcal{B}$ axis
R	Ω	2.3	rotor resistance
L	μH	26	rotor inductance
k_E	mVs	2.05	back-EMF constant
k_M	mNm/A	2.05	torque constant
J_r	gmm^2	12	rotor inertia
f_m	mNms	0.021	viscous friction coefficient at the motors
f_w	mNms	0.18	viscous friction coefficient at the wheels
k	-	64	gear ratio of the gearbox

By the help of Fig. 2.1, the spatial coordinates of both the wheels and the IB are determined. Namely, the coordinates of the intersection of axes $\mathcal{A}$ and $\mathcal{B}$ are:

$$\begin{aligned} x_m &= \int \dot{s} \cos\psi \, dt, \\ y_m &= \int \dot{s} \sin\psi \, dt, \\ z_m &= r. \end{aligned} \tag{2.1}$$

Using the results of equation (2.1) and applying the trigonometric identities based on Fig. 2.1, the spatial coordinates of the wheels are derived:

$$\begin{aligned} x_1 = x_m - \frac{d\sin\psi}{2}, \;\; y_1 = y_m + \frac{d\cos\psi}{2}, \;\; z_1 = z_m, \\ x_2 = x_m + \frac{d\sin\psi}{2}, \;\; y_2 = y_m - \frac{d\cos\psi}{2}, \;\; z_2 = z_m. \end{aligned} \tag{2.2}$$

Similarly, the spatial coordinates of the IB are given by equation (2.3), where l denotes the distance of the center of mass from the wheel axis (see Table 2.1):

$$\begin{aligned} x_b &= x_m + l\sin\theta_3\cos\psi, \\ y_b &= y_m + l\sin\theta_3\sin\psi, \\ z_b &= z_m - l\cos\theta_3. \end{aligned} \tag{2.3}$$

The motion of the system is determined with the help of the Lagrange equations Bloch (2003); Sciavicco and Siciliano (2012):

$$\frac{d}{dt}\frac{\partial \mathcal{L}}{\partial \dot{q}} - \frac{\partial \mathcal{L}}{\partial q} = \tau, \tag{2.4}$$

where $q = (\theta_1, \theta_2, \theta_3)^T$ denotes the vector of generalized coordinates. Moreover, $\mathcal{L}$ defines the Lagrange function, which is defined as the difference of the kinetic and potential energies, i.e., $\mathcal{L} = K - P$. The total kinetic energy K consists of the sum of the kinetic energies that can be written for the wheels (K_w) and the kinetic energy characterized by the motion of the IB (K_b), i.e., $K = K_w + K_b$. The total kinetic energy of the wheels given by equation (2.5) is composed of the translational and rotational energies of the wheels. In equation (2.5) J_w and J_r denote the moment of inertia of the wheels and the motor, respectively, while k indicates the gear ratio and m_w is the mass of the wheels:

$$K_w = \sum_{i=1}^{2} \frac{1}{2} m_w \left(\dot{x}_i^2 + \dot{y}_i^2 + \dot{z}_i^2\right) + \sum_{i=1}^{2} \frac{1}{2} J_w \dot{\theta}_i^2 + \sum_{i=1}^{2} \frac{1}{2} k^2 J_r \left(\dot{\theta}_i - \dot{\theta}_3\right)^2. \tag{2.5}$$

The total kinetic energy of the IB consists of the energies resulting from the translational motion of the robot, the oscillation of the IB about axis $\mathcal{A}$, and the rotation about the $\mathcal{B}$ axis as well:

$$K_b = \frac{1}{2} m_b \left(\dot{x}_b^2 + \dot{y}_b^2 + \dot{z}_b^2\right) + \frac{1}{2} J_{\mathcal{A}} \dot{\theta}_3^2 + \frac{1}{2} J_{\mathcal{B}} \dot{\psi}^2, \tag{2.6}$$

where m_b denotes the mass of the body, while $J_{\mathcal{A}}$ and $J_{\mathcal{B}}$ are the moments of inertias of the body about the axis $\mathcal{A}$ and $\mathcal{B}$, respectively. The P potential energy stored in the system is:

$$P = 2m_w gr + m_b g\left(r - l\cos\theta_3\right), \tag{2.7}$$

where g denotes the gravitational acceleration. Based on equations (2.5), (2.6), and (2.7) the Lagrange function of the system $\mathcal{L}$ is derived (see section .1 in the appendix).

The vector of generalized external forces in equation (2.4) is defined as $\tau = (\tau_1, \tau_2, \tau_3)^T$. The generalized external forces consist of the external torques τ_a (that are produced by the motors) and the effect of friction τ_f modeled in the system, i.e., $\tau = \tau_a - \tau_f$. The external torques are described by equations (2.8) and (2.9), where the input voltage and current of the motors are denoted with $u = (u_1, u_2)^T$ and $I = (I_1, I_2)^T$, respectively. The relationship between the currents and input voltages is described by the fundamental differential equation. Namely, the input voltage equals to the sum of voltage drops generated on the inductance L and resistance R and the back-EMF voltage characterized by the constant k_E, based on Kirchhoff's circuit law:

$$\dot{I} = \frac{1}{L}\left(u - k_E k \begin{bmatrix} 1 & 0 & -1 \\ 0 & 1 & -1 \end{bmatrix} \dot{q} - RI\right). \tag{2.8}$$

Furthermore, the external torques are proportional with the rotor currents by the factor $k_M k$, where k_M is the torque constant:

$$\tau_a = k_M k \begin{bmatrix} 1 & 0 \\ 0 & 1 \\ -1 & -1 \end{bmatrix} I. \tag{2.9}$$

The friction model given by equation (2.10) consists of only viscous frictions, where viscous friction effects were modeled both at the bearings and between the wheels and the supporting surface:

$$\tau_f = \begin{bmatrix} f_{m,1} + f_{w,1} & 0 & -f_{m,1} \\ 0 & f_{m,2} + f_{w,2} & -f_{m,2} \\ -f_{m,1} & -f_{m,2} & f_{m,1} + f_{m,2} \end{bmatrix} \dot{q}. \tag{2.10}$$

By evaluating the Lagrange equation (2.4), the equations of motion of the mechanical system can be rewritten in the form:

$$M(q)\ddot{q} + V(q, \dot{q}) = \tau_a - \tau_f, \tag{2.11}$$

where $M(q)$ denotes the 3-by 3 symmetric and positive definite inertia matrix, $V(q, \dot{q})$ denotes the 3 dimensional vector term including the Coriolis and centrifugal force terms and also the potential (gravity) force term. The exact elements of the matrices are described in the appendix. Based on equation (2.11), the nonlinear state-space representation $\dot{x}(t) = h(x, u)$ of the plant

is obtained. With the state vector $x_{8\times1} = (q, \dot{q}, I)^T$ the state-space equation is given as:

$$\begin{aligned} \dot{x}(t) &= \begin{bmatrix} \dot{q} \\ M(q)^{-1}\left(\tau_a - \tau_f - V(q,\dot{q})\right) \\ \frac{1}{L}\left(u - k_E k \begin{bmatrix} 1 & 0 & -1 \\ 0 & 1 & -1 \end{bmatrix} \dot{q} - RI\right) \end{bmatrix}, \\ y(t) &= Cx(t). \end{aligned} \tag{2.12}$$

The output matrix C in equation (2.12) is chosen to produce the $y_{5\times1} = (\nu, \theta_3, \omega_3, \xi, I_\mathrm{A})$ output vector, where the following symbols are introduced for easier notation: $\nu = \dot{s}$ as the linear speed of the robot, $\omega_3 = \dot{\theta}_3$ as the oscillation rate of the IB, while $\xi = \dot{\psi}$ and $I_A = (I_1 + I_2)/2$ denote the yaw rate and average current consumption, respectively.

The numerical simulation of the mathematical model is performed in MATLAB Simulink environment. The state space representation defined by equation (2.12) is implemented with the help of the S-Function Simulink block. Since the robot is equipped with multiple sensors, measurements of the open-loop behavior have been recorded in order to both compare the simulation and measurement results and validate the derived mathematical model. The comparison of numerical simulation and real robot dynamics is depicted in Figs. 2.2 and 2.3. In the experiment, unit-step excitation of $u_1 = u_2 = 1.3$V was applied to both DC motors, and the average angular velocity of the rotors $\dot{\theta}_{rot}$, the angle θ_3 and angular velocity ω_3 of the IB, moreover, the average motor current I_A were recorded during the translational motion of the robot. Based on the comparison results, it can be concluded that the theoretically derived mathematical model with the nominal robot parameters (see Table 2.1) fairly describes the real behavior of the system.

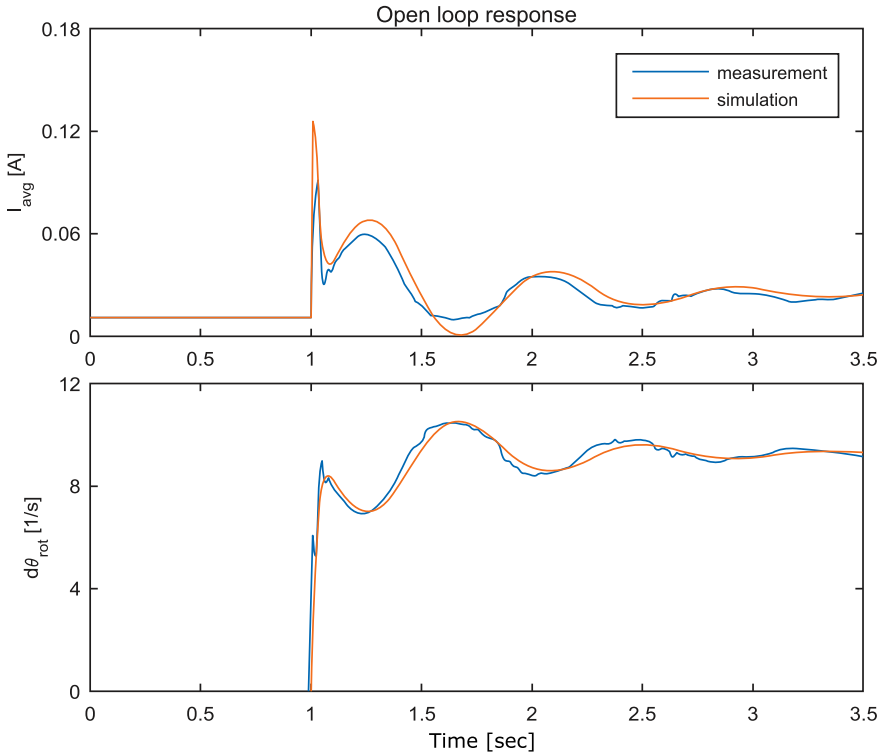

Figure 2.2: The resulting average current and average angular speed of the motors.

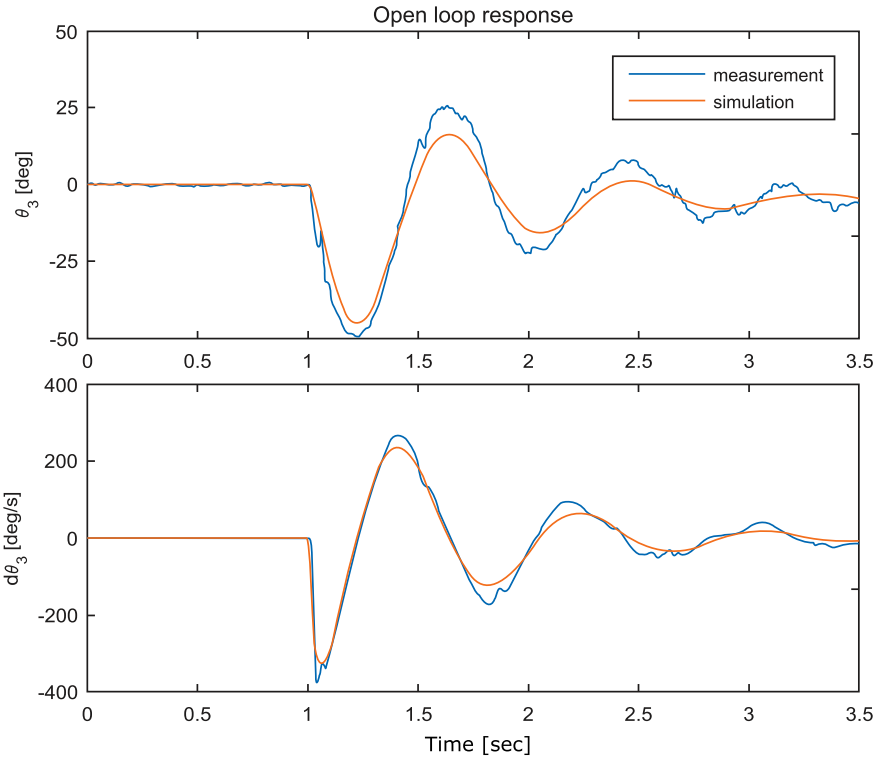

Figure 2.3: The resulting oscillation angle and angular velocity of the IB.

2.2 Development of Linear and Fuzzy Control Approaches

For the successful stabilization of the plant such control strategy is required which simultaneously suppresses the IB oscillations (around the equilibrium point) and ensures the desired planar motion of the robot. Let ν_d and ξ_d denote the desired values of the linear speed and yaw rate of the robot, respectively, then the control goals are summarized as follows. For the translational (linear) and rotational (yaw) motions $\lim_{t\to\infty} \dot{s}(t) = \nu_d$ and $\lim_{t\to\infty} \dot{\psi}(t) = \xi_d$ requirements should be satisfied, where the former requirement provides the linear displacement, while the latter requirement ensures the desired orientation of the robot. Moreover, the third requirement formulated as $\lim_{t\to\infty} \dot{\theta}_3(t) = 0$ ensures the suppression of the IB oscillations.

2.2.1 Linear Quadratic Gaussian Control

The original source is Odry *et al.* (2015b).

2.2.1.1 Algorithm

The LQR technique addresses the issue of achieving a balance between good system response and control effort Franklin *et al.* (1994); Lantos (2001). It is based on a developed mathematical algorithm which results the optimal state-feedback gain K. The feedback gain K minimizes the following quadratic cost function:

$$J(x,u) = \frac{1}{2}\sum_{k=0}^{N-1}\left(x_k^T Q x_k + u_k^T R u_k\right) + \frac{1}{2}x_N^T Q x_N, \tag{2.13}$$

where $x \in \mathbb{R}^n$ and $u \in \mathbb{R}^m$ are the state and input vectors of the system described in the state-space equation:

$$\dot{x} = Ax + Bu. \tag{2.14}$$

In equation (2.13) $Q = Q^T \in \mathbb{R}^{n \times n}$, $Q \geq 0$ and $R \in \mathbb{R}^{m \times m}$, $R > 0$ are weighting matrixes. Based on the LQR method, the state feedback matrix is given by $K = \left(R + B^T P B\right)^{-1} B^T P A$, where $P = P^T$, $P > 0$ is the unique solution of the Control Algebraic Riccati Equation (CARE). The optimal state-feedback $u_k = -Kx_k$ ensures the asymptotic stability of the closed loop system. The feedback matrix K can be calculated by the built-in Matlab function `lqrd(A,B,Q,R,Ts)`.

Since the LQR control defined by the objective function (2.13) drives the system from the initial state x_0 to the state $x_d = 0$, the control structure shall be extended with reference tracking matrices:

$$\begin{bmatrix} N_x \\ N_u \end{bmatrix} = \begin{bmatrix} A - I & B \\ C & 0 \end{bmatrix}^{-1} \begin{bmatrix} 0_{n \times m} \\ I_m \end{bmatrix}, \tag{2.15}$$

where 0 and I are the zero and identity matrices, respectively (and their sizes are given in the subscript). In the development of the optimal LQR control strategy it is assumed the state variables are measurable and the system is not disturbed by either internal or external noises. However in practice the opposite situation is quite common, namely, that a part of the measured state vector is too noisy to be used directly in the feedback. The LQG strategy provides optimal control gain to stochastic, noisy systems by minimizing the expected value of the quadratic objective function (2.13).

Based on the separation principle, the LQG control strategy is given by the state-feedback $u_k = -K\hat{x}_k$, where K is the optimal control gain determined by the LQR algorithm, while $\hat{x}_k$ state vector consists of the original states (i.e., the states of x_k that are not disturbed by noise) and the KF-based estimation of the noisy states. Let us denote the noisy state vector with ξ, then the corresponding noisy linear system can be given by:

$$\begin{aligned} \xi_{k+1} &= \Phi \xi_k + \Gamma \rho_k + \nu_k, \\ \gamma_k &= H \xi_k + z_k, \end{aligned} \tag{2.16}$$

where the process and measurement noises are indicated with ν_k and z_k, respectively, and according to the stochastic hypothesis these noises are uncorrelated and their mean value is zero. In this case the KF algorithm provides the optimal estimation $\hat{\xi}$ of the state ξ, i.e., $E\left[\xi_k - \hat{\xi_k}\right] = 0$ and $E\left[\left(\xi_k - \hat{\xi_k}\right)\left(\xi_k - \hat{\xi_k}\right)^T\right] \rightarrow \inf$. The estimation algorithm can be found in Welch and Bishop (2001) and both its performance evaluation and analysis are discussed in detail in chapter 3. As a result, the design steps of the LQG strategy are summarized as follows: 1) linearization of the mathematical model around the equilibrium point, 2) controllability analysis, 3) specification of the weighting matrices Q and R, 4) calculation of the optimal control gain K, 5) identification of the noisy state vector ξ, 6) specification of the noise covariance parameters of the filter, 7) state estimation with KF algorithm and 8) application of the state feedback strategy $u_k = -K\hat{x}_k$.

2.2.1.2 Elaboration of the Control Strategy

The goal of the elaboration procedure is to calculate the optimal state feedback K and reference tracking matrices N_x and N_u that drive the motors such a way that both the desired planar motion of the robot and the suppression of the IB oscillations are ensured. The linear state space equation of system dynamics is obtained via the linearization of equation (2.12) around the equilibrium point $(x_e, u_e) = (0, 0)$:

$$\dot{x} = \underbrace{\left(\frac{\partial h}{\partial x}\right)_{(x_e,u_e)}}_{A} x(t) + \underbrace{\left(\frac{\partial h}{\partial u}\right)_{(x_e,u_e)}}_{B} u(t). \tag{2.17}$$

In order to reduce the complexity of implementation the $\tilde{x} = Tx = \left(s, \theta_3, \dot{s}, \dot{\theta}_3, \psi, \dot{\psi}\right)^T$ coordinate transformation is applied. The resulting state-space representation is given by:

$$\begin{aligned} \dot{\tilde{x}} &= \tilde{A}\tilde{x} + \tilde{B}u \\ y &= \tilde{C}\tilde{x}. \end{aligned} \tag{2.18}$$

The controllability matrix is given by $M_c = \left(B, AB, ..., A^5B\right)$ Franklin *et al.* (1994); and the evaluation of its rank results in rank $M_c = 4$. Therefore, according to the Kalman rank condition for controllability (KRCC), the aforementioned system is not controllable since the dimension of the state vector is $\dim \tilde{x} = 6$. The non-controllable states of $\tilde{x}$ are the position s and orientation ψ. Thus, a new coordinate transformation $z = T_{C\bar{C}}\tilde{x}$ is defined, such that $T_{C\bar{C}} = (T_C, T_{\bar{C}})$ is a basis for $\mathbb{R}^6$, furthermore the columns of T_C form the basis for the controllable subspace, $\dim T_C = 6 \times 4$ and $\dim T_{\bar{C}} = 6 \times 2$. As a consequence of the definition, the state vector $z = (z_C, z_{\bar{C}})$ is clearly divided into two parts, namely $z_C = \left(\theta_3, \dot{s}, \dot{\theta}_3, \dot{\psi}\right)^T$ denotes the controllable state vector, while $z_{\bar{C}} = (s, \psi)^T$ contains uncontrollable states. The state-space representation becomes:

$$\begin{aligned} \dot{z} &= \begin{bmatrix} A_C & A_{C\bar{C}} \\ 0 & A_{\bar{C}} \end{bmatrix} z(t) + \begin{bmatrix} B_C \\ 0 \end{bmatrix} u(t), \\ y &= \begin{bmatrix} C_C & C_{\bar{C}} \end{bmatrix} z(t). \end{aligned} \tag{2.19}$$

The LQR strategy is elaborated by using the controllable subsystem (A_C, B_C). The weighting matrices $Q = \operatorname{diag} Q_{ii}$ and $R = \operatorname{diag} R_{jj}$ were defined heuristically as $Q_{11} = 14.5$, $Q_{22} = 156.2$, $Q_{33} = 1.3$, $Q_{44} = 1.3$ and $R_{11} = R_{22} = 0.1$. Solving the CARE the optimal control gain is obtained, while the reference tracking matrices are determined based on equation (2.15).

The KF is used to estimate the attitude θ_3 of the IB (second element of $\tilde{x}$). Since the accelerometer measures the projection of gravity vector onto its axes, the attitude is given by $\theta_{3,acc} = \operatorname{atan}(a_y/a_x)$ AN3182 (2010). Unfortunately, $\theta_{3,acc}$ is both very noisy and cannot be considered as an accurate derived quantity since the accelerometer measures both static and dynamic accelerations. Thus, it is common practice to consider the gyroscope and accelerometer as a noisy linear system and use the KF algorithm to estimate the state vector. The

corresponding state-space equation is given by:

$$\begin{aligned} \xi_{k+1} &= \begin{bmatrix} 1 & -T_s \\ 0 & 1 \end{bmatrix} \xi_k + \begin{bmatrix} T_s \\ 0 \end{bmatrix} \rho_k + \nu_k, \\ \gamma_k &= \begin{bmatrix} 1 & 0 \end{bmatrix} \xi_k + z_k, \end{aligned} \tag{2.20}$$

where the state vector $\xi = (\theta_3, \tilde{u})^T$ consists of the IB angle θ_3 and the bias of the gyroscope $\tilde{u}$. Furthermore, the input of the linear system is the angular velocity $\rho = \dot{\theta}_{3,gyro}$ (measured with the gyroscope), while the output of the system is the derived angle $\gamma = \theta_{3,acc}$ obtained from raw accelerometer measurements. Both the covariance matrices that characterize the measurement and state noises were derived based on offline measurements.

According to the separation principle, the LQG control strategies is elaborated as follows. The state feedback $u_k = -K\left(\hat{\theta}_3, \dot{s}, \dot{\theta}_3, \dot{\psi}\right)$ ensures the asymptotic stability of the closed loop system around the equilibrium point, where $\hat{\theta}_3$ denotes the KF-based estimation of the IB angle. Moreover, the optimal control gain K is obtained with CARE. The detailed control structure is depicted in Fig. 2.4.

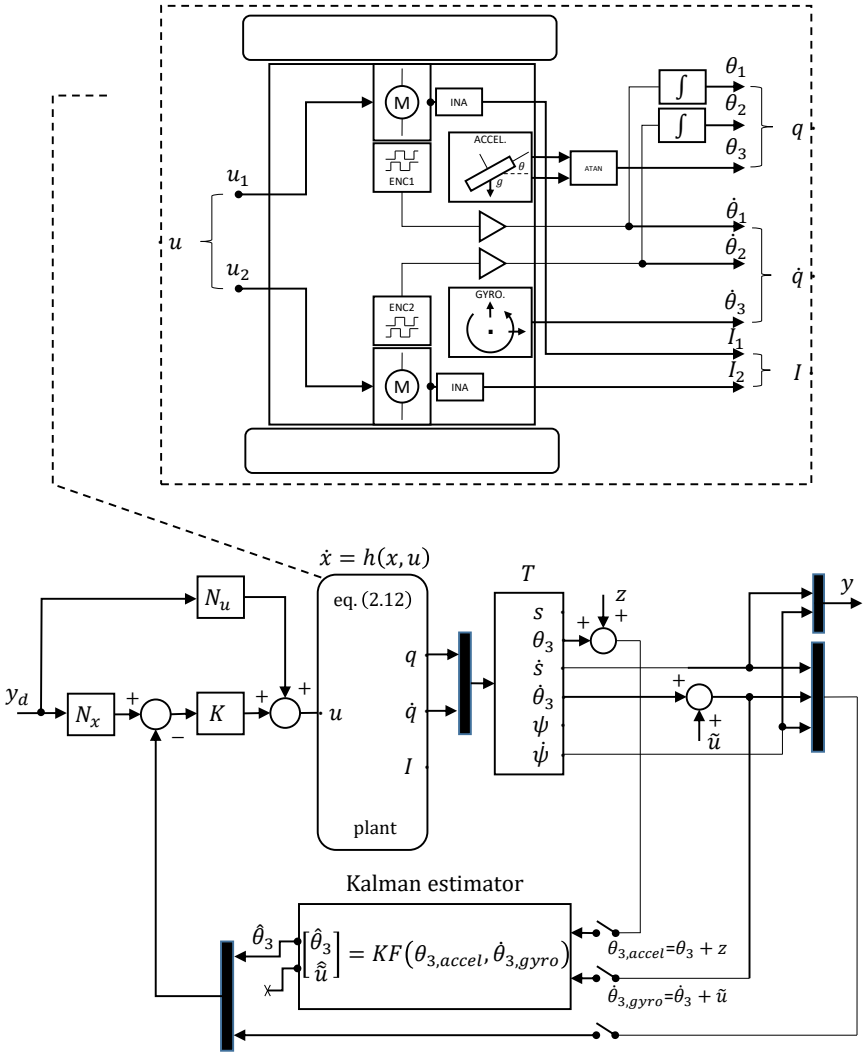

Figure 2.4: Detailed LQG control structure.

2.2.2 Fuzzy Control

The original source is Odry *et al.* (2016a).

2.2.2.1 Fuzzy Logic Controllers

Lofti A. Zadeh introduced the fuzzy sets Zadeh (1965) by extending the classical two-valued logic $\{0, 1\}$ with the whole continuous interval $[0, 1]$. This allows to introduce linguistic variables (such as small and large for reasoning about the current consumption) and associate them with membership functions. Fuzzy control is based on the application of these fuzzy sets, which result in that the inference mechanism of a FLC can be defined by simple IF-THEN linguistic rules. Hence, there is no need to define complex and precise models, instead the empirical rules and the approximate reasoning contribute to a heuristically defined control strategy. The FLC structure is depicted in Fig. 2.5 and its fundamental algorithm is composed of the following parts Wang (1997); Kóczy *et al.* (2000); Fullér (2000).

1. Fuzzification of the n-dimensional observation vector $\chi = (x_1, x_2, ..., x_n)$ and calculation of the firing values of the ith rule $(i = 1, ..., r)$ defined as:

$$R_i: \quad \text{IF } x_1 = X_1^i \text{ and } ... \text{ and } x_n = X_n^i \text{ THEN } y = B^i. \tag{2.21}$$

   Let χ_j denote the jth dimension of the observation vector, then the firing value γ_j^i represents the fitting degree of the observation χ_j to the antecedent fuzzy set X_j^i in the jth dimension of the ith rule as

$$\gamma_j^i = \max_{\chi_j}\{\min\{X_j^*(\chi_j), X_j^i(\chi_j)\}\}, \tag{2.22}$$

   where $X_j^*(\chi_j)$ is the fuzzified observation.

2. Calculation of the applicability measure of the ith rule, denoted by γ^i, as the minimum of the aforementioned firing values. This weight determines the significance of the consequent fuzzy set defined in the ith rule.

$$\gamma^i = \min_{j=1}^{n} \gamma_j^i \tag{2.23}$$

3. Calculation of the consequent fuzzy set $B^{i,*}$ in the ith rule (i.e., assigning the so-called firing level to the output fuzzy set defined in each rule) as the minimum of the applicability measure γ^i and the fuzzy set B^i defined in R_i:

$$B^{i,*}(y) = \min\left(\gamma^i, B^i(y)\right). \tag{2.24}$$

4. The summarized conclusion (total fuzzy output) is obtained as the union of all $B^{i,*}$ consequent fuzzy sets as:

$$B^*(y) = \max_{i=1}^{r} B^{i,*}(y). \tag{2.25}$$

5. In case of Mamdani architectures, the defuzzification process maps back the output fuzzy set to crisp domain. One of the common defuzzification techniques is the center of area (COA) method, which determines the COA of the summarized conclusion fuzzy set $B^*(y)$. The crisp output is calculated as:

$$y_{\text{COA}} = \frac{\int_{y \in B^*} B^*(y)\, y dy}{\int_{y \in B^*} B^*(y)\, dy}. \tag{2.26}$$

In case of zero-order Sugeno systems, constant singleton output membership functions define the conclusion in each rule, i.e., constant (not fuzzy) function $y = \kappa^i$ constitutes the consequent in the ith rule in equation (2.21) instead of the fuzzy set B^i. This increases computational efficiency and enables the computation of the crisp output y_0 as the weighted average over all rule outputs obtained in step 2:

$$y_0 = \frac{\sum_{i=1}^{r} \kappa^i \cdot \gamma^i}{\sum_{i=1}^{r} \gamma^i}, \tag{2.27}$$

where κ^i denotes the consequent (constant) singleton defined in the ith rule.

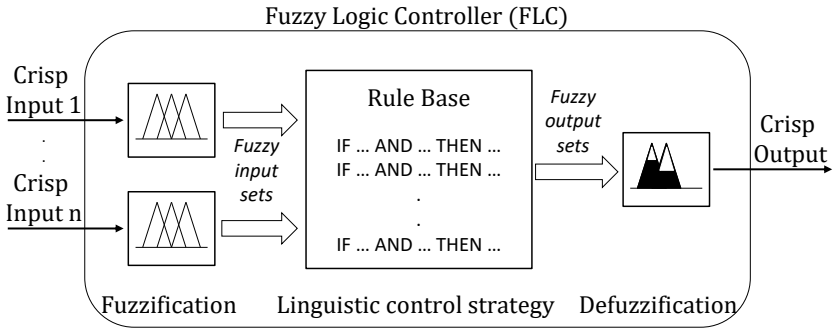

Figure 2.5: Structure of the fuzzy logic controller National (2018).

2.2.2.2 Elaboration of the Control Strategy

The goal is to design a heuristic fuzzy control scheme that drives both wheels through the actuators (DC motors) such a way that the robot can perform the prescribed control task. The developed fuzzy approach differs from the solutions given by Huang *et al.* (2011) and Xu *et al.* (2013a) in both the design and elaboration procedures. Namely, an expert oriented design approach is employed here, which uses those simple heuristic knowledge oriented tools (such as the definition of input-output relations with the help of linguistic variables and simple IF-THEN rules-based observations) that fuzzy logic meant to offer Wang (1997).

The elaboration of the fuzzy control strategy consists of defining the FLCs and a control scheme that satisfies the control requirements. This heuristic procedure starts by aggregating the deductions related to the behavior of the dynamical system using both observations and human common sense. In order to ensure the anti-sway control of the robot the following main deductions shall be implemented with the control scheme.

1. If the speed error (e_ν) is positive, then the control voltage (u_ν) shall be positive (and similarly the opposite scenario).

2. Moreover, the control voltage (u_ν) shall be modified (decreased or limited) in such a way to minimize the IB oscillations.

Based on both the aforementioned deductions and the results of LQG control, a control scheme that consists of three cascade-connected FLCs (hereinafter FLC1, FLC2, and FLC3) is proposed. This control scheme is depicted in Fig. 2.6, where the inputs and outputs of each FLC can be identified. Based on the aggregated initial deductions, both the corresponding input-output ranges and linguistic values are defined.

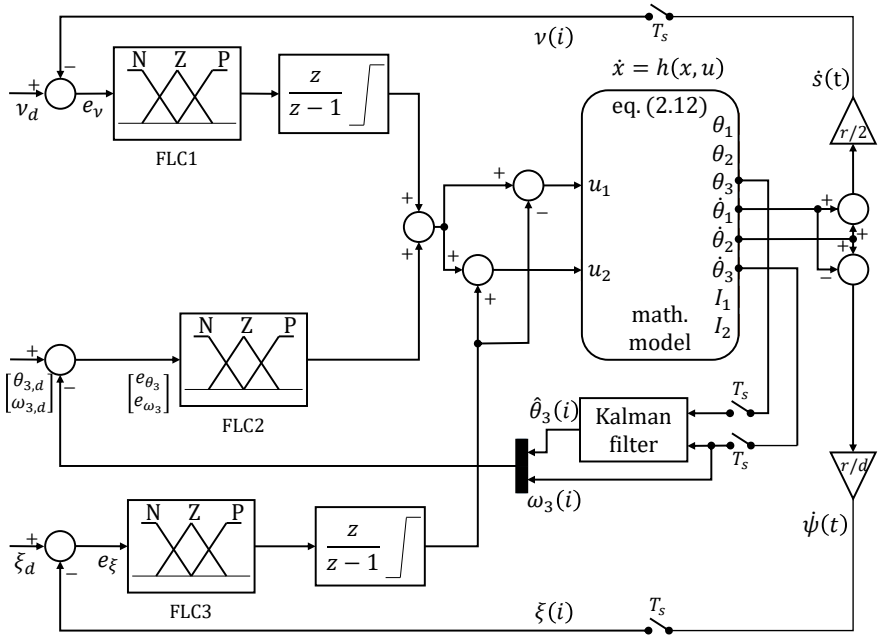

Figure 2.6: Block diagram of the applied control structure.

The design and tuning of each FLC is performed on an intuitive, heuristic manner. The membership functions related to the control variables are chosen with triangular and trapezoidal shapes, because those are commonly used in fuzzy control design. For the inputs of each FLC, three membership functions are chosen (by iterative tuning), uniformly distributed across their universes of discourse (see Fig. 2.7).

The control scheme is constructed using different PD-type and PI-type FLCs which are interconnected in cascade way. Table 2.2 summarizes the inference mechanism of the employed FLCs. Using the fuzzy sets N (negative), P (positive) and Z (zero) the fuzzy rules for the PD-type and PI-type FLCs are shown in Table 2.3. The exact antecedents and the consequent related to the tables are defined in the next paragraphs. The proposed architectures execute weighted average defuzzification. Since, the $T_s = 0.01$ s sampling time in taken into account (which equals to the sampling time of the applied sensors on the real robot), therefore, as an example $\theta_{3,k}$ denotes the discrete time domain equivalent of the sampled signal $\theta_3(t)$: $\theta_{3,k} = \theta_3(kT_s)$.

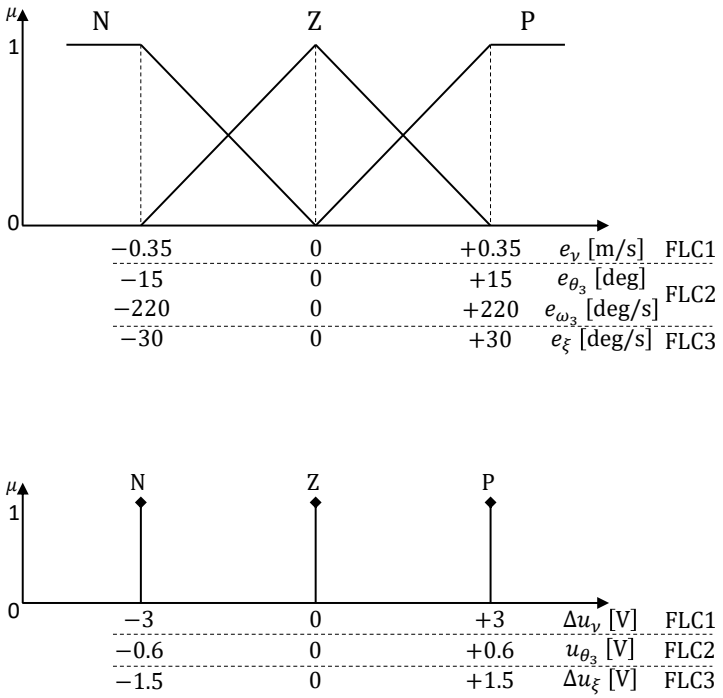

Figure 2.7: Membership functions of the employed FLCs.

Table 2.2: Properties of the employed controllers.

AND method	OR method	Implication	Aggregation	Defuzzification
MIN	MAX	MIN	MAX	Weighted average

Table 2.3: Rule base of PD and PI-type FLCs.

PD-type

Consequent		Antec. 2		
		N	**Z**	**P**
Antec. 1	**N**	N	N	Z
	Z	N	Z	P
	P	Z	P	P

PI-type

	Antec.		
	N	**Z**	**P**
Consequent	N	Z	P

FLC1 is responsible for the linear speed control of robot. The input (antecedent of each rule) of the controller is the speed error $e_{\nu,k} = \nu_{d,k} - \nu_k$, while the output (or consequent) is the variation of the command voltage $\Delta u_{\nu,k}$. As a result of iterative tuning ± 0.35 ms^{-1} and ± 3 V are established for the universes of discourse of e_ν and Δu_ν, respectively. Since the acceleration of the robot causes the oscillation of the IB (and we keep in mind that the differential term increases the sensitivity), a PI-type FLC is employed, whose fuzzy rules are defined in Table 2.3. Moreover, weighted average defuzzification is applied, therefore, the crisp control voltage $u_{\nu,k}$ for the speed control of the robot in the kth epoch is defined as:

$$u_{\nu,k} = u_{\nu,k-1} + \frac{\sum_{i=1}^{3} \gamma^i \left(e_{\nu,k}\right) \cdot \kappa^i}{\sum_{i=1}^{3} \gamma^i \left(e_{\nu,k}\right)}, \tag{2.28}$$

where $\gamma^i\left(e_{\nu,k}\right)$ returns the membership degree of the antecedent $e_{\nu,k}$ in the ith-rule and κ^i is the singleton consequent.

The aforementioned controller (FLC1) only partly ensures the linear displacement of the robot. Since the oscillation of the IB is not compensated, therefore the linear speed might fluctuate. The task of FLC2 is to suppress the IB oscillations. Since oscillation occurs whenever the robot accelerates, FLC2 is designed such a way to decrease the control voltage u_ν whenever oscillation is sampled. In this way the acceleration is restricted which results in the suppression of the oscillation. The inputs of the controller are the oscillation error $e_{\theta_3,k}$ and its time derivative $e_{\omega_3,k}$, while the output of the controller is the control voltage $u_{\theta_3,k}$. The applied triangular and trapezoidal membership functions are shown in Fig. 2.7. The universes of discourse of the input variables are defined based heuristic knowledge; for the oscillation error and its time derivative ± 15 deg and ± 220 degs^{-1} ranges are defined, respectively, while for the output control voltage ± 0.6 V is established. The employed fuzzy rules define a PD-type FLC (see Table 2.3). Similarly to FLC1, the crisp output of the controller is calculated using the weighted average method as:

$$u_{\theta_3,k} = \frac{\sum_{i=1}^{9} \min\left(\gamma^i\left(e_{\theta_3,k}\right), \gamma^i\left(e_{\omega_3,k}\right)\right) \cdot \kappa^i}{\sum_{i=1}^{9} \min\left(\gamma^i\left(e_{\theta_3,k}\right), \gamma^i\left(e_{\omega_3,k}\right)\right)}, \tag{2.29}$$

where $\gamma^i(e_{\theta_3,k})$ and $\gamma^i(e_{\omega_3,k})$ are the ith-rule fired membership function values and κ^i denotes the singleton value of the consequent weighting factor of the ith rule (see Fig. 2.7).

FLC3 controls the yaw rate of the robot. The input of the controller is the error $e_{\xi,k} = \xi_{d,k} - \xi_k$, while the output is the variation of the control voltage $\Delta u_{\xi,k}$. The universes of discourse of the input and output variables are chosen heuristically as ± 30 degs^{-1} and ± 1.5 V, respectively. The linguistic variables and membership functions are depicted in Fig. 2.7. By combining the output with an integrator, as depicted in Fig. 2.6, a PI-type FLC is employed, whose rule base is given in Table 2.3. The crisp control voltage of FLC3 is given as:

$$u_{\xi,k} = u_{\xi,k-1} + \frac{\sum_{i=1}^{3} \gamma^i\left(e_{\xi,k}\right) \cdot \kappa^i}{\sum_{i=1}^{3} \gamma^i\left(e_{\xi,k}\right)}. \tag{2.30}$$

The control voltages of the motors can be identified based on Fig. 2.6:

$$\begin{aligned} u_1 &= u_\nu + u_{\theta_3} - u_\xi, \\ u_2 &= u_\nu + u_{\theta_3} + u_\xi. \end{aligned} \tag{2.31}$$

2.2.3 Initial Control Performances

The original source is Odry *et al.* (2016b).

The control performances are studied both in simulation environment and on the real plant. A comparison is given by evaluating both the dynamic response of the closed loop system and the overall control performance.

2.2.3.1 Implementation of Algorithms

The simulation environment uses the mathematical model of the plant and the control structure to form the closed loop. Therefore, the closed loop consists of three main parts, namely, the plant (i.e., mathematical model (2.12)), the Kalman state estimator and the linear or fuzzy-based control algorithm. The numerical simulation of the proposed control strategies is performed in MATLAB Simulink environment. The FLCs are designed with the help of the Fuzzy Logic Toolbox of MATLAB, while LQG strategy is realized with simple gain blocks that implement the optimal control matrices. The simulation results of the closed loop behavior is depicted in Fig. 2.8.

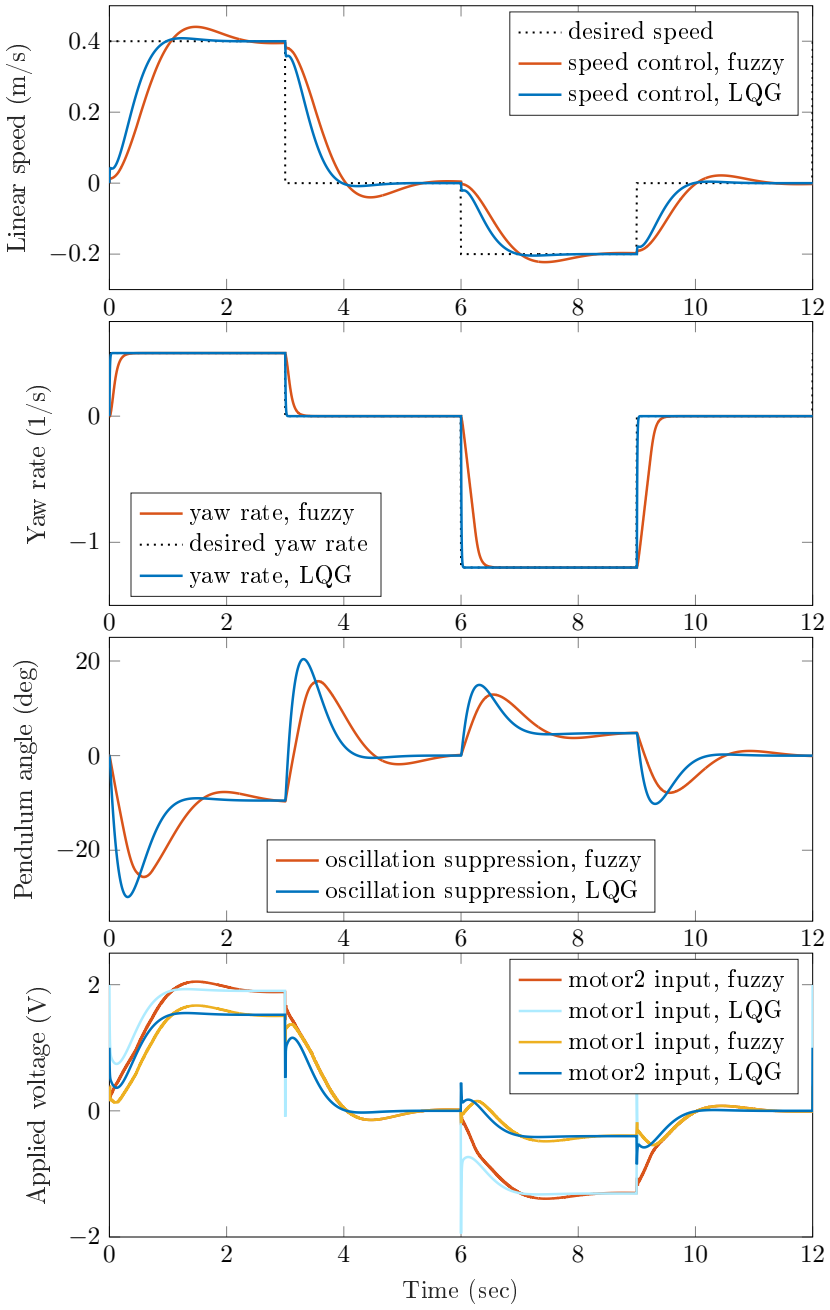

Figure 2.8: Closed loop behavior of the plant using the elaborated controllers (Simulation results).

From the top, the first subfigure is the linear speed $\dot{s}$ of the robot, the second shows the yaw rate $\dot{\psi}$, the third highlights the resulting IB oscillations θ_3 (IB angle), while the last one shows the applied voltages to the motors. The following reference signals were applied: $\nu_d = \{0.4, 0, -0.2, 0\}$ ms^{-1} for the linear displacement and $\xi_d = \{0.5, 0, -1.2, 0\}$ s^{-1} for the desired orientation. The simulation results show that both the linear control strategy and the cascade-connected fuzzy control scheme stabilize the dynamical system successfully. It can be seen that the elaborated controllers simultaneously ensure the translational motion (reference tracking performance is given in the first two subplots from the top of the figure) and the suppression of the IB oscillations (third subplot). In the simulation environment, the control strategies implement discrete-time controllers; the dynamics of the plant is sampled at fixed $f_s = 100$ Hz, which equals to the sampling frequency of the applied sensors.

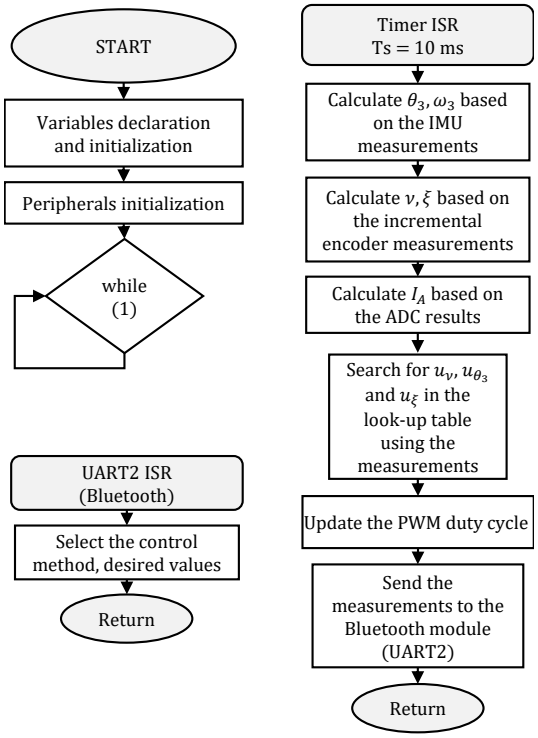

Figure 2.9: Flowchart of the embedded software.

Regarding the implementation on the real robot, the embedded software along with the control algorithms are coded in C language. MCU2 is programmed to work as an IMU, therefore it reads the data of sensors, executes the KF algorithm, and sends a package consisting of $\theta_{3,acc}$, ω_3, and $\hat{\theta}_3$ to MCU1 in every $T_s = 10$ ms, where $\theta_{3,acc}$ indicates the raw IB angle determined using the pure accelerations, ω_3 denotes the angular velocity of the IB measured by the gyroscope, while $\hat{\theta}_3$ indicates the KF-based estimation of the IB attitude. MCU1 executes the chosen control algorithm based on the collected measurements. Namely, it receives the package ($\theta_{3,acc}$, ω_3, $\hat{\theta}_3$) from MCU2 and extends it with the instantaneous position and velocity of the robot (s, $\dot{s}$) using the measurements of the incremental encoders (i.e., the state vector in equation (2.12) is determined). Once the measurements are obtained, the selected control algorithm both determines the instantaneous control signals and updates the duty cycle of the PWM generator. Both the measurements and control signals are calculated with floating point

operations, then the final results are converted to PWM duty cycles. These PWM signals are transmitted to H-bridges that drive the DC motors. Furthermore, the measurements and control outputs are sent to the PC user through a wireless (Bluetooth) module with $f_s = 100$ Hz frequency. A graphical user interface (GUI) written in MATLAB records the instantaneous measurements. The flowchart of the embedded software is depicted in Fig. 2.9.

The implementation of the LQG approach is rather straightforward; the optimal gains and reference tracking matrices are directly applied to weight the state vector for the calculation of the control outputs once the measurements are updated. The implementation of the fuzzy control strategy was based on the fuzzy surfaces (as an example Fig. 2.10 shows the fuzzy surface of FLC2).

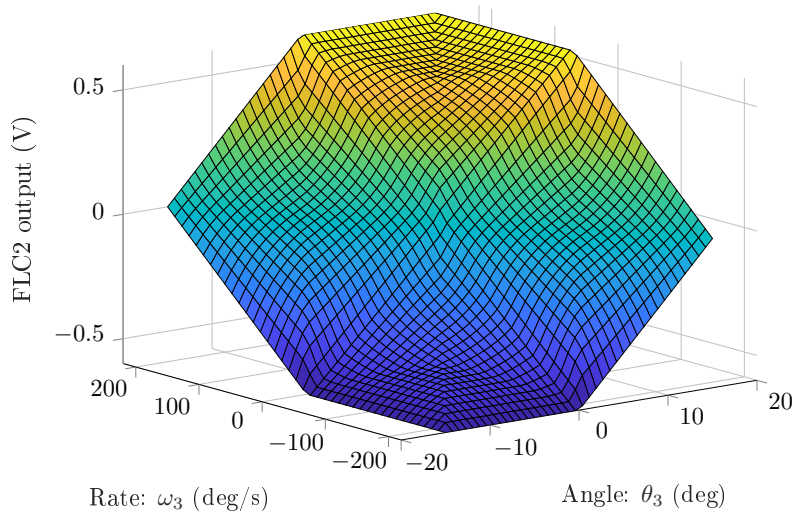

Figure 2.10: The implemented fuzzy surface of FLC2.

Since fuzzy surfaces define the output of the controller as a function of the instantaneous inputs, FLCs can be approximated with look-up tables (LUT). As a result, the crisp output of a FLC is obtained by searching in the table for the control output that is related to the measurements, i.e., each element of a LUT corresponds to certain input pairs. In this application the resolution of the implemented LUTs is 40×40, therefore the input ranges of each FLC are equidistantly divided into 40 input values. Three look-up table (hereinafter LUT1-3 as approximations of FLC1-3) are stored in the flash memory of MCU1, and the control voltages are obtained in each sampling time by searching in these tables based on the instantaneous measurements. LUT1-3 are generated by evaluating the possible input combinations and registering the corresponding control signal in a LUT for each FLC. Since, the motors are driven with 10-bit resolution PWM signals stored in 16-bit integer variables, therefore the size of a LUT is $M_{\text{LUT}} \approx 3.2$ kByte. This LUT based implementation method is suitable for small embedded processors and requires less calculation (significantly smaller computational time compared to the direct method, where fuzzification, implication, and defuzzification calculations are performed), because only the table indexes are needed to be calculated. The crisp output is selected based on the table indexes. However, the precision of the control output both depends on the LUT size and resolution of

the PWM signal. The proposed schemes in Figs. 2.4 and 2.6 are executed in each sampling epoch k based on the instantaneous measurements ν_k, ξ_k, $\hat{\theta}_{3,k}$ and $\omega_{3,k}$. The initial control performances are depicted in Fig. 2.11.

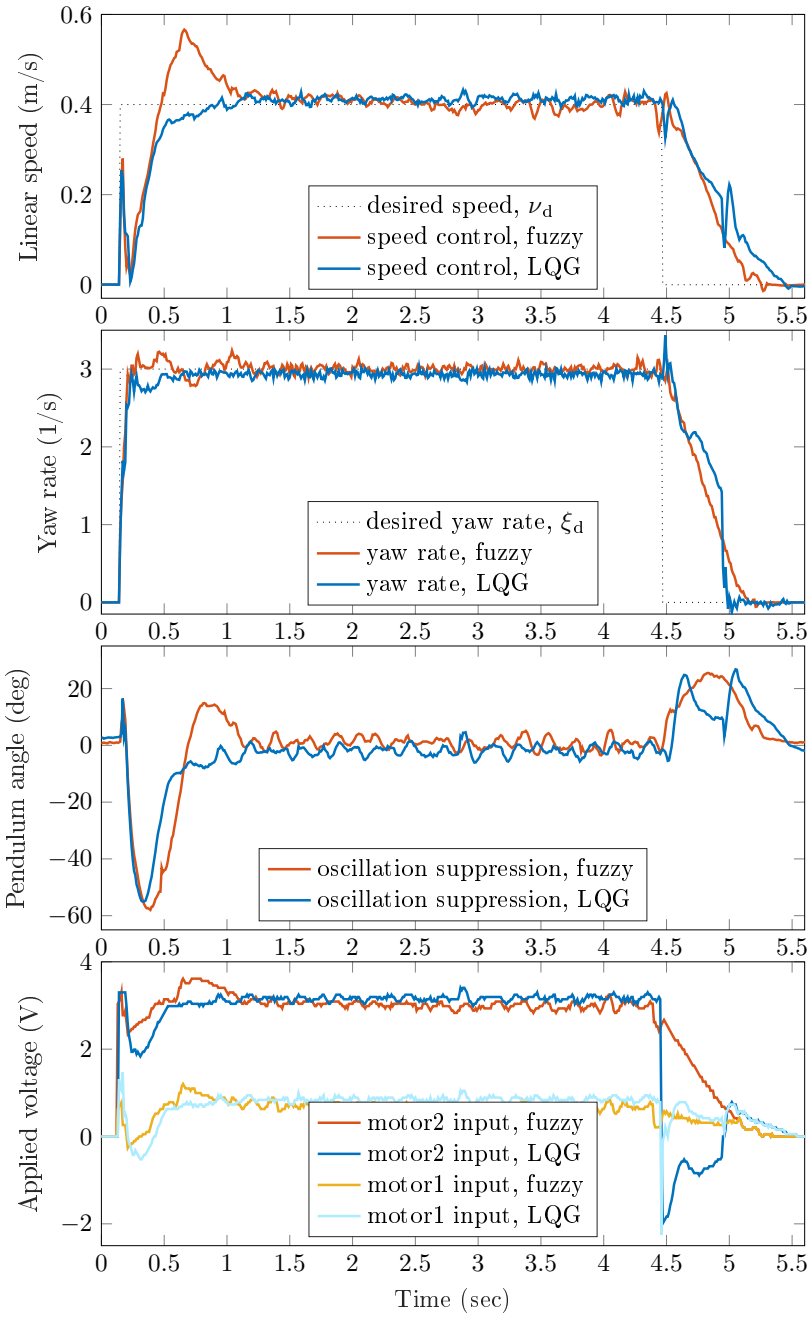

Figure 2.11: Control performances of the implemented LQG and fuzzy controllers (Measurements).

As an example, the row (ind_1) and column (ind_2) indexes and the crisp output (u_{θ_3}) of FLC2 are calculated as:

$$\begin{aligned} \text{ind}_1 &= \text{round}\left(e_{\theta_3} - e_{\theta_3}^{\min}\right)/\text{res}_1, \\ \text{ind}_2 &= \text{round}\left(e_{\omega_3} - e_{\omega_3}^{\min}\right)/\text{res}_2, \\ u_{\theta_3} &= \text{LUT}_2\left(\text{ind}_1, \text{ind}_2\right), \end{aligned} \tag{2.32}$$

where res_1 and res_2 denote the resolutions of the input ranges, while $e_{\theta_3}^{\min}$ and $e_{\omega_3}^{\min}$ indicate the least possible values of the inputs. In the implemented fuzzy control structure, the control signals of the motors are calculated as:

$$\begin{aligned} u_{1,k} &= \text{LUT}_1\Big|_{e_{\nu,k}} + \text{LUT}_2\Big|_{(e_{\theta_3,k},e_{\omega_3,k})} + \text{LUT}_3\Big|_{e_{\xi,k}}, \\ u_{2,k} &= \text{LUT}_1\Big|_{e_{\nu,k}} + \text{LUT}_2\Big|_{(e_{\theta_3,k},e_{\omega_3,k})} - \text{LUT}_3\Big|_{e_{\xi,k}}, \end{aligned} \tag{2.33}$$

where the output signals $u_{\nu,k}$, $u_{\theta_3,k}$ and $u_{\xi,k}$ are selected in LUT1-3 based on both equation (2.32) and the corresponding error signals ($e_{\nu,k}$, $e_{\theta_3,k}$ and $e_{\omega_3,k}$ or $e_{\xi,k}$).

Similarly to the simulation results, the first subplot in Fig. 2.11 shows the achieved linear speed of the robot $\dot{s}$, the second subplot highlights the yaw rate $\dot{\psi}$, the third is the instantaneous angle θ_3 of the IB, while the last subplot indicates the applied voltages. It can be seen that both implemented control strategies successfully suppress the IB oscillations and ensure the translational motion of the robot. In the experiment, the desired speed and yaw rate have been set to 0.4 ms^{-1} and 3 s^{-1}, respectively (dotted lines in Fig. 2.11).

2.2.3.2 Evaluation and Comparison

Based on Figs. 2.8 and 2.11, it is concluded that the elaborated control schemes ensure asymptotic system behavior, however the control quality needs to be determined. This section quantifies the control performances by evaluating different error integral formulas, moreover, a comparative assessment is given based on the achieved simulation and measurement results.

For the comparison of the elaborated control strategies both the transient responses and overall control performances are analyzed. This comparison is based on the closed loop behavior in time domain. For the quality measurement of reference tracking and suppression of IB oscillations four different error integrals are evaluated, namely these measures are the sum of absolute errors (SAE), sum of square errors (SSE), sum of discrete time-weighted absolute errors (STAE), and the sum of discrete time-weighted square errors (STSE) defined by equations (2.34) and (2.35), respectively Barton (1996):

$$\text{SAE}(e) = \sum_{k=1}^{N} |e_k|, \quad \text{SSE}(e) = \sum_{k=1}^{N} e_k^2, \tag{2.34}$$

$$\text{STAE}(e) = \sum_{k=1}^{N} kT_s |e_k|, \quad \text{STSE}(e) = \sum_{k=1}^{N} kT_s e_k^2, \tag{2.35}$$

where N denotes the length of the measurement, and e defines the error vector ($\dim e = N$), which is the difference of the desired and realized values; in case of reference tracking $e = e_\nu$ or $e = e_\xi$, while in case of the suppression of the IB oscillations $e = e_{\omega_3} = -\omega_3$ (since the desired rate of oscillation is zero). By evaluating the aforementioned quality-measurement formulas the initial control quality results are obtained. These initial results can be used in the formulation of a complex fitness function to both evaluate the overall control performance and optimize the controllers, thereby achieving enhanced control quality.

Based on the simulation and implementation results the qualitative characteristics of the elaborated controllers is summarized in Table 2.4, where T_{rise} indicates the rise time, $T_{5\%}$ denotes the settling time and *ovs.* is used for the abbreviation of overshoot. According to the simulation results, the linear control strategy provides faster closed loop behavior with smaller reference tracking overshoots. From Table 2.4, it can also be read that the elaborated fuzzy scheme satisfies the control requirements with much bigger overshoot (0.036 ms^{-1} at 0.4 ms^{-1} reference speed), and due to the PI-type controllers it provides less aggressive closed loop behavior than the linear controller. Regarding the suppression of the IB oscillations, both controllers perform the task similarly; the overshoot (i.e., maximum oscillation angle) is between $25 - 30$ degrees. These simulation results well predict the outcome of the comparison related to the implemented controllers. The measurement results also prove that the linear control strategy ensures faster system response and smaller overshoots. Regarding the fuzzy control, the big overshoot is quite conspicuous (measurement results in Fig. 2.11), and also, slower settling time characterizes the weaker performance of the fuzzy control scheme. Both realized controllers successfully suppress the IB oscillations with similar quality (e.g., the maximum overshoot is around 55 degrees).

Table 2.4: Characteristics of the controllers.

	Planar motion of the robot			
	Simulation		**Implementation**	
	Linear	**FUZZY**	**Linear**	**FUZZY**
T_{rise}(s)	0.73	0.9	0.38	0.27
$T_{5\%}$(s)	0.82	1.78	0.38	0.83
ovs.(ms^{-1})	0.0083	0.036	0.018	0.14

	Suppression of the IB oscillations			
	Simulation		**Implementation**	
	Linear	**FUZZY**	**Linear**	**FUZZY**
ovs.($^\circ$)	29.9	25.6	52.7	56.3
T_{5°(s)	0.85	1.19	0.71	0.91

According to the figures, it can be concluded that more satisfying control performance is achieved by the linear control technique. The reason of the modest performance of the elaborated fuzzy control scheme could have different sources. It is important to mention that the realized controllers are the results of intuitive control design steps, which means that the linear controller has been defined by selecting the Q and R weighting matrices (and taking into account the plant dynamics), while the inference mechanism of fuzzy control strategy has been defined by the selected membership functions and rules. Moreover, it shall be kept in mind that the derived mathematical model (see equation (2.12)) has not been validated, since the nominal (or calculated) values of both inertia related (i.e., inertia matrix and center of mass) and electrical parameters (such as the resistance or inductance of the motor) of the robot were used in the development procedure. The result of the not validated mathematical model can also be seen in Table 2.4, since significant differences between the simulation and implementation results are highlighted. In fact, it was expected that the performance of the realized controllers will differ from the simulation results since the design procedure of the linear control takes into account the mathematical model as a constraint equation (which is only approximately known), ultimately this difference led the system to a better closed loop behavior.

The evaluation of the quality measurement formulas (2.34) and (2.35) are summarized in Table 2.5. The outcome of the evaluation results concludes controversy, since according to the calculated error integrals, the better overall control performance is provided by the fuzzy control scheme. The last column of Table 2.5 indicates that according to the SAE, STAE, and STSE quality measurement formulas the realized fuzzy control scheme results smaller aggregated error values. The rows of Table 2.5 define the chosen error integral formula, while the first three columns define the aggregated error values related to the errors e_ν, e_ξ and e_{ω_3}. The overall aggregated error value (total error) is defined by multiplying the sub-aggregated error values, for example, in case of SAE:

$$\mathrm{SAE}_{\mathrm{overall}} = \log_{10} \prod_{e \in \{e_\nu, e_\xi, e_{\omega_3}\}} \mathrm{SAE}\,(e)\,. \tag{2.36}$$

The ultimate outcome of the comparison is that the linear control strategy provides better transient system responses, however, the better overall control performance is achieved by the cascade-connected fuzzy control scheme. Through this analysis, it has been shown that approximate reasoning and heuristic knowledge oriented development give satisfying control performances. This suboptimal control solution is further investigated and improved in the next section by using the quality measurement formulas (2.34) and (2.35) in an optimization procedure. In this optimization procedure, the linear control gains as well as both the shape of the membership functions and their ranges are optimized for a better overall control performance.

Table 2.5: Quality measurement numbers.

	Fuzzy control			
	e_ν	e_ξ	e_{ω_3}	$\log_{10}\Pi$
SAE	30.4780	128.7299	$4.2689 \cdot 10^3$	7.2240
SSE	6.5300	218.3223	$1.1638 \cdot 10^5$	8.2199
STAE	85.6093	512.2402	$9.4892 \cdot 10^3$	8.6192
STSE	20.3829	955.1933	$1.6724 \cdot 10^5$	9.5127

	Linear control			
	e_ν	e_ξ	e_{ω_3}	$\log_{10}\Pi$
SAE	30.8451	150.3294	$3.7218 \cdot 10^3$	7.2370
SSE	6.9708	265.7726	$8.0833 \cdot 10^4$	8.1754
STAE	101.2168	581.9903	$9.1477 \cdot 10^3$	8.7315
STSE	23.8399	1169.0301	$1.2966 \cdot 10^5$	9.5579

2.3 Enhancement of Control Performances

Although, the heuristically defined controllers (developed with empirical rules, weighting gains, input-output ranges and heuristically tuned membership functions) in section 2.2 roughly meet the design requirements, only suboptimal control performances are obtained (since the parameters were selected experimentally, which do not results in maximized control performance, rather a compromise solution). The suboptimal control performance can be further improved by trial and error tuning. However, the engineering intuition-based iterative tuning becomes

rather difficult if complex nonlinear systems with high order dynamics are controlled. Moreover, this way the best (or maximized) control performance is not guaranteed. This tuning problem can be realized with numerical optimization, which replaces the designer's tedious, iterative task and tunes (optimizes) the control parameters by locating the minimum of the formulated fitness function the characterizes the control quality.

This section addresses the preceding problem and describes both design improvement and optimization approaches for the control structures developed in the previous section. First, the observations of system dynamics is employed and both new linguistic variables and IF-THEN rules are introduced for the enhancement of the fuzzy control scheme. The results of the investigation is a special PI-type FLC, which simultaneously ensures the translational motion and prevents high current peaks and jerks in the motor drive system of the robot. Then, a complex fitness function is formulated for the quantification of the overall control performance to investigate and measure the achievable control performances. In this fitness function, the quality of reference tracking, the efficiency of the suppression of IB oscillations and the magnitude of current peaks in the driving mechanism are considered. Using the defined fitness function, the optimization of the parameters of both linear and fuzzy control schemes is realized with the aid of particle swarm optimization (PSO), yielding the enhanced (maximized) control performances.

2.3.1 Protective Fuzzy Control

The original source is Odry *et al.* (2017b).

To enhance the initial performance of fuzzy control a special nonlinear PI-type FLC is developed and applied in the control scheme, which results in both fast reference tracking and significantly reduced jerks and current peaks in the motor drive system. This PI-type FLC allows to protect the electro-mechanical parts of the plant, moreover, it ensures fast closed loop behavior. The resultant protective FLC can be employed universally for plants that highly require the vibrations and jerks to be reduced in their electro-mechanical parts Carbone (2011); Kecskés and Odry (2018). The modified control structure that contains the nonlinear PI-type FLC is depicted in Fig. 2.12.

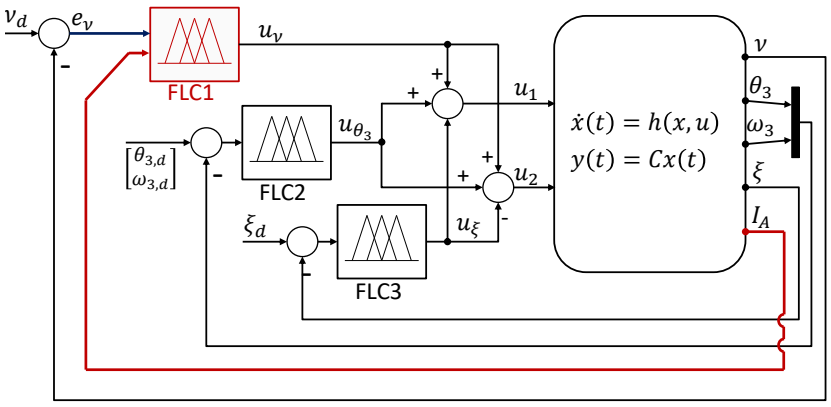

Figure 2.12: Block diagram of the modified fuzzy control structure.

FLC2 and FLC3 are the same structures as introduced earlier, their parameters, membership functions and rule bases are described in Figs. 2.5 and 2.7 and with Tables 2.2 and 2.3. The protective PI-type FLC is denoted with FLC1 (red block in Fig. 2.12) and its complete structure is shown in Fig. 2.13. The task of this controller is to both ensure the MWP's translational motion and reduce the current peaks in the motor drive system. Therefore, the linear speed error e_ν and the average motor current I_A form the inputs of the controller. The control signal is denoted with u_ν and is a combination of the crisp proportional and integral tags (first and second outputs of the FLC, see Fig. 2.13). The rule base shall be defined based on the following facts:

1. IF the speed error (e_ν) is positive (negative), THEN positive (negative) control action (u_ν) is applied, however

2. IF in the same time the motor current I_A is large, THEN the aforementioned control action (u_ν) is decreased with positive (negative) protective voltage to reduce the current peak.

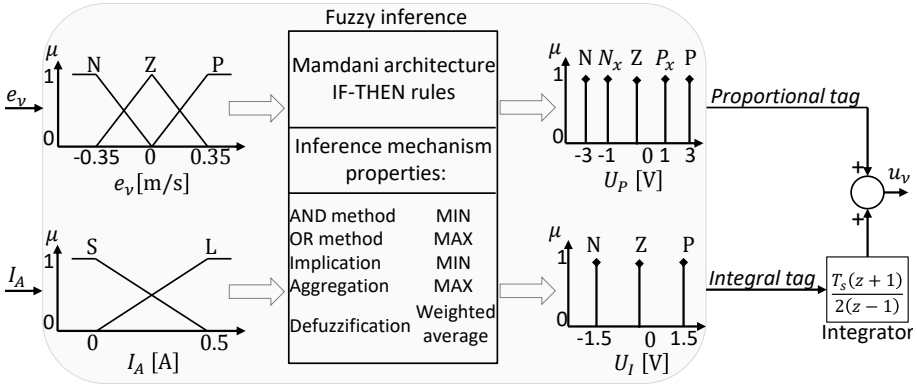

Figure 2.13: Structure of the protective FLC (FLC1).

The aforementioned deductions are expanded into six rules given in Table 2.6. Three membership functions are chosen to describe the speed error with the fuzzy sets N (negative), P (positive) and Z (zero). The motor current is characterized by S (small) and L (large) fuzzy sets. Only the proportional tag (first output) is influenced by the protective mechanism, since the integral tag has slower control action dynamics. The protective mechanism is characterized by Nx and Px fuzzy sets describing the negative and positive protective voltages, respectively. The protective nature of FLC1 is well demonstrated by its fuzzy surface depicted in Fig. 2.14. It can be observed that FLC1 works as a nonlinear P controller, whose control action is decreased as the motor current increases. This non-linearity both produces smoothness in control and allows to reduce the current peaks and jerks in the electro-mechanical parts of the MWP. As a result, FLC1 has a protective PI-type structure, which takes into account the average motor current I_A beside the speed error signal $e_\nu = \nu_d - \nu$, where the fuzzy rules have been established such a way to both ensure the desired linear speed and reduce the current peaks and jerks in the motor drive system.

Table 2.6: Rule base of the protective FLC (FLC1).

	Speed error: e_ν	**Motor current:** I_A	**Proportional tag:** U_P	**Integral tag:** U_I
1	Z	-	Z	Z
2	P	-	P	P
3	N	-	N	N
4	Z	S	Z	-
5	P	L	Px	-
6	N	L	Nx	-

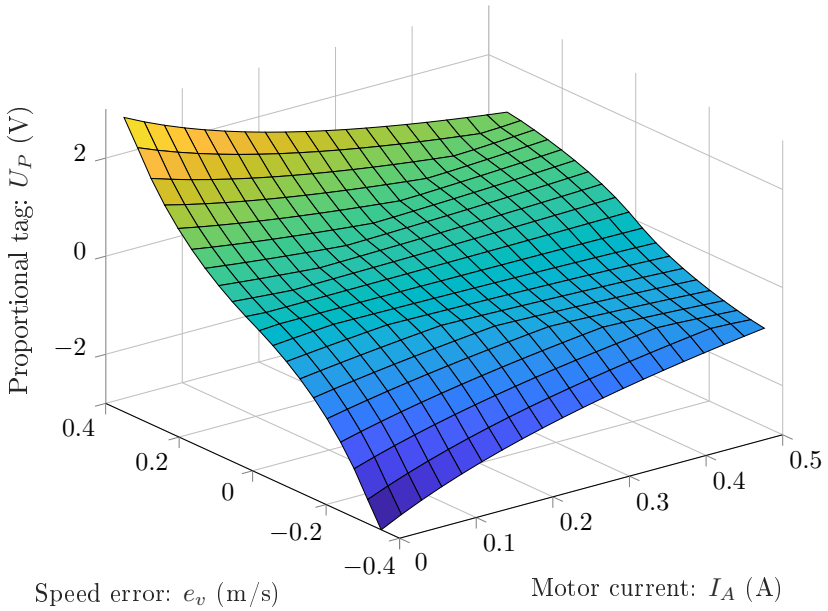

Figure 2.14: The generated fuzzy surface related to the rule base of FLC1.

2.3.2 Equivalent PID Controllers

Since the elaborated LQR technique comprises of simple gains that weight the state vector, moreover, the state vector contains the generalized coordinates q and their time derivatives $\dot{q}$ of the system, therefore the developed LQR approach can be replaced with simple PD controllers. Additionally, the fuzzy scheme also employs nonlinear PD-type and PI-type FLCs for the stabilization of the plant. As a result, a general linear control structure is derived as the equivalent linear scheme of the fuzzy approach, where three PID controllers are employed instead of FLCs. These PID controllers will be tuned in the optimization problem with numerical optimization.

PID controllers provide control signals that are proportional to the error between the desired and actual output, to the integral of the error, and to the derivative of the error Tang *et al.* (2001). The output (or control) signal and the corresponding transfer function in continuous-time are formulated as:

$$\begin{aligned} u(t) &= K_P e(t) + K_I \int_0^t e(\tau)\, d\tau + K_D \frac{de(t)}{dt}, \\ C(s) &= K_P + K_I \frac{1}{s} + K_D s, \end{aligned} \tag{2.37}$$

where $e(t)$ denotes the error signal, s is the Laplace operator, and K_P, K_I and K_D are the parameters of the controller to be tuned. Since, the controller is employed in digital domain its

discretization is realized by converting the integral and derivative terms to their discrete-time counterpart. Applying the Tustin approximation, the transfer function of a discrete-time PID controller is represented by

$$C(z) = K_P + \frac{K_I T_s}{2}\frac{z+1}{z-1} + \frac{2K_D}{T_s}\frac{z-1}{z+1}. \tag{2.38}$$

The equivalent linear control structure is formed by replacing the FLCs with discrete-time transfer functions (2.38). Similarly to the fuzzy scheme, PID1 is responsible for the linear speed control of the plant, where the error and control signals are e_ν and u_ν, respectively. PID2 ensures the suppression of the IB oscillations with its input-output signals e_{θ_3} (oscillation error) and u_{θ_3} (control action). However, the yaw rate controller (FLC3) is not replaced nor optimized, since its dynamics does not influence the overall control quality (i.e., translational motion, IB oscillation and current peaks) significantly. The initial parameters are selected experimentally as $K_{P,1} = 12$, $K_{I,1} = 25$ for PID1, and $K_{P,2} = 0.03$, $K_{D,2} = 3 \cdot 10^{-5}$ for PID2.

2.3.3 Optimization of Control Approaches

The original sources are Odry *et al.* (2017a) *and* Odry and Fullér (2018).

In order to both measure the achievable control performance and obtain maximized the control quality, the optimization of both linear and fuzzy control approaches is realized with the aid of PSO. This parameter tuning procedure consist of three parts, namely, the definition of a complex cost function for the evaluation of the overall control quality, selection of the parameters sets to be tuned, and the application of the optimization algorithm to tune the parameters by minimizing the defined cost function. The optimization algorithm outputs the optimal possible PID and FLC parameters (i.e., the most appropriate linear gains, fuzzy membership functions and input-output ranges). To conduct a fair comparison, both control approaches are optimized in the same environment using the same data set, requirements and optimization procedure. Moreover, the fitness function shall be selected such a way to make the optimized PID and fuzzy control structures provide both fast system dynamics and reduced IB oscillations, jerks, and current peaks in the motor drive system.

2.3.3.1 Parameters of the Controllers

The main parameters that determine the fuzzy approach are related to the shapes and ranges of the applied membership functions. Varying the shape, position and input-output range of these functions different control performance is achieved. The triangular membership functions and the singleton consequents are characterized by three parameters (i.e., p_{i1},p_{i2} and p_{i3} describe the points of the triangle fuzzy set) and an output gain (u_i of the ith controller), respectively. These parameters are selected to be tuned by means of numerical optimization in case of FLCs. On the other hand, the performance of the PID controller is influenced by the proportional (K_P), integral (K_I) and derivative (K_D) coefficients, therefore these coefficients represent the parameter set to be tuned in case of the linear control approach. The initial values of the controller parameters are given in the fourth column of Table 2.7.

Table 2.7: Notation of the FLC parameters: initial and optimized values.

FLC1

Fuzzy set	Meaning	Parameters	Initial values	Optimized values
N (in)	negative	$\Gamma(-\infty, -p_{11}, -p_{12})$	$p_{11} = 0.35$ and $p_{12} = 0$	$p_{11} = 0.289$ and $p_{12} = 0$
Z (in)	zero	$\Gamma(-(p_{11} - p_{13}), 0, (p_{11} - p_{13}))$	$p_{13} = 0$	$p_{13} = 0.0019$
P (in)	positive	$\Gamma(p_{12}, p_{11}, \infty)$	–	–
S (in)	small	$\Gamma(-\infty, 0, d_{11})$	$d_{11} = 0.5$	$d_{11} = 0.783$
L (in)	large	$\Gamma(d_{12}, d_{13}, \infty)$	$d_{12} = 0$ and $d_{13} = 0.5$	$d_{12} = 0.17$ and $d_{13} = 0.953$
N, P (U_P out)	neg. and pos. (out gains)	u_{11}	$\lvert u_{11}\rvert = 3$	$\lvert u_{11}\rvert = 1.002$
Nx, Px (U_P out)	neg. and pos. (out gains)	u_{12}	$\lvert u_{12}\rvert = 1$	$\lvert u_{12}\rvert = 0.22$
N, P (U_I out)	neg. and pos. (out gains)	u_{13}	$\lvert u_{13}\rvert = 1.5$	$\lvert u_{13}\rvert = 5.26$

FLC2

Fuzzy set	Meaning	Parameters	Initial values	Optimized values
N (in1)	negative	$\Gamma(-\infty, -p_{21}, -p_{22})$	$p_{21} = 15$ and $p_{22} = 0$	$p_{21} = 27.04$ and $p_{22} = 0$
Z (in1)	zero	$\Gamma(-(p_{21} - p_{23}), 0, (p_{21} - p_{23}))$	$p_{23} = 0$	$p_{23} = 1.122$
P (in1)	positive	$\Gamma(p_{22}, p_{21}, \infty)$	–	–
N (in2)	negative	$\Gamma(-\infty, -d_{21}, -d_{22})$	$d_{21} = 220$ and $d_{22} = 0$	$d_{21} = 657.93$ and $d_{22} = 0$
Z (in2)	zero	$\Gamma(-(d_{21} - d_{23}), 0, (d_{21} - d_{23}))$	$d_{23} = 0$	$d_{23} = 13.301$
P (in2)	positive	$\Gamma(d_{22}, d_{21}, \infty)$	–	–
N, P (out)	consequent gain	u_2	$\lvert u_2\rvert = 0.6$	$\lvert u_2\rvert = 1.068$

FLC3

Fuzzy set	Meaning	Parameters	Initial values	Optimized values
N (in)	negative	$\Gamma(-\infty, -p_{31}, -p_{32})$	$p_{31} = 30$ and $p_{32} = 0$	$p_{31} = 16.629$ and $p_{32} = 0$
Z (in)	zero	$\Gamma(-(p_{31} - p_{33}), 0, (p_{31} - p_{33}))$	$p_{33} = 0$	$p_{33} = 3.970$
P (in)	positive	$\Gamma(p_{32}, p_{31}, \infty)$	–	–
N, P (out)	consequent gain	u_3	$\lvert u_3\rvert = 1.5$	$\lvert u_3\rvert = 2.398$

PID1

Coefficient	Meaning	Range	Initial values	Optimized values
K_P	proportional	$[1, 24]$	$K_{P,1} = 12$	$K_{P,1} = 8.80$
K_I	integral	$[5, 35]$	$K_{I,1} = 25$	$K_{I,1} = 19.07$
K_D	derivative	$[-, -]$	$K_{D,1} = 0$	$K_{D,1} = 0$

PID2

Coefficient	Meaning	Range	Initial values	Optimized values
K_P	proportional	$[0.002, 0.1]$	$K_{P,2} = 0.03$	$K_{P,2} = 0.054$
K_I	integral	$[-, -]$	$K_{I,2} = 0$	$K_{I,2} = 0$
K_D	derivative	$[7 \cdot 10^{-8}, 5 \cdot 10^{-5}]$	$K_{D,2} = 3 \cdot 10^{-5}$	$K_{D,2} = 5.12 \cdot 10^{-7}$

2.3.3.2 Complex Fitness Function

The control performance is measured with the fitness (or cost) function. In the previous subsection different error integral formulas have been recommended for the quality measurement of both the reference tracking and suppression of IB oscillations. Based on these error integrals, a combination of four mean absolute errors (MAE) is chosen for the cost function to qualify the overall control performance. This cost function evaluates the quality of reference tracking (e_ν and e_ξ), the efficiency of IB oscillations suppression (e_{ω_3}) and the average current consumption (I_A). This formula makes optimization to tune the controller parameters such a way that both fast system dynamics and reduced IB oscillations and jerks in the mechanics are ensured. The selected complex fitness function is given as follows.

$$F = \sqrt[4]{\left(\frac{\sum_{j=1}^{N}|e_{\nu,j}|}{L}\right)^{\alpha_1}\left(\frac{\sum_{j=1}^{N}|e_{\xi,j}|}{L}\right)^{\alpha_2}\left(\frac{\sum_{j=1}^{N}|e_{\omega_3,j}|}{L}\right)^{\beta}\left(\frac{\sum_{j=1}^{N}\left|I_{A,j}^2\right|}{L}\right)^{\gamma}} \tag{2.39}$$

In equation (2.39) N denotes the length of the measurement, $j = 1...N$, while $\alpha_1 = 1.4$, $\alpha_2 = 0.85$, $\beta = 1.6$ and $\gamma = 0.4$ weights represent the preferences between the control objectives. Among these weights, α_1 and β are the largest, since the most important control quality goal is to achieve the desired planar motion as fast as possible and with least amount of IB oscillations. The evaluated yaw rate control quality (performance of FLC3) has less impact ($\alpha_2 = 0.85$) in equation (2.39), since it does not influence the relationship between the MWP's translational motion and resultant IB oscillations. Moreover, the squared average motor current is considered in the cost function to emphasize the effect of current peaks. The aim of the optimization problem is to find the control parameters (p_i, d_i and u_i for FLCs and $K_{P,i}$, $K_{I,i}$ and $K_{D,i}$ for PID controllers, see Table 2.7) that correspond to the minimum fitness function value.

2.3.3.3 Particle Swarm Optimization

The simulation environment was considered as a black box object; its inputs and outputs are the desired planar motion (ν_d and ξ_d) and reference tracking errors (e_ν, e_{ω_3}) plus average motor current I_A, respectively. Moreover, the simulation model is characterized by the controller parameters that determine the overall control performance. Fig. 2.15 depicts both the overall block diagram of the applied fuzzy and PID-based closed loop structures and their optimization procedure. The PSO is applied for the tuning of the control parameters, since it is a robust and efficient heuristic method that has already proven its fast convergence property Kecskés and Odry (2014); Ye *et al.* (2017). The fuzzy structure is characterized by 15 parameters, therefore $n_{gen} = 150$ and $n_{pop} = 150$ are chosen for the number of generations and populations, respectively. In case of the PID structure, the optimization is executed with $n_{gen} = 40$ and $n_{pop} = 40$, since only much less parameters characterize the controllers.

PSO utilizes individual particles that form a swarm, imitating the swarm behavior of flocking birds, to search for the global minimum or maximum within a search space. During the particles' flights, they adjust their positions based on both their own experiences and the experiences gained by the swarm as a whole. Specifically, each particle broadcasts its current optimum local points to its neighboring particles. Therefore, each particle knows not only its own optimal position but also the optimal positions of its neighbors as well as the optimal position achieved by the swarm as a whole (the current global optimum). These identified optimal positions are then used by the swarm as reference points for the search process in the iteration's next step Kennedy *et al.* (2001). Let X_i and V_i denote the position and velocity vector of the ith particle in the swarm, while P_i and G indicate the personal best position (which gives the best fitness value so far) of the ith particle and the global best position achieved (i.e., the position of the best individual), respectively. The velocity and position vectors are modified in every generation

based on the following equations:

$$V_i^{k+1} = \varpi V_i^k + c_1 r_1 \left(P_i^k - X_i^k\right) + c_2 r_2 \left(G^k - X_i^k\right),$$
$$X_i^{k+1} = X_i^k + V_i^{k+1}, \tag{2.40}$$

where c_1 and c_2 are positive constants, $r_1, r_2 \in [0, 1]$ are random values, and ϖ is the inertia weight. These parameters have been selected as $\varpi = 0.9$, $c_1 = 0.5$ and $c_2 = 1.5$ based on previous studies Kecskés and Odry (2014). In the present study, we used the Particle Swarm toolbox for MATLAB Code (2013) to implement the algorithm.

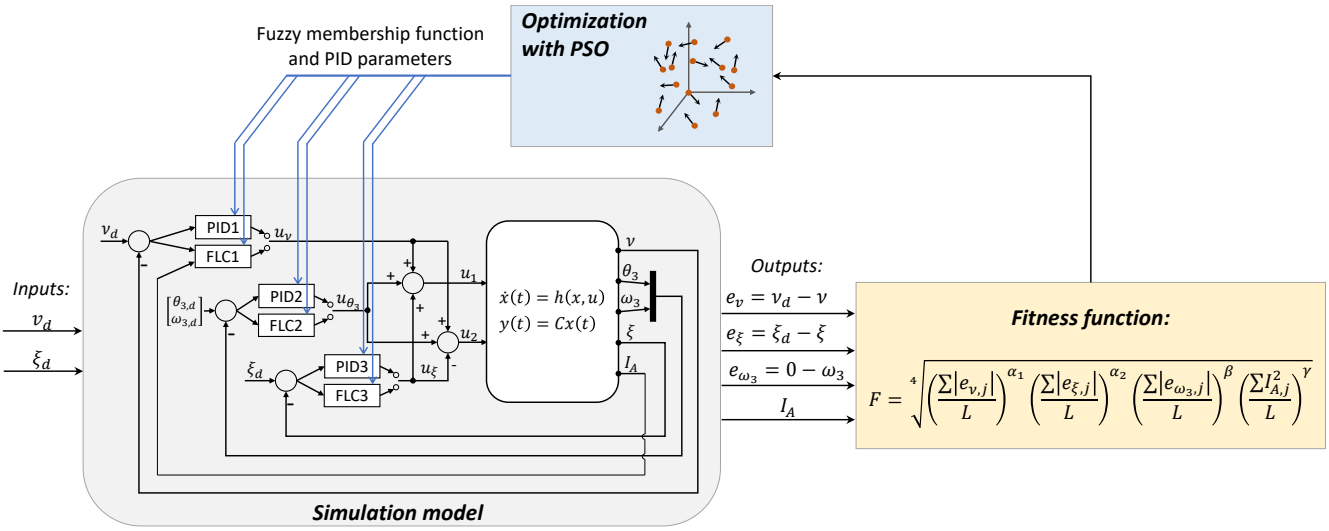

Figure 2.15: Block diagram of the closed loop and its optimization procedure.

2.3.4 Results

The original source is Odry and Fullér (2018).

The optimized closed loop behaviors are depicted in Figs. 2.16 and 2.17, while the tuned PID and FLC parameters are summarized in the fifth column of Table 2.7. The achievable maximum linear speed of the robot is approximately 0.5 ms^{-1}. In order to test the response time of the closed loop dynamics both fast and slow behaviors are analyzed. Therefore, the following reference (desired) signals are considered in the analysis: $\nu_d = \{0.4, 0, -0.2, 0\}$ ms^{-1} for the translational motion and $\xi_d = \{30, 0, -70, 0\}$ degs^{-1} for the desired yaw rate.

Regarding the optimized fuzzy control structure, the corresponding fitness function value (evaluating equation (2.39)) has significantly improved after the optimization procedure, namely, from $F_{\text{init}} = 0.1049$ (related to the initial controller parameters in the fourth column of Table 2.7) to $F_{\text{opt}} = 0.0558$, thereby providing 46.8% better overall control performance (the smaller the value the better control performance is achieved). Based on Fig. 2.16, it can be observed, that the optimized FLC parameters ensure fast closed loop behavior (the reference values are achieved in less than 0.7 sec), moreover the oscillation of the IB is limited and quickly suppressed (similarly, in less than 0.7 sec). Therefore, the optimization enabled to obtain a more efficient

control structure that has remarkably enhanced the system behavior (fast and effective reference tracking). Moreover, the electro-mechanical parts of the MWP are protected, since high peaks and jerks related to IB oscillations are limited. The flexibility of the FLCs allowed to significantly reduce the motor current peaks. The initial closed loop dynamics was characterized by $0.5-0.6$ A motor current transients. These transients are limited to $0.2-0.3$ A current peaks by employing the optimized FLCs, therefore with smaller current consumption and limited jerks and current peaks, the electro-mechanical parts of the MWP are more protected. Based on the partial fitness function results, it can be remarked that the reference tracking performance has been enhanced by 13% and 59% for the linear speed and yaw rate control, respectively, while the performance of the suppression of the IB oscillation has been enhanced by 36% with the optimized fuzzy control structure.

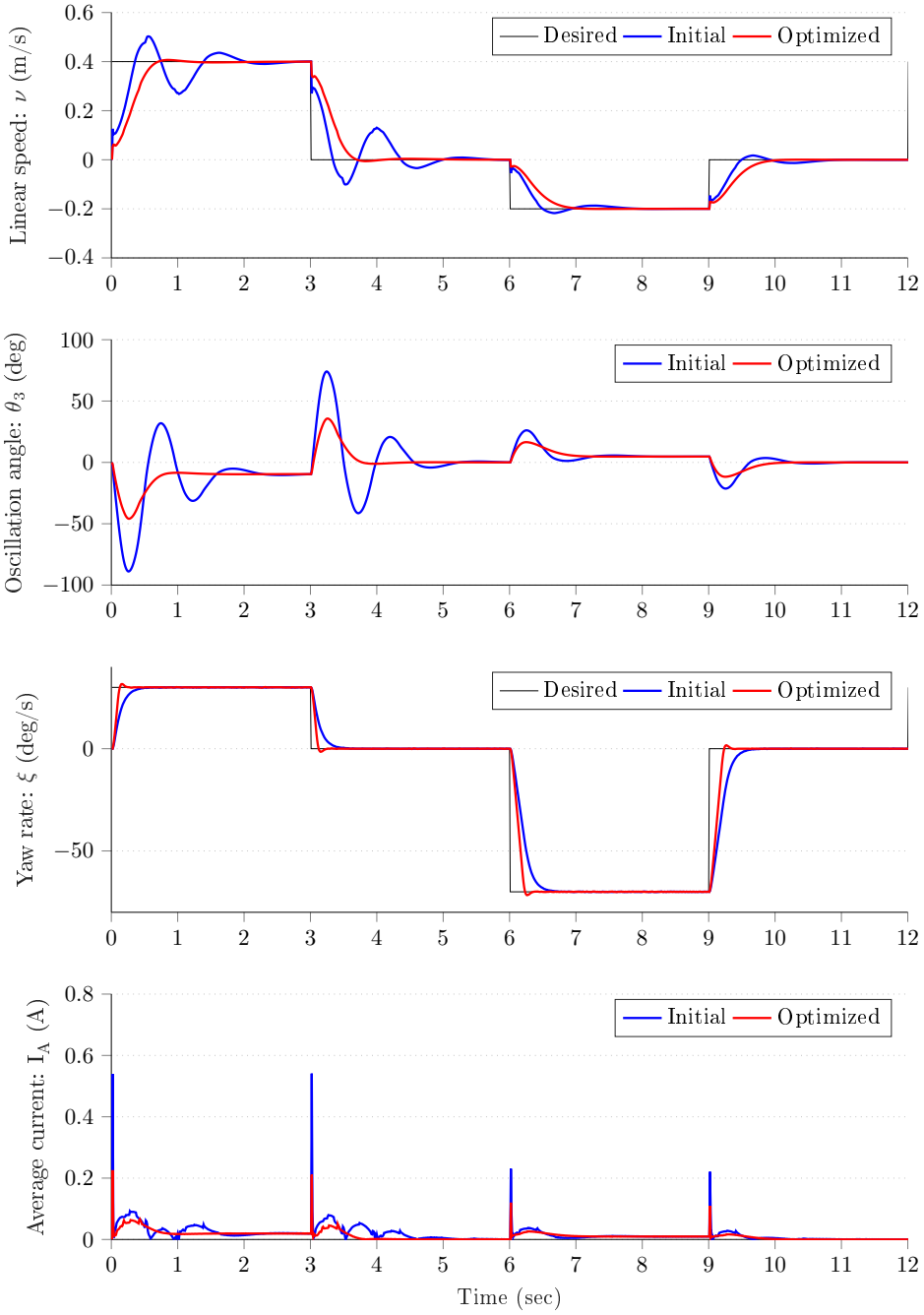

Figure 2.16: Closed loop dynamics of the fuzzy approach before (blue) and after (red) the optimization.

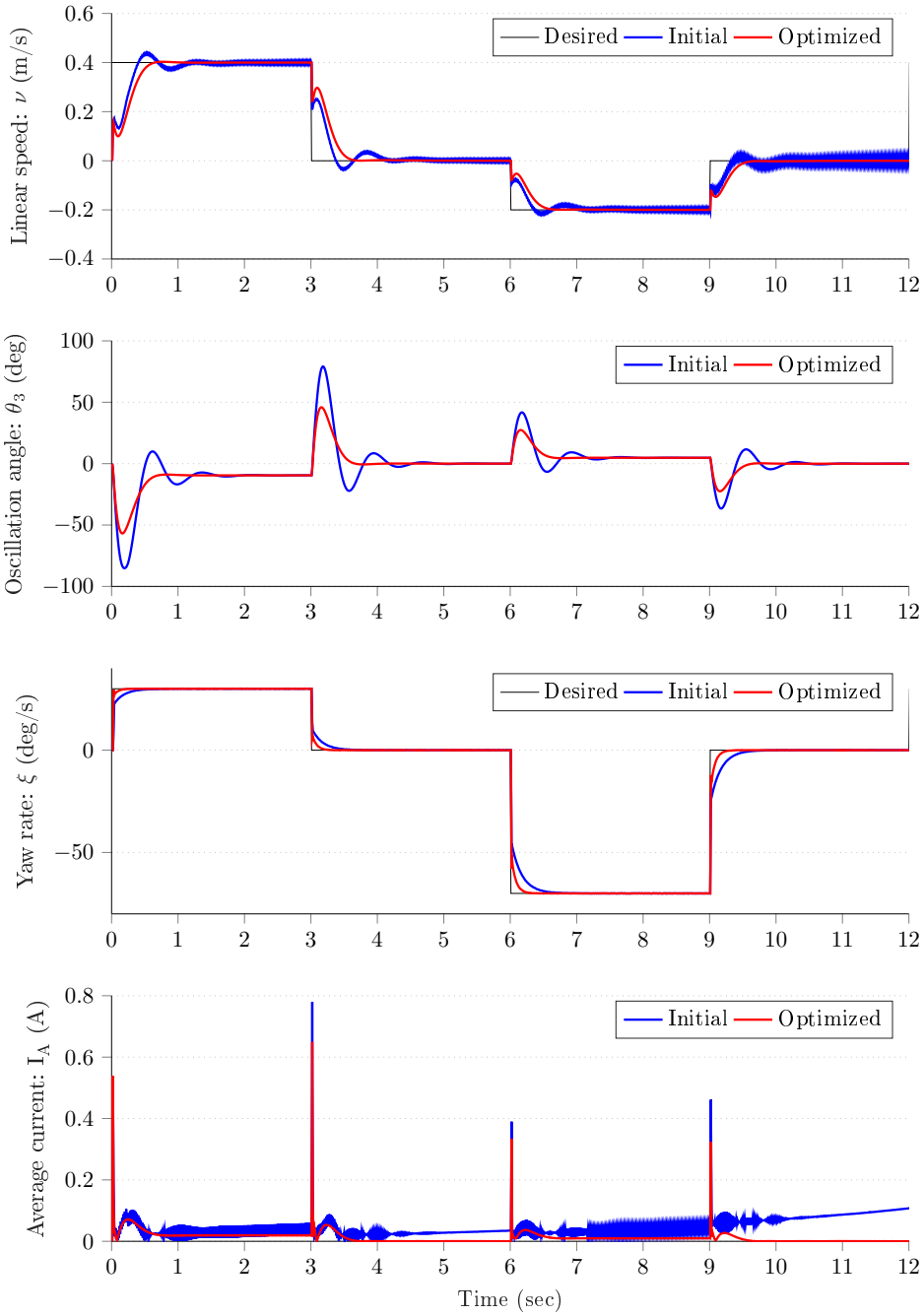

Figure 2.17: Closed loop dynamics of the linear approach before (blue) and after (red) the optimization.

The optimized control performances are highlighted and compared in Fig. 2.18, while the initial and optimized PID and fuzzy action surfaces are shown in Fig. 2.19 and Fig. 2.20, respectively. Based on the first row of Fig. 2.18 it can be observed that both the optimized fuzzy and optimized PID control schemes provide the same closed loop dynamics for the planar motion of the MWP (the desired linear speed is achieved in 0.68 sec). However, the flexibility of fuzzy logic allowed to perform the suppression of both the IB oscillations and current peaks much more effectively (significantly smaller IB oscillation and current peak compared to the optimized PID control results). Namely, the resultant IB oscillation is suppressed in 0.68 sec in both cases, however significant difference in the magnitudes can be observed (i.e., 56.8 deg

and 46.8 deg in case of PID and fuzzy control schemes, respectively). Moreover, the current consumption of the PID control is characterized with a 0.54 A average current peak, while the optimized fuzzy scheme accomplished the same task with a significantly smaller 0.32 A current peak. These results prove that the flexible nature of fuzzy logic could result in a more efficient overall control performance, where the IB oscillation is limited and quickly suppressed, moreover, the electro-mechanical parts of the MWP are more protected against jerks and high current peaks.

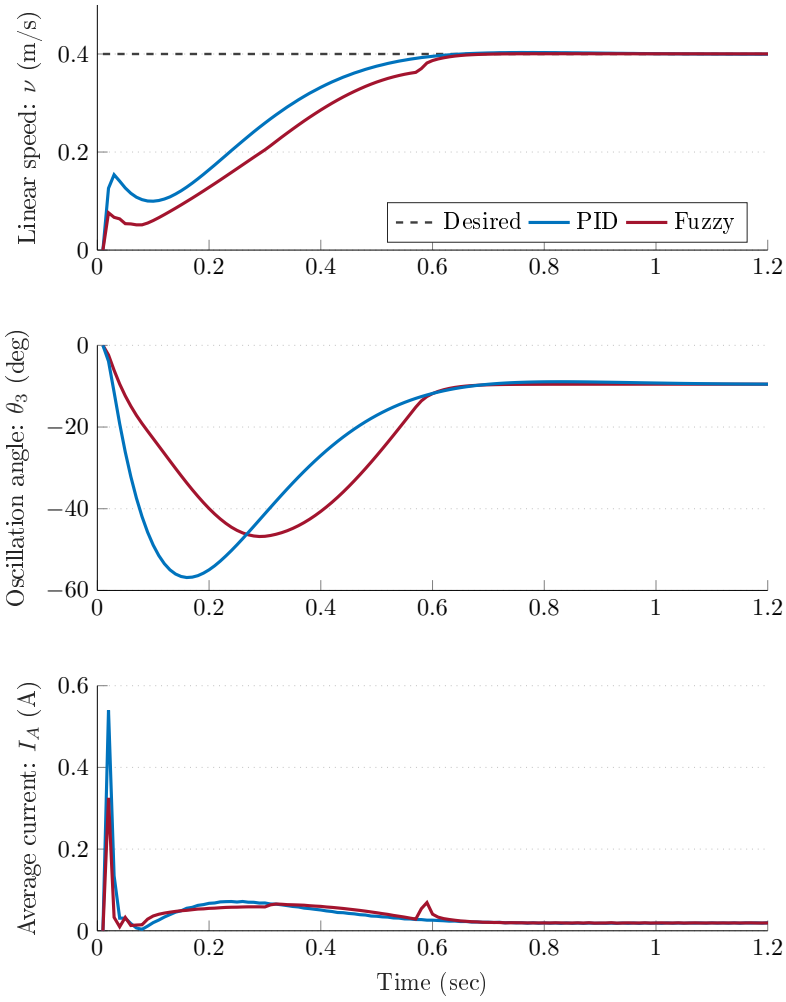

Figure 2.18: Control performances of optimized PID and fuzzy approaches.

The differences between the control performances can be explained based on the action surfaces depicted in Fig. 2.19 and Fig. 2.20. On one hand, the FLC1 establishes a nonlinear relationship between the speed error and the crisp output. Moreover, this relationship is extended with the impact of motor current, where the control action is nonlinearly decreased as the motor current increases. This nonlinear action surface results in that the planar motion of the MWP is characterized by slower system response in the first 0.5 sec in Fig. 2.18. However, as the average current magnitude has reduced the control action is increased, thereby the FLC could approach the initially faster PID controller around 0.6 sec.

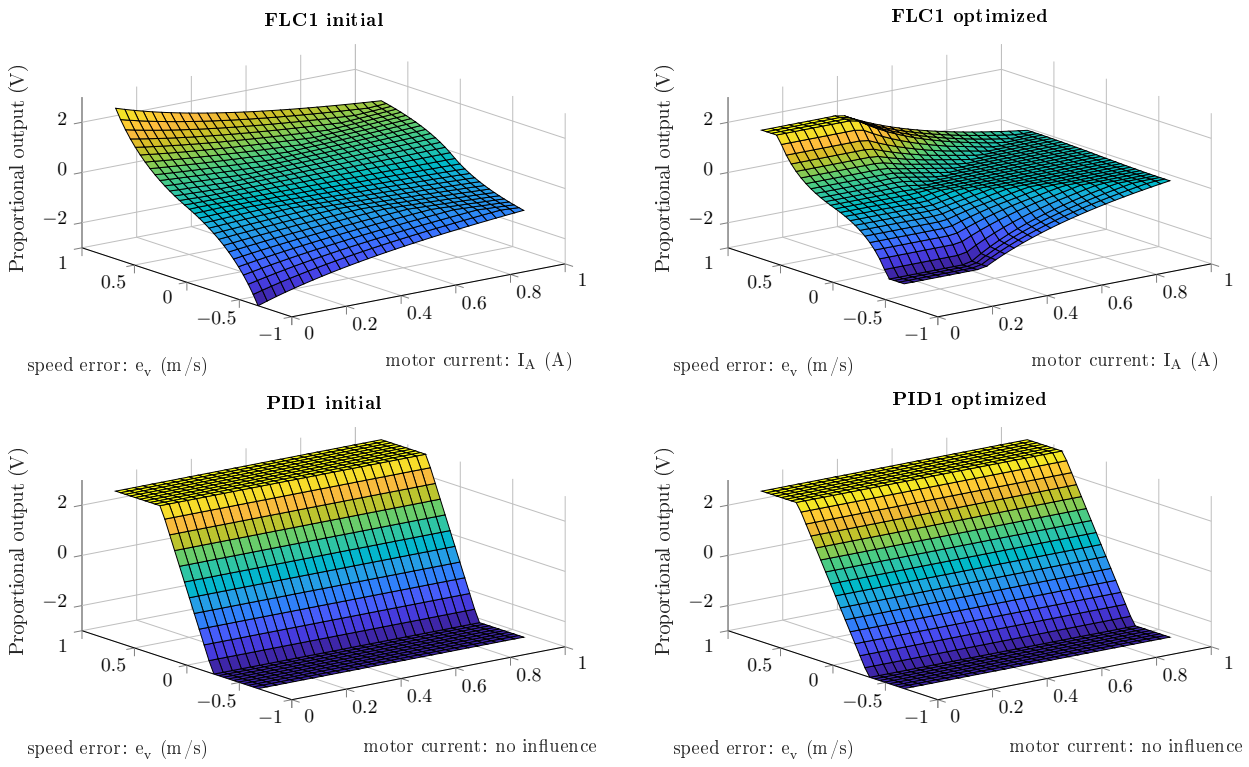

Figure 2.19: Action surfaces of FLC1 and PID1 before (left) and after (right) the optimization.

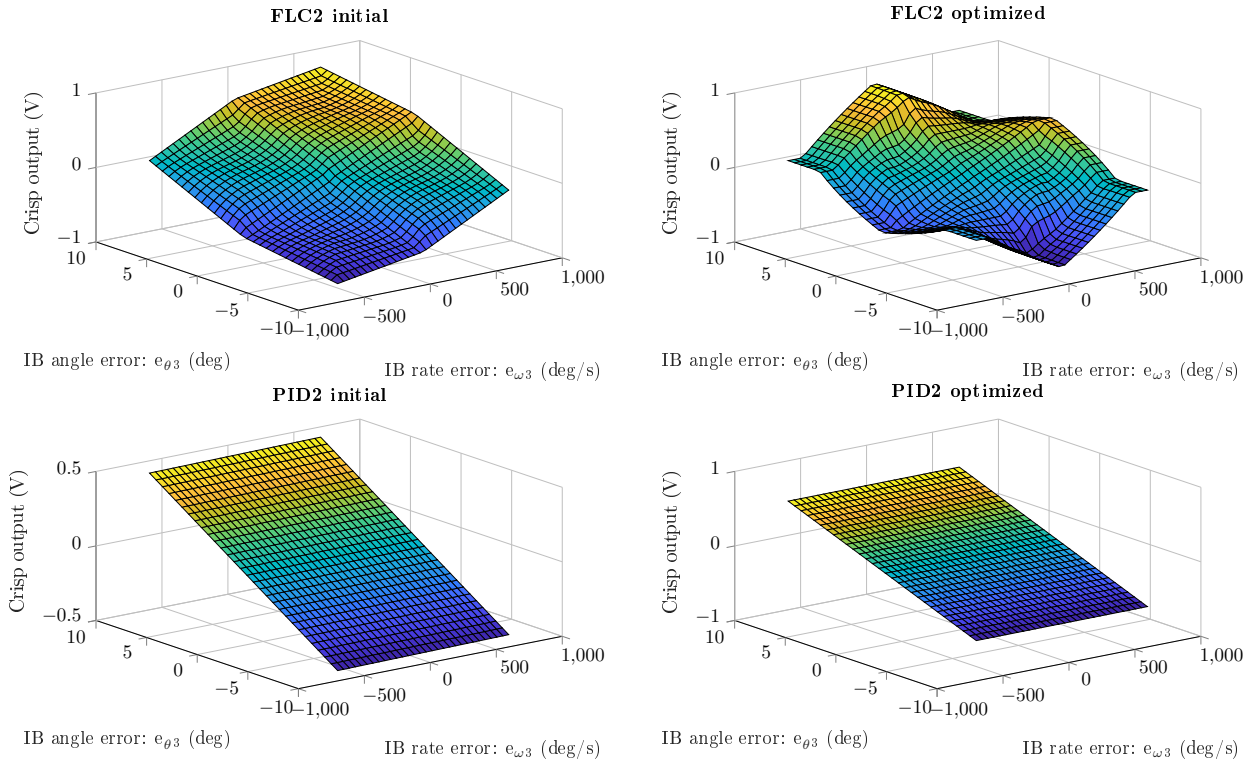

Figure 2.20: Action surfaces of FLC2 and PID2 before (left) and after (right) the optimization.

The action surfaces of the applied PID controllers show a linear connection between the input and output values. In the applied PID controller-based based scheme, it is not feasible to influence the control action such a way to limit the jerks and current peaks. This criteria could have been satisfied either with adaptive techniques or with an additional PID controller that is placed in the inner current loop. Both solutions would complicate the control structure. In contrast, the proposed (and later optimized) protective FLC has shown a well-applicable solution to both take into account additional inputs (such as the motor current) easily and provide efficient and robust control performance through the definition of simple heuristic IF-THEN rules.

The achieved control performances have shown that the flexibility of fuzzy logic provides an easy and effective way to improve the overall performance of the system. Moreover, the application of the PSO algorithm enables to tune heuristically defined control parameters, and thereby obtain maximized control quality. These results can be further improved with more sophisticated FLCs that are characterized by bigger rule bases and more linguistic values (e.g., the inputs and outputs of the FLCs could be decomposed into five membership functions in order to define finer and more advanced fuzzy inference machines). The investigation of more advanced FLCs is left open for future works.

2.4 Theses

This thesis group deals with the development and analysis of such fuzzy control approaches, which provide both robust dynamical behavior and energy efficient control actions in mechatronics (robotics) applications compared to conventional methods. The main result of the investigation is a special PI-type FLC structure, which limits the jerks and current transients in motor drive systems, thereby protecting efficiently the electro-mechanical parts of robots.

2.4.1 Thesis 1.1

A nonlinear 8-dimensional mathematical model of WMP systems has been derived that takes into account the motor dynamics, and its inputs are the terminal voltages of the applied motors. Based on the comparison of measurement and simulation results of open-loop robot dynamics, it was shown that the proposed model well describes the real behavior of the dynamical system, thus it provides the basis to effectively design control algorithms for these kind of underactuated naturally unstable mechatronic systems.

Publications pertaining to the thesis: Odry *et al.* (2015a,b).

2.4.2 Thesis 1.2

A cascade-connected, heuristic IF-THEN rules-based fuzzy control scheme has been developed for the unstable mechatronic system, which provides asymptotic stability in closed loop.

Publications pertaining to the thesis: Odry *et al.* (2016a, 2020a).

2.4.3 Thesis 1.3

A special PI-type FLC has been derived, which evaluates the instantaneous motor currents beside the error signals, thereby providing both smooth control action and improved control performance. A protective-type fuzzy control structure has been established with the derived FLC.

Publications pertaining to thesis: Odry *et al.* (2017b).

2.4.4 Thesis 1.4

An optimized fuzzy control structure has been obtained with the aid of the PSO algorithm. The outlined comparative analysis highlighted that the protective-type FLC structure provides significantly improved control performance than the linear approach in terms of the resulting oscillations and current peaks in the electro-mechanical structure of mechatronic systems.

Publications pertaining to thesis: Odry *et al.* (2016b, 2017a); Odry and Fullér (2018).

Remark: The byproduct of these theses is a novel educational project for both robotics and control system design laboratories. I both developed a laboratory setup (WMP kit) for education of (fuzzy-based) control problems and described a complete laboratory project from analysis of the solutions in the literature, over the description and elaboration of dedicated student tasks, to the assessment recommendations. This laboratory project is described in Odry *et al.* (2020a):

Odry, Á., Fullér, R., Rudas, I. J., and Odry, P. Fuzzy control of self-balancing robots: A control laboratory project. *Computer Applications in Engineering Education*, 2020, 1 – 24.

Moreover, all the information, including the computer aided design (CAD) models, MATLAB/Simulink files, MCU software, and LUT-based implementation of FLCs have been made publicly available in the supplementary online material Odry (2019b) to help other lab teams in designing similar experiments. This enables both the WMP lab kit and addressed control system design problems to be replicated in the laboratory of any institution. The complete project along with the software tools have been developed solely by the author of this PhD dissertation.

3 State Estimation

This chapter discusses two novel approaches to estimate accurately mobile robot attitudes based on the fusion of low-cost accelerometers and gyroscopes. The first part of the paper demonstrates the use of a special test bench that both enables simulations of various dynamic behaviors of wheeled robots and measures their real attitude angles along with the raw sensor data. These measurements are applied in a simulation environment and the optimization of KF parameters is outlined. Then, a novel adaptive KF structure is developed that modifies the noise covariance values according to the system dynamics. The instantaneous dynamics are characterized regarding the magnitudes of both the instantaneous vibration and the external acceleration. The developed adaptive solution measures these magnitudes and utilizes fuzzy-logic to modify the filter parameters in real time. The proposed filter performances are also benchmarked against other common methods to analyze both the flexibility and robustness of the approaches. Then, as the generalization of the developed adaptive KF, a novel fuzzy-adaptive extended KF (hereinafter FAEKF) for the real-time attitude estimation of agile mobile platforms equipped with magnetic, angular rate, and gravity (MARG) sensor arrays is designed. This filter structure employs both a quaternion-based EKF and an adaptive extension, in which measurement methods are used to calculate the magnitudes of system vibrations, external accelerations, and magnetic distortions. These magnitudes, as external disturbances, are incorporated into a sophisticated fuzzy inference machine, which executes fuzzy IF-THEN rules-based adaption laws to consistently modify the noise covariance matrices of the filter, thereby providing accurate and robust attitude results. Moreover, a six-degrees of freedom (6 DOF) test bench is designed for filter performance evaluation, which also executes various dynamic behaviors in the three-dimensional space and enables measurement of the true attitude angles (ground truth) along with the raw MARG sensor data. The tuning of filter parameters is performed with numerical optimization based on the collected measurements from the test environment. A comprehensive analysis highlights that the developed techniques significantly improve the attitude estimation quality. Moreover, the filter structures successfully reject the effects of both slow and fast external perturbations.

The developed test benches can also be utilized to tune and optimize other attitude filters. Moreover, the proposed optimized and adaptive solutions are universally applicable to any robotic application in which attitude estimation is required and dynamic effects (such as vibration, acceleration and magnetic disturbance) influence the filter performance significantly.

3.1 IMU-based Attitude Estimation

The original source is Odry *et al.* (2018): Odry, Á., Fullér, R., Rudas, I. J., and Odry, P. Kalman filter for mobile-robot attitude estimation: Novel optimized and adaptive solutions. *Mechanical systems and signal processing*, **110**, 569 – 589.

This section focuses primarily on one-dimensional attitude (tilt angle) estimation of WMP systems. As mentioned in the introduction (see subsection 1.1.4), neither the accelerometer

nor the gyroscope is capable of providing accurate and stable attitude values. Therefore, the purposes of attitude estimation are to integrate and process raw measurements and to provide attitude estimates that are smoothed properly. A KF is a recursive, state-space model-based algorithm that both enables the integration of the aforementioned sensors and provides the optimal state estimation based on the properly defined noise covariance matrices.

3.1.1 Algorithm

3.1.1.1 Gyroscope model

The raw gyroscope measurement Ω_k^B consists of three main components: the true angular velocity ω_k^B, the non-static bias term $\omega_{0,k}$, and the additive measurement noise μ_k. It is given by

$$\Omega_k^B = \omega_k^B + \omega_{0,k} + \mu_k, \tag{3.1}$$

where the superscript B denotes vectors expressed in the body frame and k is a discrete-time variable. In equation (3.1), the additive rate noise is assumed a zero-mean, white, Gaussian variable with the following characteristics:

$$E\left[\mu_k\right] = 0, \quad E\left[\mu_k \mu_l^T\right] = \sigma_\mu^2 \delta_{kl}, \quad \left[\sigma_\mu^2\right] = \left(\frac{\text{deg}}{\text{s}}\right)^2 \frac{1}{\text{Hz}}, \tag{3.2}$$

where σ_μ^2 denotes the noise variance and δ_{kl} is the Kronecker delta. Moreover, the term $\omega_{0,k}$ in equation (3.1) is considered a slowly varying bias (as a result of temperature sensitivity) modeled by the random walk process

$$\omega_{0,k} = \omega_{0,k-1} + \eta_k, \tag{3.3}$$

where η_k denotes driving Gaussian noise with a σ_η^2 noise variance, i.e.,

$$E\left[\eta_k\right] = 0, \quad E\left[\eta_k \eta_l^T\right] = \sigma_\eta^2 \delta_{kl}, \quad \left[\sigma_\eta^2\right] = \left(\frac{\text{deg}}{\text{s}}\right)^2 \text{Hz}. \tag{3.4}$$

After being reformulated from the gyroscope measurement (equation (3.1)), the true angular velocity, can be integrated numerically to compute the orientation using $\theta_{k+1} = \theta_k + \omega_k T_s$, where T_s is the sampling time. However, due to the bias term $\omega_{0,k}$ and the presence of the measurement noise μ_k, the gyro-based realization of θ_k produces an unbounded accumulation error. Therefore, gyroscope measurements yield only short-term accuracy (i.e., high-frequency attitude realization can be achieved with rate gyro measurements).

3.1.1.2 Accelerometer model

The raw accelerometer output A_k^B consists of four main components: the external acceleration α_k^B, the contribution of gravitational acceleration g_k^B, the bias term a_0, and the additive measurement noise ν_k, and it is given by

$$A_k^B = \left(\alpha_k^B - g_k^B\right) + a_0 + \nu_k. \tag{3.5}$$

The bias term is usually compensated for during the calibration procedure Höflinger *et al.* (2013), although the process for achieving this exceeds the scope of this article. If a robot (or another mobile mechatronic system) is in stationary state (i.e., no dynamic acceleration is occurring and $\alpha_k^B \approx 0$), then the gravity vector can be used to calculate the raw attitude realization $\theta_{A,k}$ with Li and Wang (2013)

$$\theta_{A,k} = \arctan2\left(A_{y,k}, A_{z,k}\right) = \theta_k + v_k, \tag{3.6}$$

where $A_{y,k}$ and $A_{z,k}$ are the instantaneous measurements of the accelerometer. This realization, which is described by equation (3.6), can also be considered the sum of the real attitude θ_k and additive noise v_k that represents the effects of ν_k from equation (3.5) after the trigonometric function has been evaluated. In a manner similar to the gyroscope model, v_k is assumed to be Gaussian white noise with the following characteristics:

$$E\left[v_k\right] = 0, \quad E\left[v_k v_l^T\right] = \sigma_v^2 \delta_{kl}, \quad \left[\sigma_v^2\right] = \deg^2 \frac{1}{\mathrm{Hz}}. \tag{3.7}$$

Based on equations (3.5) and (3.6), we can deduce that if there is an external acceleration ($\alpha_k^B \neq 0$), then the attitude realization given by equation (3.6) provides unreliable results and a drastically reduced accuracy because the ratio of $A_{y,k}$ to $A_{z,k}$ does not provide relevant attitude information (i.e., the pure gravity vector cannot be applied). In this implementation, the external acceleration is not modeled explicitly. Instead, its effects are absorbed by v_k (i.e., a significantly larger σ_v^2 noise variance is expected when $\alpha_k^B \neq 0$). Therefore, the accelerometer measurements yield adequate attitude realizations (so-called low-frequency attitude realizations) only when the system is in a non-accelerating mode.

3.1.1.3 Sensor fusion with Kalman filter

The previously described approaches can be synthesized to utilize the advantages of both types of sensors and to obtain attitude results with higher reliabilities and accuracies. In such a synthesis, the gyro-based attitude realization is extended by the attitude realization derived from the accelerometer data. Therefore, the unbounded integration error is compensated for and long-term stability is achieved. To fuse these sensors, a linear KF is implemented.

This KF is a recursive algorithm that provides an optimal estimation $\hat{x}$ of the noisy state vector x (whose dynamics are described by a state-space equation) such that:

$$\begin{aligned} &E\left[x_k - \hat{x_k}\right] = 0, \\ &E\left[\left(x_k - \hat{x_k}\right)\left(x_k - \hat{x_k}\right)^T\right] \rightarrow \inf. \end{aligned} \tag{3.8}$$

When MEMS IMU data are considered, the state dynamics are constructed from both the discrete-time integrated true angular velocity (ω_k reformulated from equation (3.1)) and the random walk process of the bias term (equation (3.3)). This means that the state propagation

is described by the state vector $x_k = (\theta_k, \omega_{0,k})^T$, the input variable $u_k = \Omega_k$, and the process noise vector $w_k = (\mu_k, \eta_k)^T$ as

$$\begin{aligned} x_{k+1} &= \Phi x_k + \Gamma u_k + w_k, \\ \begin{bmatrix} \theta \\ \omega_0 \end{bmatrix}_{k+1} &= \begin{bmatrix} 1 & -T_s \\ 0 & 1 \end{bmatrix} \begin{bmatrix} \theta \\ \omega_0 \end{bmatrix}_k + \begin{bmatrix} T_s \\ 0 \end{bmatrix} \Omega_k + \begin{bmatrix} \mu \\ \eta \end{bmatrix}_k, \end{aligned} \tag{3.9}$$

where Φ is the state transition matrix, Γ denotes the input matrix, and $T_s = 1/f_s$ is the sampling time. Based on equation (3.6), the measurement equation is formed (as an updated absolute orientation) with an output of $z_k = \theta_{A,k}$, measurement noise of v_k, and an output matrix of H as

$$\begin{aligned} z_k &= H x_k + v_k, \\ \theta_{A,k} &= \begin{bmatrix} 1 & 0 \end{bmatrix} \begin{bmatrix} \theta \\ \omega_0 \end{bmatrix}_k + v_k. \end{aligned} \tag{3.10}$$

According to the stochastic hypothesis, if the process and measurement noise vectors w_k and v_k are uncorrelated ($E\left[w_k v_l^T\right] = 0$) and modeled with zero-mean, white, Gaussian random variables (as was assumed in both the gyroscope and accelerometer models represented by equations (3.2), (3.4), and (3.7)), then the Kalman filter provides an optimal estimation with a minimum state-vector variance. The recursive algorithm uses the state-space equations (3.9) and (3.10) along with the covariance matrices of w_k and v_k given by $Q = E\left[w_k w k^T\right]$ and $R = E\left[v_k v k^T\right]$, respectively, to propagate the states, process the measurements, and update the covariance estimates in the time and measurement update equations Welch and Bishop (2001). Namely, the time update equations determine the *a priori* state estimate ($\hat{x}_k^-$) and estimate error covariance (P_k^-) as:

$$\begin{aligned} \hat{x}_k^- &= \Phi \hat{x}_{k-1} + \Gamma u_{k-1}, \\ P_k^- &= \Phi P_{k-1} \Phi^T + Q, \end{aligned} \tag{3.11}$$

where $\hat{x}_{k-1}$ and P_{k-1} denote the *a posteriori* (updated) state estimate and estimate error covariance at step $k-1$. The measurement update equations are responsible for correcting the *a priori* estimates employing both the measurement z_k and its noise covariance R. First, the Kalman gain is calculated:

$$G_k = P_k^- H^T \left(H P_k^- H^T + R\right)^{-1}, \tag{3.12}$$

then, both the state estimate and the estimate error covariance are updated (i.e., the *a posteriori* state vector and error covariance matrix are determined):

$$\begin{aligned} \hat{x}_k &= \hat{x}_k^- + G_k \left(z_k - H\hat{x}_k^- \right), \\ P_k &= \left(I - G_k H \right) P_k^-, \end{aligned} \tag{3.13}$$

where I denotes the 2×2 identity matrix.

Because the matrices Φ, Γ, and H in equations (3.9) and (3.10) contain constants, the estimation (or filter) performance is directly influenced, and thus determined, by the respective choices of the process and measurement noise covariances Q and R as well as the initial value of the estimation error covariance $P_0 = E\left[\left(x\left(0\right) - x_0 \right) \left(x\left(0\right) - x_0 \right)^T \right]$. The following subsections propose first a solution based on numerical optimization for automatic tuning of these parameters. Then, I develop an adaptive KF approach that varies the aforementioned covariance values based on the dynamical behavior of the system.

3.1.2 Test environment

To evaluate the state estimation error, measure the filter performance, and realize the optimization of the KF parameters, the true state (i.e., the true attitude of the WMP body θ_k) must be known. A test bench is designed, which provides a set of special circumstances to the WMP that allow the real attitude angle to be measured and the accelerometer and gyroscope measurements to be collected.

3.1.2.1 Electro-mechanical structure of the test bench

Due to the mechanical structures of WMP systems, the pendulum (the IB of the robot) is typically realized between the stators and the rotors of their applied motors. The relationships between the angular positions of the wheels ($\theta_{w,k}$) and the pendulum (θ_k) are given by

$$\theta_{r,k} = \theta_{w,k} - \theta_k, \tag{3.14}$$

where $\theta_{r,k}$ is the relative motor angle measured by the incremental encoders attached to the motor shafts. If the wheels are prevented from rotating (i.e., $\theta_{w,k} = 0$), then, based on equation (3.14), the rotary encoders can be used to measure the true angular position of the WMP body θ_k.

The test bench depicted in Fig. 3.1 takes advantage of this condition by using two (shaft-clamping) jaws to pin down the wheel shafts and prevent their rotation. The test bench jaws are attached to a movable plate that slides back and forth on two parallel 400-mm long rails via linear bearings. The position of the plate is measured by the attached encoder. This electro-mechanical structure enables external acceleration to occur simultaneously with the inner body's oscillation, allowing a variety of dynamic (vibrating and accelerating) system behavior to be simulated and measured. Fig. 3.1 shows both a photograph and the CAD model of the test environment. The shafts of the robot are fixed between the jaws. In the CAD model, the side- and top-printed WMP circuit boards are set to invisible to reveal the inner workings of the robot.

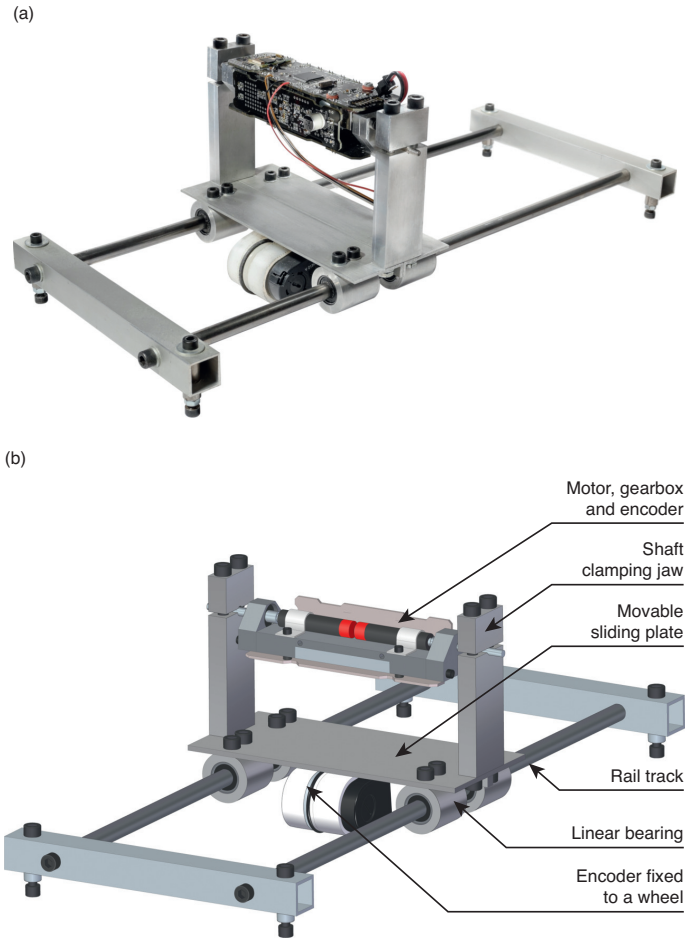

Figure 3.1: Photograph and CAD model of test bench.

The embedded WMP system has been described in section 1.3. Since the DC motors are equipped with both planetary gearheads of 64 reduction ratio and two-channel incremental encoders of 100 lines per revolution resolution. Therefore, the accuracy of true attitude (ground truth) measurements employing X4 encoding is:

$$\Delta_\theta = \frac{360^\circ}{4 \times 100 \times 64} \approx 0.0141^\circ. \tag{3.15}$$

During the measurement, the DC motors are driven using different sinusoidal signals (varying both amplitude and frequency), resulting in a wide variety of WMP body oscillations. Simultaneously, the movable plate is slid back and forth, simulating various horizontal acceleration values. The encoder measurements attached to the motor (the true attitude) and the sliding plate (the true horizontal acceleration), along with the instantaneous accelerometer and gyroscope data, are collected and sent to the PC for further evaluation. A three-channel incremental encoder (model no. HEDS-5540 A11) of 500 lines per revolution resolution is fixed to a wheel of $r = 19$-mm radius (see Fig. 3.1). Therefore, the accuracy of horizontal position measurement employing X4 encoding is:

$$\Delta_y = \frac{2\pi r}{4 \times 500} \approx 0.0597 \text{ mm}. \tag{3.16}$$

3.1.2.2 Measurement results

Dynamic behaviors, including stationary states, various angular velocities, mild and intense vibrations, and mild and intense acceleration have been measured and recorded. The measurement lasted for about 350 sec, and the simulated dynamic behavior has been characterized using the following ranges: $0-6.5$ Hz for body oscillation frequency, ± 800 degs^{-1} for angular velocity, and ± 1.5 g for external horizontal acceleration. Fig. 3.2 depicts two parts of the whole measurement in which the angle realization quality can be observed under both static and diverse dynamic conditions. The entire measurement data set can be accessed in the supplementary online material Odry (2019c).

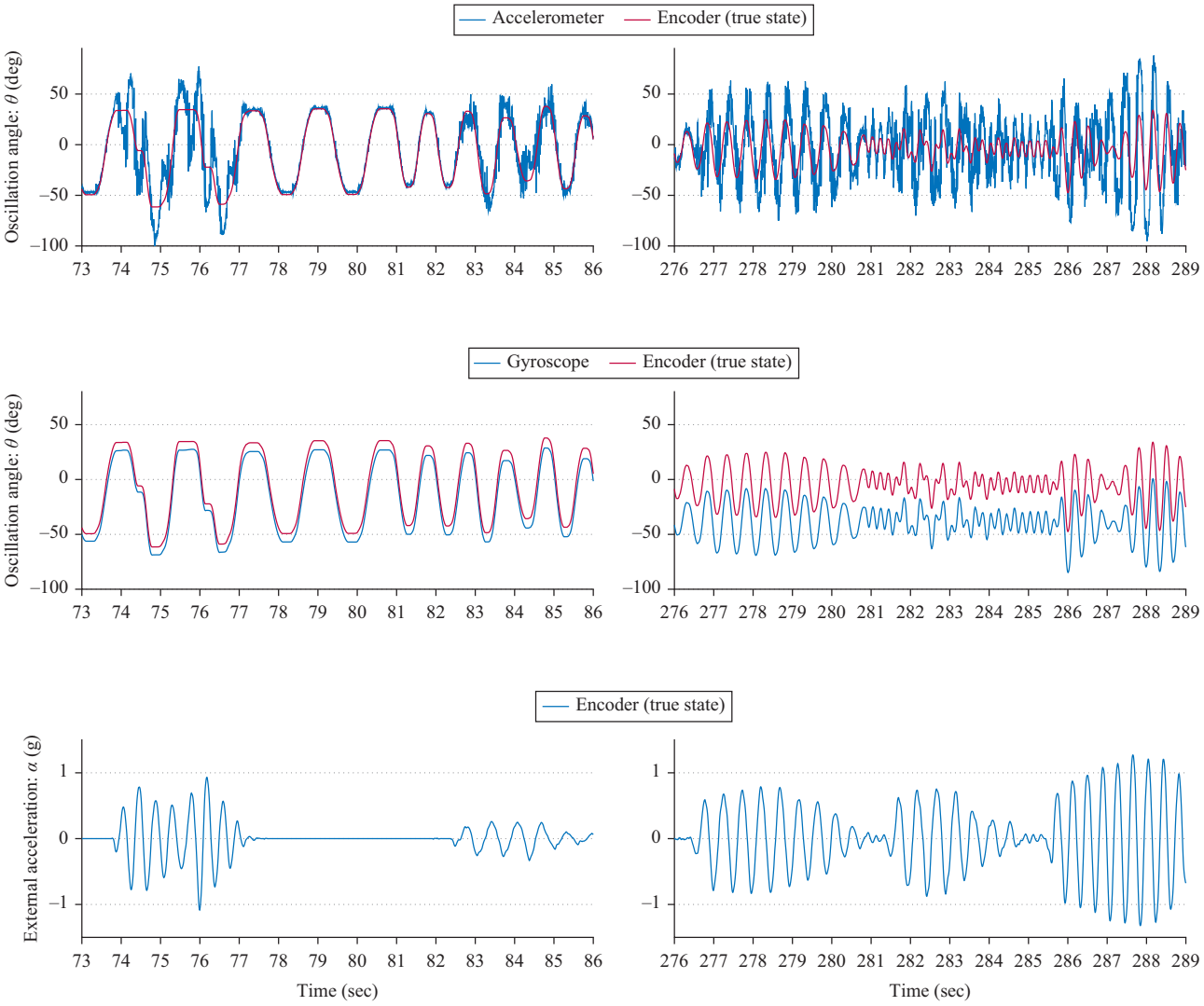

Figure 3.2: Two time slots from the 350 sec long measurement.

The first and second rows of Fig. 3.2 compare the real attitude (measured by the motor encoder) with the attitude realizations provided by the accelerometer and gyroscope data, while the third row shows the external acceleration (measured by the plate encoder) applied during the measurement process. On the one hand, due to the integration of the bias and noise components, the gyro-based angle realization is characterized by unbounded drift (e.g., the

accumulated error are about 15° after 100 sec and approximately 40° after 300 sec). On the other hand, for low-frequency oscillations with no external acceleration, the accelerometer-based realizations describe the instantaneous oscillations accurately (e.g., at around 80 sec). However, when either external acceleration or high angular velocity is present, the quality of the accelerometer-based realization decreases drastically (e.g., at around 75 sec and 85 sec). In fact, the instantaneous realizations are essentially useless in these cases (as shown on the entire right side of Fig. 3.2).

3.1.3 Optimization of filter parameters

Because the embedded WMP system is characterized by a low processing speed and the recorded measurements have been made available in MATLAB, the KF coefficient optimization is performed offline in a MATLAB/Simulink simulation environment. The block diagram of the measurement process and the applied optimization procedure is depicted in Fig. 3.3. The inputs of the simulation environment are the real angular position (i.e., the encoder measurement of θ_k) and the realized angular position and velocity values (i.e., $\theta_{A,k}$ and Ω_k calculated from the IMU measurements), while its output is the estimation error $e_k = \theta_k - \hat{\theta}_k$, where $\hat{\theta}_k$ denotes the output of the implemented KF algorithm. The KF parameter tuning is performed by defining a fitness function quantifying the estimation quality and applying a method for optimizing the noise covariance values by minimizing the fitness function value.

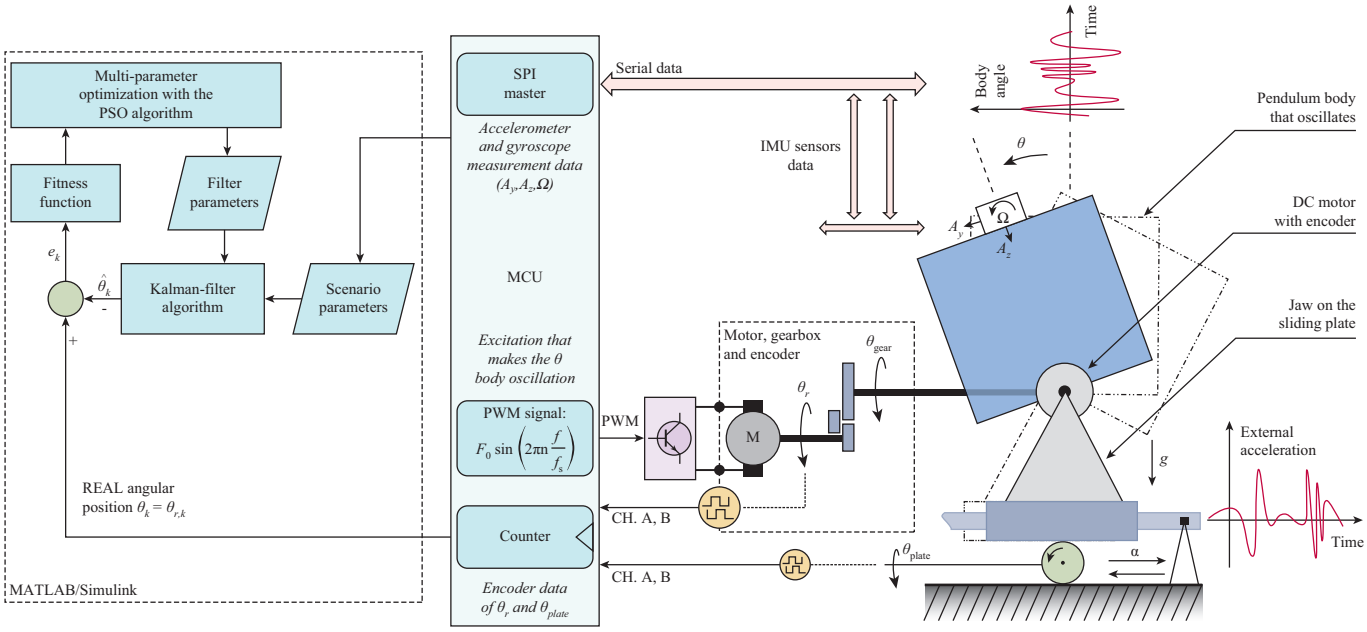

Figure 3.3: Block diagram of measurement and optimization procedures.

3.1.3.1 Initialization of filter parameters

The initial KF parameter values need to be defined in the simulation environment. Such initialization is necessary for the respective process and measurement noise covariance matrices Q and R, the state vector of the state equations (3.9) and (3.10) $\hat{x}_0$, and the estimation error covariance matrix P_0.

The process noise values μ_k and η_k in equation (3.9) are considered to be statistically independent (i.e., uncorrelated), as it is usually assumed Kownacki (2011); Lee *et al.* (2012); Gośliński *et al.* (2015); Crassidis *et al.* (2007). Therefore, a diagonal process noise covariance matrix (Q), along with the measurement noise variance value (R), is investigated in the optimization procedure, specified as:

$$Q = \begin{bmatrix} q_{00} & 0 \\ 0 & q_{11} \end{bmatrix}, \quad R = \rho, \tag{3.17}$$

where q_{00}, q_{11}, and ρ are introduced to provide simpler notation for the optimization. The noise variance initialization is typically determined via Allan variance analysis for a stationary system state Höflinger *et al.* (2013); El-Sheimy *et al.* (2008); Benini *et al.* (2015). However, if the system is operating in dynamic mode, then the Allan variance initialization method loses validity, especially with respect to ρ, which absorbs and represents the effects of external acceleration (equation (3.6)) as well as the sensor noise.

One advantage of the optimization process is that the noise analyses can be omitted, since rational initial guesses for q_{00}, q_{11}, and ρ will cause these parameters to converge to the optimal possible noise variances in the parameter space. Therefore, the following values have been chosen for the initialization of noise variances: $q_{00} = 5 \cdot 10^{-7}$, $q_{11} = 5 \cdot 10^{-9}$, and $\rho = 10^5 \cdot q_{00} = 0.05$, where the multiplication factor 10^5 indicates that the realizations of the accelerometer-based attitudes ($\theta_{A,k}$) are expected to be significantly more unreliable than gyro-based angular velocity realizations (Ω_k) due to the system's dynamic behavior.

When the measurements begins, the WMP body angle is 0°. Therefore, the initial state vector has been chosen as $\hat{x}_0 = (0, 0)^T$, while the initial value of state covariance matrix has been set to $P_0 = 0_{2\times 2}$. The estimation error covariance is updated continuously in KF algorithms, thus the initial P_0 guess affects the overall KF performance only slightly. Considering this, the elements of P_0 are not optimized.

3.1.3.2 Fitness function

The KF performance is measured by a fitness function that quantifies the differences between the real and estimated state values.

In most practice-oriented complex problems, the mean absolute error (MAE) or the mean squared error (MSE) are chosen as the fitness function in the model parameter optimization procedure. On one hand, because these formulas can be easily implemented and evaluated (even in embedded systems) and are well-suited to measurement uncertainties, many research results in the literature prove that successful parameter optimization is achieved based on the minimization of the MAE Modares *et al.* (2010b); Oh *et al.* (2011) or MSE Chatterjee *et al.* (2005); Alıcı *et al.* (2006); Kwok *et al.* (2006); Modares *et al.* (2010a); Quaranta *et al.* (2010); Alireza (2011); Alfi and Fateh (2011) fitness function. On the other hand, the model parameter optimization (or identification) in practical applications can be considered as a curve fitting problem as well. In this case, comparison of measurements and simulation results of a derived mathematical model and minimization of the MSE allow the unknown model parameters to be successfully identified.

Based on the foregoing facts, the mean square error was selected to be the fitness function:

$$F = \frac{1}{N}\sum_{k=1}^{N} e_k^2 = \frac{1}{N}\sum_{k=1}^{N}\left(\theta_k - \hat{\theta}_k\right)^2, \tag{3.18}$$

where N is the measurement length. The objective of the optimization problem is to determine the optimal possible ρ, q_{00}, and q_{11} noise variances corresponding to the lowest possible fitness function value.

Since the measurement errors in equations (3.9) and (3.10) are assumed to be independent, normally distributed random variables, therefore the optimization of the noise variances by minimizing F in equation (3.18) will correspond to the so-called maximum likelihood estimate Hendrix and Boglárka (2010).

3.1.3.3 Particle swarm optimization

During optimization, the simulation environment is considered a black box with inputs (measurements from both the encoder and the IMU), an output (the estimation error $e_k = \theta_k - \hat{\theta}_k$), and a set of parameters (in this case ρ, q_{00}, and q_{11}) that determine the filter performance. Therefore, similarly to the control system optimization problem (discussed in chapter 2), a heuristic optimization method has been chosen that is effective (with a fast convergence), easy to implement, robust, and able to operate without gradient information.

Among the heuristic optimization algorithms, the PSO is selected as the most suitable for this problem, because it has demonstrated greater effectiveness than genetic algorithms and other heuristic methods Kecskés *et al.* (2017b); Kwok *et al.* (2006); Kecskés and Odry (2014); Ye *et al.* (2017). In addition, PSO is a population-based search algorithm that uses the fitness function to guide the search in the search space; therefore, unlike gradient-based optimization methods, the PSO does not have difficulties with nonlinear, noisy, or discontinuous functions and is less susceptible to becoming trapped in local minima. These advantages are discussed in detail in Oh *et al.* (2011), while both the algorithm and its parameters have been described in subsection 2.3.3.3.

3.1.3.4 Results

Once the noise variance ranges are defined and the corresponding fitness function is formulated (equation (3.18)), the optimization algorithm can begin running. I have chosen $n_{gen} = 30$ and $n_{pop} = 30$ for the numbers of generations and populations, respectively, because the optimization problem itself is characterized by only three parameters (i.e., ρ, q_{00}, and q_{11}). The ranges of the parameters are defined heuristically. The algorithm has been run twice in succession, and its ranges and initial values have been redefined based on the subresults of the first iteration. The third column of Table 3.1 summarizes the results of the parameter optimization process, which are discussed in the rest of this subsection.

The optimization process uses the initial values defined in the previous subsection. An intense external acceleration has been applied during the measurement of the dynamic behavior, and its effect have been absorbed in the measurement noise v_k (equation (3.6)). Therefore, the noise variance ρ is expected to converge to a higher value. Indeed, the optimization has

converged to a noticeably higher variance value (up from 0.05 to 0.35) that more thoroughly represents the noise characteristics of the accelerometer-based realizations. At the same time, the process noise variances have converged to notably smaller values (from $5 \cdot 10^{-7}$ to $6.38 \cdot 10^{-8}$ for q_{00} and from $5 \cdot 10^{-9}$ to $3.08 \cdot 10^{-12}$ for q_{11}), meaning that the optimization has converged such that the noisy state propagation equation (3.9) has become much more reliable but the measurement update equation more uncertain. Owing to the lower process noise covariance Q, the filter gain has decreased. Therefore, the optimization has resulted in a KF characterized by dynamics slower than those of the algorithm using the initial values. Because the dynamic behavior I have simulated and measured on the test bench has covered both static and extreme (vibrating and accelerating) WMP conditions, the faster KF dynamics is not expected to be necessary. Considering the above, the optimization has provided satisfactory results. If the filter dynamics are too slow for certain applications, then the subresults of an earlier optimization run can be applied.

Table 3.1: Initial and optimized values with optimization bounds.

First run: $F_{init} = 8.6921 \rightarrow F_{opt} = 2.3447$

Symbol	Initial	Optimized	min	max
ρ	0.05	0.27905	0.008	0.3
q_{00}	$5 \cdot 10^{-7}$	$1.08 \cdot 10^{-7}$	$1 \cdot 10^{-7}$	$2 \cdot 10^{-6}$
q_{11}	$5 \cdot 10^{-9}$	$1.17 \cdot 10^{-10}$	$1 \cdot 10^{-10}$	$2 \cdot 10^{-8}$

Second run: $F_{init} = 2.3252 \rightarrow F_{opt} = 1.9077$

Symbol	Initial	**Optimized**	min	max
ρ	0.27	**0.35459**	0.25	0.45
q_{00}	$1 \cdot 10^{-7}$	$\mathbf{6.38 \cdot 10^{-8}}$	$7 \cdot 10^{-9}$	$7 \cdot 10^{-7}$
q_{11}	$1 \cdot 10^{-10}$	$\mathbf{3.08 \cdot 10^{-12}}$	$1 \cdot 10^{-12}$	$4 \cdot 10^{-10}$

Fig. 3.4 depicts the results of the parameter optimization process. In the first rows, the estimation performances are shown both before (by the red curves) and after (by the yellow curves) the optimization, and the estimated values are compared to the true attitudes. In the second rows, the estimation errors of the initial (blue curves) and optimized (red curves) KF are highlighted. A noticeable performance improvement can be observed in the plots. The curves for the optimized parameters fit both frequencies and amplitudes of the true body attitudes to a satisfactory degree. The fitness function value is significantly improved by the parameter optimization. Specifically, it decreased from the initial $F_{init} = 8.6921$ (filter performance achieved with the initial filter parameters) to $F_{opt} = 1.9077$, indicating that a 78% filter performance improvement has been achieved with the proposed optimization procedure.

The effects of the external acceleration and vibration still decreases the estimation quality drastically (e.g., around 75 sec on the left side and the whole right side of Fig. 3.4) resulting in an unsatisfactory initial KF performance (red curves, before optimization). However, a combination of optimized filter parameters has been found that enables the KF to effectively suppress the effects of these external disturbances, and to provide both satisfactory estimation accuracy and fast filter convergence for the intended application.

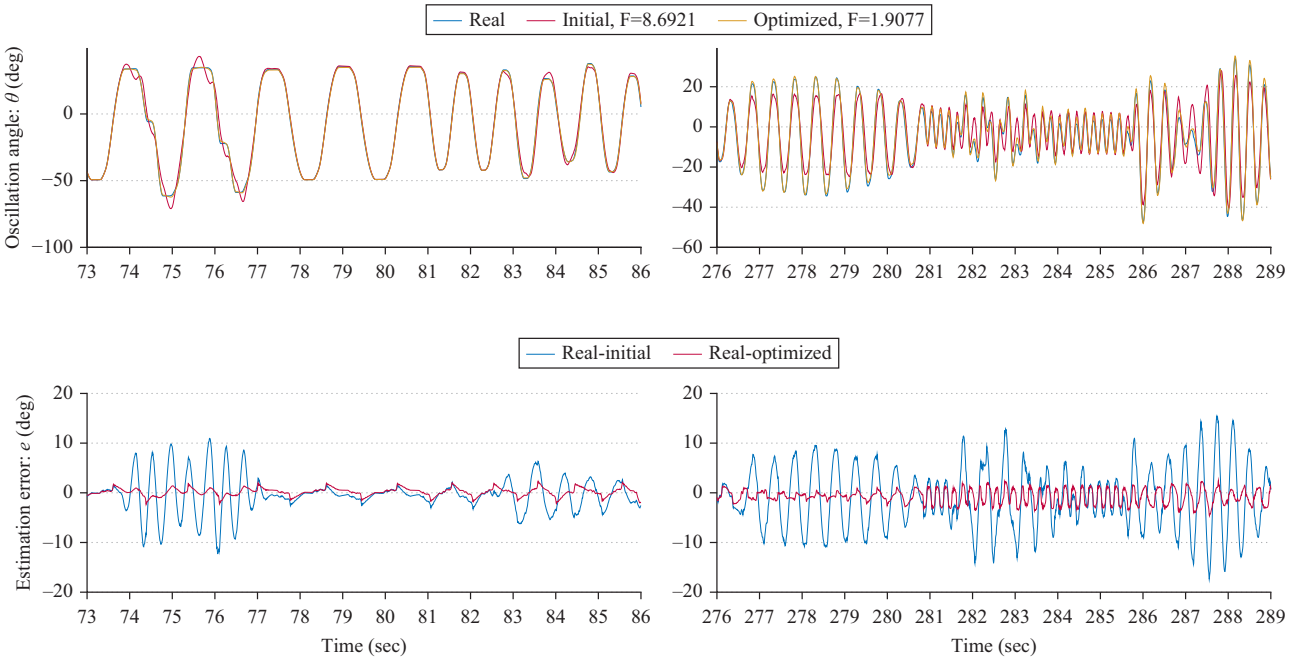

Figure 3.4: Initial and optimized Kalman filter performances compared to true body attitudes.

3.1.4 Adaptive Kalman filter approach

The previous subsection demonstrated that, with the assistance of optimization, a combination of noise covariance values Q and R can be found such that the resulting state estimation performance is satisfactory. However, the optimized Q and R matrices do not characterize accurately the real noise existing in the system but rather represent broad variance values that cover the whole noise and the model approximations in the measurement whether the system is stationary or subject to intense external disturbances. In the present study, this outcome is expected because the state-space equation does not model the external acceleration. Instead, the effects of the external disturbances are absorbed in the assumed white noise component of equation (3.10).

Because the KF performance is primarily influenced by the noise covariance values Q and R, I investigate in this subsection whether an adaptive approach that varies these matrices according to the instantaneous dynamical behavior can provide a performance superior to that of the filter convergence in the previous subsection or not. The instantaneous dynamical behavior is characterized by two factors: the magnitudes of the vibration and the external acceleration. If these factors are described by relevant measures in real time, then online manipulation of the noise covariance values can be realized and the estimation performance can be enhanced.

In the following subsections, I develop an adaptive KF approach that both measures the aforementioned external disturbances and modifies the noise variance assumed in the measurement model via a fuzzy inference machine. The results will demonstrate that the developed approach further improves the state estimation quality.

3.1.4.1 Measuring vibration magnitude

The magnitudes of instantaneous system vibrations can be described by the oscillation frequency of the WMP body. Among the two MEMS sensors, the gyroscope provides reliable measurements of the angular velocity for both low and high oscillations. Therefore, the gyroscope data can be utilized to estimate the instantaneous oscillation frequency.

Using this approach, the WMP body oscillation frequency is estimated with a fast Fourier transform (FFT)-based evaluation of short gyro measurement packets. The high sampling frequency of the sensor enables to gather measurement packets of length L. Through the FFT algorithm's evaluation of these short measurements, an estimation of the oscillation frequency ($\hat{f}$) is made. The main steps of the estimation algorithm is summarized as follows.

1. Collect a data packet x of length L from the gyroscope measurements. The value of L depends on the application requirements, since it is a trade-off between the amount of information used in the FFT calculation and the estimation delay. Larger L values provide finer oscillation spectra but longer estimation delays ($d = L/f_s$). In this study, the sampling frequency is 800 Hz and the window size is set to $L = 400$ ($d = 0.5$ sec delay).

2. Compute a discrete Fourier transform of the data packet x to obtain frequency domain information about the instantaneous oscillation. The output of the FFT algorithm is represented by the ordered pair $(f_i, |\Omega|_i)$, with f_i and $|\Omega|_i$ representing the frequency components and their corresponding amplitudes, respectively. Namely,

$$\mathcal{W}_l = \sum_{k=0}^{L_{\text{FFT}}-1} x_k e^{-j\left(\frac{2\pi lk}{L_{\text{FFT}}}\right)}, \quad l = 0, ..., L_{\text{FFT}} - 1 \tag{3.19}$$

and

$$(f_i, |\Omega|_i) = \left(\frac{f_s i}{L_{\text{FFT}}}, \frac{2}{L}\left|\mathcal{W}_i\right|\right), \quad i = 0, ..., \frac{L_{\text{FFT}}}{2}, \tag{3.20}$$

where L_{FFT} denotes the length of the transform. I set $L_{\text{FFT}} = 2^9$, yielding an estimation resolution of $\frac{f_s}{L_{\text{FFT}}} = 1.5625$ Hz.

3. Estimate the oscillation frequency (expected to be below $f_{\text{thr}} = 8$ Hz in the case of WMP) by finding the highest-intensity frequency component that is smaller than f_{thr} with

$$\begin{aligned} f_{\max} : (f_{\max}, |\Omega|_{\max}) \wedge |\Omega|_{\max} &= \max_{\forall i, f_i \leq f_{\text{thr}}} |\Omega|_i \,, \\ \hat{f} &= \begin{cases} 0, & \text{if } |\Omega|_{\max} < |\Omega|_{\text{thr}} \\ f_{\max}, & \text{otherwise} \end{cases} \end{aligned} \tag{3.21}$$

where, along with the conditions $f \leq f_{\text{thr}}$ and $|\Omega|_{\max} < |\Omega|_{\text{thr}}$, the frequency components related to the measurement noise are isolated (the high frequency components with small magnitudes). In the implementation of the algorithm, I set $|\Omega|_{\text{thr}} = 10$ degs^{-1}.

4. Repeat the steps starting from 1.

Fig. 3.5 demonstrates the results of using the aforementioned algorithm on four different data packets. In the first rows, the collected oscillations are shown in the time domain, while the second rows depict the corresponding FFT algorithm results. Evaluation of the algorithm's third step (equation (3.21)) results in the oscillation frequency estimate ($\hat{f}$) depicted near the peak of the curves. The embedded necessary condition in equation (3.21) is explained for the fourth case (on the right side) of Fig. 3.5 in which no oscillation occurs and the FFT result contains only the corresponding noise spectrum. When f_{thr} is not introduced, the 106-Hz frequency component would correspond to the maximum intensity and result in an incorrect estimate, while the introduction of $|\Omega|_{\text{thr}}$ prevents the incorrect selection of the 3-Hz component as the estimated frequency as well. Fig. 3.6 highlights the real-time algorithm evaluation over a section of the 350 sec measurement. The blue curve represents gyro-based angular rate measurements and the red curve shows the estimation of the oscillation frequency based on data packets of length $L = 400$. The figure illustrates that the aforementioned FFT-based algorithm provides information related to the instantaneous vibrations of a dynamical system.

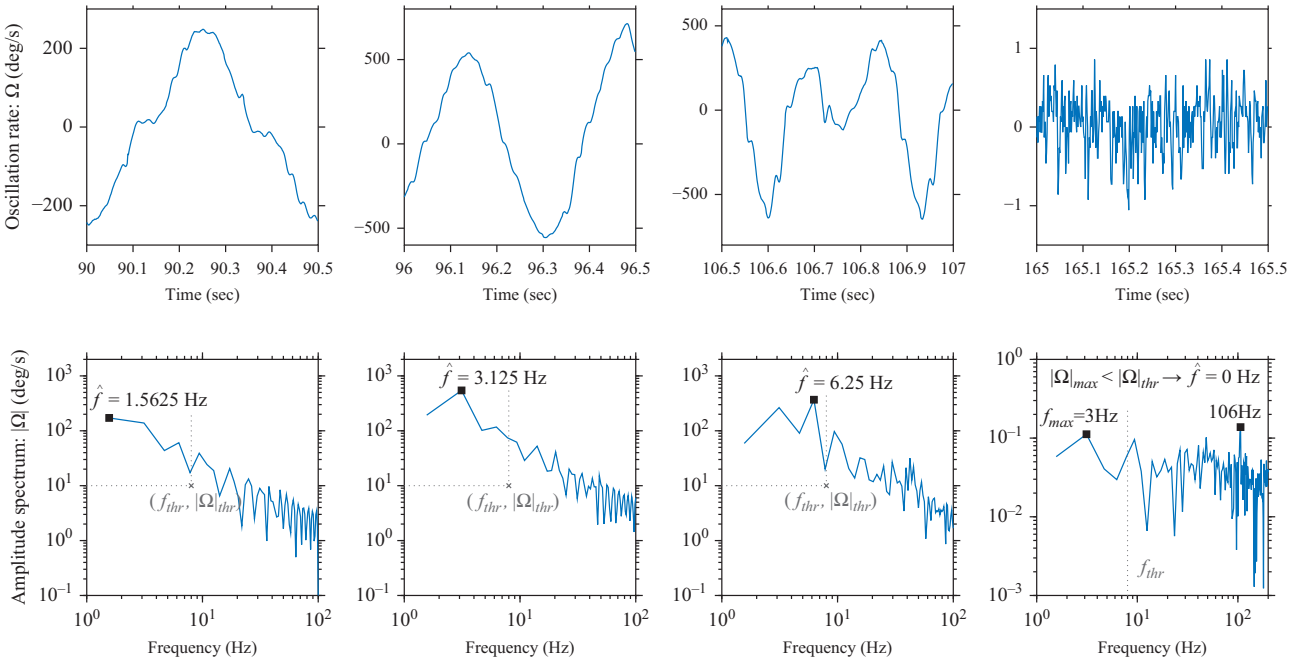

Figure 3.5: Demonstration of the use of a FFT-based frequency estimation algorithm on four different data packets.

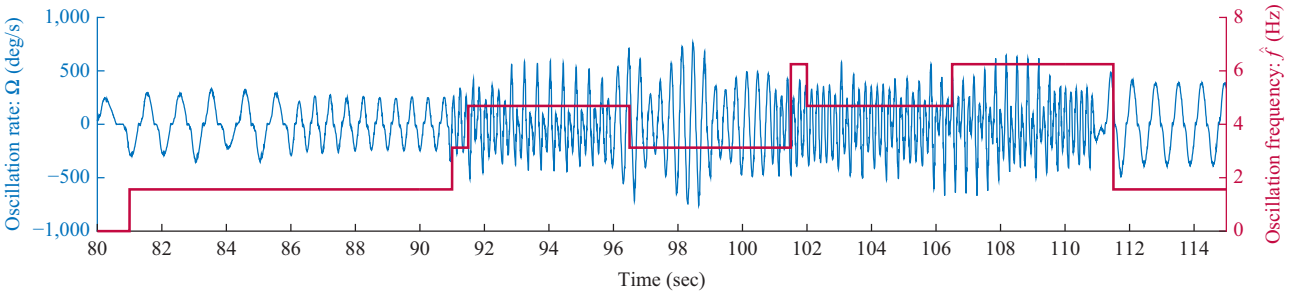

Figure 3.6: Real-time FFT-based oscillation frequency estimation.

3.1.4.2 Measuring external acceleration magnitude

The magnitude of the external acceleration can be derived from the accelerometer measurements. If the magnitude of the accelerometer measurement is approximately equal to the gravitational acceleration (i.e., $\sqrt{A_x^2 + A_y^2 + A_z^2} \approx 1\text{g}$), then the system is in a non-accelerating mode. Therefore, it is common practice to measure the external acceleration using a switching model in which different threshold levels are assigned to the dynamic acceleration $\alpha = \left|\sqrt{A_x^2 + A_y^2 + A_z^2} - 1\text{g}\right|$. However, it is rather difficult to select and distinguish the appropriate threshold levels. Consequently, the defined threshold levels can easily result in a false external acceleration. Moreover, the scalar dynamic acceleration α provides brief and instantaneous results that do not provide an overall picture of the dynamics of the system.

The proposed approach takes advantage of the high sampling frequency of the employed accelerometer and formulates an accumulated measure to describe the magnitude of the external acceleration. The accumulated measure given by equation (3.22) utilizes a window of length L and integrates the instantaneous scalar dynamic acceleration. Therefore, the average acceleration provides a broad description of the dynamic behavior of the system. The window size can be varied based on the application design requirements, and, for shorter delays, smaller L values can be chosen. For simplicity, $L = 400$ has been chosen to synchronize the measures. The average acceleration can be calculated as:

$$\hat{\alpha} = \frac{1}{L}\sum_{k=1}^{L} \alpha_k, \quad \alpha_k = \left|\sqrt{A_{x,k}^2 + A_{y,k}^2 + A_{z,k}^2} - 1\text{g}\right|, \tag{3.22}$$

where $A_{x,k}$, $A_{y,k}$, and $A_{z,k}$ are the measurements of the three-axis accelerometer. Therefore, similarly to the vibration measurement, the magnitude of the external acceleration $\hat{\alpha}$ is determined by collecting data packets of length L from the accelerometer and calculating the mean value of the scalar dynamic acceleration.

Fig. 3.7 depicts the determination of the external acceleration magnitude over a section of the 350 sec measurement. The blue curve shows the real external acceleration (α) applied to the test bench and measured by the plate encoder, while the red curve highlights the average dynamic acceleration ($\hat{\alpha}$) determined by equation (3.22). The average dynamic acceleration describes the dynamical behavior of the system accurately.

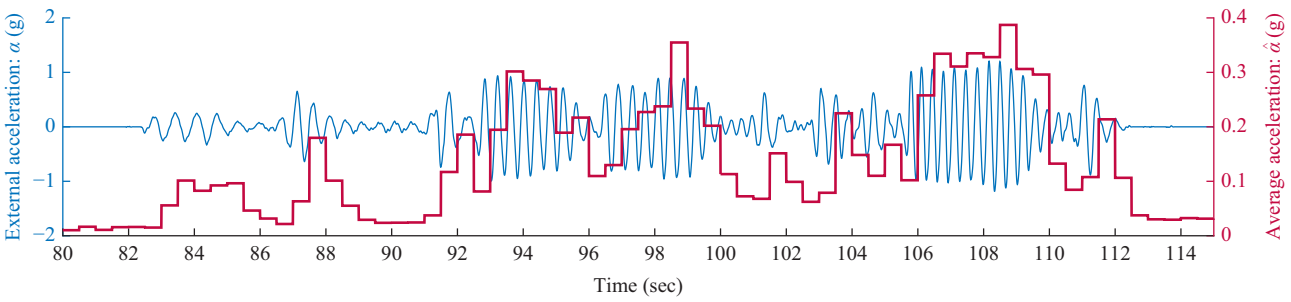

Figure 3.7: Real-time determination of the external acceleration magnitude.

3.1.4.3 Fuzzy inference machine

Using the measures $\hat{f}$ and $\hat{\alpha}$, deductions relevant to the dynamical behavior of the system can be made. Hence, the measurement noise variance $R = \rho$ can be manipulated according to these parameters. The gyro-related noise is not sensitive to either the external acceleration or the vibrations (i.e., constant process noise covariance $Q = \text{diag}(q_{00}, q_{11})$ can be considered). Consequently, an adaptive filtration is established to vary the noise variance ρ as a function of the measures $\hat{f}$ and $\hat{\alpha}$.

Fuzzy reasoning enables deductions to be made using simple IF-THEN linguistic rules. Because fuzzy sets are applied, there is no need for complex mathematical relations. Instead, mapping between $\hat{f}$, $\hat{\alpha}$ and the noise variance ρ can be performed using heuristic knowledge. The algorithm is composed of three main steps: the fuzzification of crisp inputs, fuzzy output calculations based on empirical IF-THEN rules, and the defuzzification of the fuzzy output Wang (1997); these steps have been described in detail in subsection 2.2.2.1. The empirical IF-THEN rules are usually aggregated based on both observations related to the system and human common sense. In my case, the initial deductions consist of two points:

1. IF the system is in a stationary (non-accelerating) mode, THEN there exists a well-chosen ratio between the noise covariance values Q and R yielding a satisfactory state estimation performance, whereas

2. IF external disturbances are present during the dynamical behavior, THEN (it is expected that the attitude realization $\theta_{A,k}$ is characterized by high uncertainty, and therefore) the measurement noise variance ρ should be increased so that the KF relies more heavily on the gyroscope data.

Fig. 3.8 depicts the structure of the proposed adaptive KF. A two-input one-output fuzzy inference machine is implemented, which forms a zero-order Sugeno systems. The machine's inputs are the external disturbance magnitudes $\hat{f}$ and $\hat{\alpha}$, while its output is a weighting factor denoted by K that weights the noise variance (i.e., the adaptive measurement noise variance is formulated as $R = K\rho$).

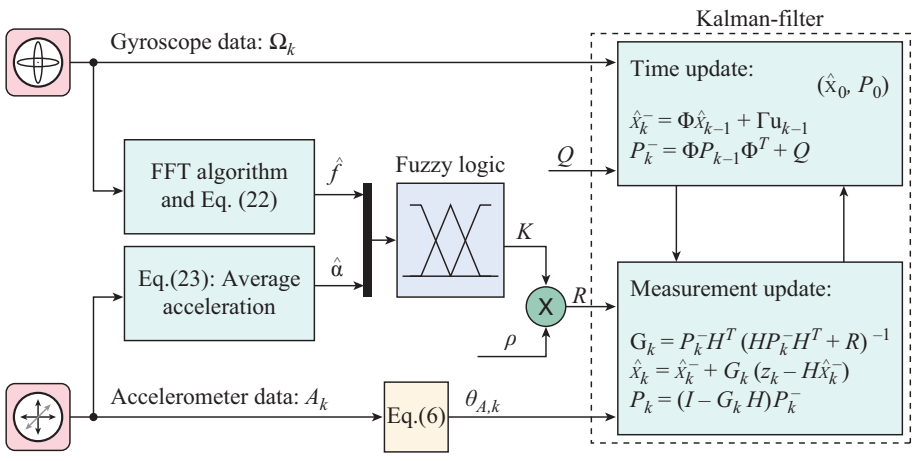

Figure 3.8: Structure of the adaptive Kalman filter approach.

The ranges of the input variables are defined based on the fact that the maximum values of $\hat{f}$ and $\hat{\alpha}$ are about 6.5 Hz and 0.35 g, respectively, while the output range has been chosen intuitively via iterative tuning. The inputs are covered by three membership functions (one triangular and two trapezoidal fuzzy sets) where Z (zero), S (small), and B (big) describe the magnitudes of $\hat{f}$ and $\hat{\alpha}$. In terms of the output, five singleton consequents $(K_1, ..., K_5)$ representing the scaling magnitude are defined. Fig. 3.9 shows the input and output membership functions and the properties of the fuzzy inference machine, while Fig. 3.10 depicts the corresponding fuzzy surface.

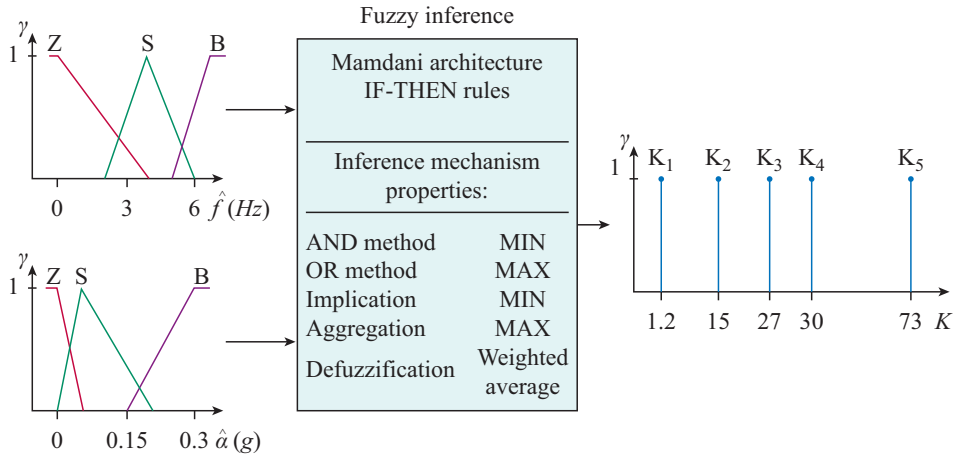

Figure 3.9: Properties of the applied fuzzy inference machine.

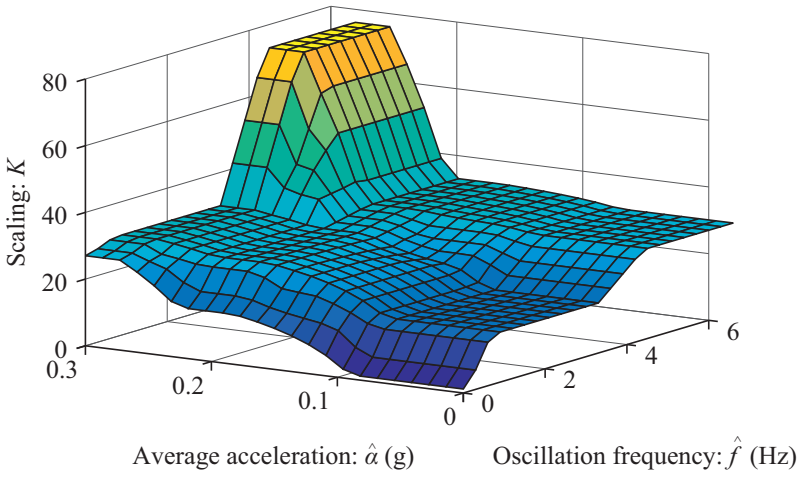

Figure 3.10: Generated surface related to the fuzzy rule base.

The aforementioned initial deductions are expanded into nine rules. These rules describe the scaling of the noise variance ρ according to the magnitudes of both the instantaneous vibration and the external acceleration (see equation (3.23)). The rule base is summarized in Table 3.2. For example, IF the vibration is close to zero and the external acceleration is big, THEN the moderate scaling K_3 is applied, while IF both the vibration and the external acceleration are big, THEN the largest scaling K_5 is chosen.

Table 3.2: Rule base of the fuzzy inference machine.

Scaling factor K		Ext. accel. $\hat{\alpha}$		
		Z	**S**	**B**
Vibration $\hat{f}$	**Z**	K_1	K_2	K_3
	S	K_2	K_3	K_4
	B	K_3	K_4	K_5

$$
\begin{aligned}
&\text{Rule1} \;:\; \text{IF } \hat{f} \text{ is Z and } \hat{\alpha} \text{ is Z THEN } K \text{ is } K_1 \\
&\text{Rule2} \;:\; \text{IF } \hat{f} \text{ is Z and } \hat{\alpha} \text{ is S THEN } K \text{ is } K_2 \\
&\text{Rule3} \;:\; \text{IF } \hat{f} \text{ is Z and } \hat{\alpha} \text{ is B THEN } K \text{ is } K_3 \\
&\text{Rule4} \;:\; \text{IF } \hat{f} \text{ is S and } \hat{\alpha} \text{ is Z THEN } K \text{ is } K_2 \\
&\text{Rule5} \;:\; \text{IF } \hat{f} \text{ is S and } \hat{\alpha} \text{ is S THEN } K \text{ is } K_3 \\
&\text{Rule6} \;:\; \text{IF } \hat{f} \text{ is S and } \hat{\alpha} \text{ is B THEN } K \text{ is } K_4 \\
&\text{Rule7} \;:\; \text{IF } \hat{f} \text{ is B and } \hat{\alpha} \text{ is Z THEN } K \text{ is } K_3 \\
&\text{Rule8} \;:\; \text{IF } \hat{f} \text{ is B and } \hat{\alpha} \text{ is S THEN } K \text{ is } K_4 \\
&\text{Rule9} \;:\; \text{IF } \hat{f} \text{ is B and } \hat{\alpha} \text{ is B THEN } K \text{ is } K_5
\end{aligned}
\tag{3.23}
$$

Since the fuzzy architecture executes weighted average defuzzification, therefore the resulting crisp output (weighting factor K) and the adaptive measurement noise variance (R) are given as:

$$
\begin{aligned}
K &= \frac{\sum_{i=1}^{9} \kappa^i \cdot \min\left(\gamma^i\left(\hat{f}\right), \gamma^i\left(\hat{\alpha}\right)\right)}{\sum_{i=1}^{9} \min\left(\gamma^i\left(\hat{f}\right), \gamma^i\left(\hat{\alpha}\right)\right)}, \\
R &= K\rho,
\end{aligned}
\tag{3.24}
$$

where $\gamma^i(\hat{f})$ and $\gamma^i(\hat{\alpha})$ are the ith-rule fired membership function values and κ^i denotes the singleton value of the consequent (K) of the ith rule (see Fig. 3.9).

3.1.4.4 Results

A flexible, adaptive filter structure has been established based on the implementation of the aforementioned fuzzy inference machine. However, the noise covariance values Q and R have to be reselected by taking into account the fact that the measurement noise covariance R scales according to the dynamical behavior. Since both the optimization environment and the fitness function had already been established, it is feasible to re-execute the optimization for Q and R in the adaptive structure.

Table 3.3 illustrates the optimization results. All of the initial noise variance values have been set based on the results of subsection 3.1.3.4, except for the variance ρ, which has been initiated with a smaller value since it scales with the fuzzy output K according to the fuzzy surface depicted in Fig. 3.10. The optimization algorithm has been executed twice in succession.

The optimized variances are highlighted in the third column of Table 3.3. The ratio between the noise variances have decreased (compared to the results in Table 3.1) due to the algorithm's adaptive characteristics. The algorithm's inherent flexibility have allowed the process noise variance q_{00} to converge to a value ten times larger than in the previous case, resulting in faster estimation dynamics, whereas the process noise variance q_{11} has converged to a notable bigger value as well. This outcome was expected, because the fuzzy scaling causes measurement noise variance ρ to increase each time a disturbance occurs, and, via this mechanism, the reliability of the accelerometer-based results is controlled in real-time.

Both the adaptive KF approach and the optimized noise variances further improve the state estimation performance (i.e., the fitness function value has settled at $F_{adapt} = 1.6990$). Compared to the optimized $F_{opt} = 1.9077$ fitness function value from section 3.1.3, the adaptive KF approach has improved the overall filtration performance by 10.9%. These results demonstrate that a superior filter convergence can be achieved by varying the noise variances according to the magnitudes of external disturbances.

Table 3.3: Initial and optimized values and optimization bounds (for the adaptive case).

First run: $F_{init} = 1.7596 \rightarrow F_{opt} = 1.6995$

Symbol	Initial	Optimized	min	max
ρ	0.05	0.14805	0.005	0.2
q_{00}	$7 \cdot 10^{-8}$	$2.71 \cdot 10^{-7}$	$1 \cdot 10^{-8}$	$3 \cdot 10^{-7}$
q_{11}	$5 \cdot 10^{-12}$	$3.09 \cdot 10^{-12}$	$2 \cdot 10^{-12}$	$5 \cdot 10^{-11}$

Second run: $F_{init} = 1.7054 \rightarrow F_{opt} = F_{adapt} = 1.6990$

Symbol	Initial	**Optimized**	min	max
ρ	0.14	**0.31969**	0.05	0.43
q_{00}	$3 \cdot 10^{-7}$	$\mathbf{5.86 \cdot 10^{-7}}$	$6 \cdot 10^{-8}$	$8 \cdot 10^{-7}$
q_{11}	$4 \cdot 10^{-12}$	$\mathbf{6.43 \cdot 10^{-12}}$	$1 \cdot 10^{-12}$	$1 \cdot 10^{-11}$

3.1.5 Comparison

This subsection presents a comparison of the KF and adaptive KF approaches presented in subsections 3.1.3 and 3.1.4, respectively, against the commonly used orientation estimation methods Mahony *et al.* (2008) and Madgwick *et al.* (2011). These filters (hereinafter Mahony and Madgwick filters) have gained extensive interest in the robotics and control community Euston *et al.* (2008); Tsagarakis *et al.* (2017) and their performance is regularly taken into account as a benchmark in comparative analyses Cavallo *et al.* (2014); Valenti *et al.* (2015); Mourcou *et al.* (2015). To consider the best performances in this analysis and conduct a fair comparison, the parameters of both filters are optimized in the same environment using the same fitness function, data set (sensor data and sampling time), and optimization procedure as discussed in subsection 3.1.3. The implementation of the Mahony and Madgwick filters is based on the sample codes Madgwick (2010).

3.1.5.1 Optimized Mahony filter

Complementary filters use frequency domain information (instead of statistical descriptions) to filter and combine signals provided by sensors that have complementary spectral characteristics. This also allows fast response and accuracy in orientation estimation.

Reference Mahony *et al.* (2008) formulated the filtering problem as a deterministic observation problem posed directly on the special orthogonal group $SO(3)$ driven by reconstructed attitude and angular velocity measurements. As a result, an explicit complementary filter was proposed that provides good orientation and gyro bias estimates based on accelerometer and gyroscope data. This nonlinear quaternion-based complementary filter first calculates the orientation error using the accelerometer data and the orientation determined in the previous step; then, a proportional and integral (PI) controller is employed to correct the gyroscope measurement. Through the integration of the quaternion propagation and normalization a new estimate of orientation is obtained.

For my tests, the adjustable K_P, K_I parameters of the PI controller have been initially set to 0.5 and 0, respectively; then, the optimization of these parameters has been executed using equation (3.22) and the PSO algorithm with $n_{gen} = 20$ and $n_{pop} = 20$. The results in Table 3.4 demonstrate that the optimization noticeably improve the filter performance; i.e., the initial fitness function value $F_{init} = 2.0042$ has been reduced to $F_{opt} = 1.7849$ with the tuned K_P, K_I parameters.

Table 3.4: Initial and optimized values and optimization bounds (for the Mahony filter).

First run: $F_{init} = 2.0042 \rightarrow F_{opt} = 1.8276$

Symbol	Initial	Optimized	min	max
K_P	0.5	0.3502	0.35	0.7
K_I	0	$0.993 \cdot 10^{-4}$	0	0.005

Second run: $F_{init} = 1.8274 \rightarrow F_{opt} = 1.7849$

Symbol	Initial	**Optimized**	min	max
K_P	0.35	**0.2613**	0.125	0.4
K_I	$1 \cdot 10^{-4}$	$\mathbf{2.3158 \cdot 10^{-4}}$	0	$4 \cdot 10^{-4}$

3.1.5.2 Optimized Madgwick filter

The Madgwick filter also uses a quaternion representation of orientation. Its specificity lies in the application of accelerometer data in an analytically derived and optimized gradient descent algorithm to compute the direction of the gyroscope measurement error as a quaternion derivative. The output of this algorithm yields a drift corrective step that maintains the gyro data-based quaternion propagation.

The initial value of the filter's adjustable parameter β has been set to 0.1; then, optimization has been performed using equation (3.22) and the PSO algorithm with $n_{gen} = 10$ and $n_{pop} = 10$. Table 3.5 summarizes the outcome of the optimization, where the optimized $\beta = 0.0387$ is actually quite close to the value recommended in reference Madgwick *et al.* (2011). The executed optimization improve the fitness function value from the initial $F_{init} = 2.8091$ to $F_{opt} = 2.1206$.

Table 3.5: Initial and optimized values and optimization bounds (for the Madgwick filter).

First run: $F_{init} = 2.8091 \rightarrow F_{opt} = 2.1228$				
Symbol	Initial	Optimized	min	max
β	0.1	0.0371	0.02	0.15

Second run: $F_{init} = 2.1333 \rightarrow F_{opt} = 2.1206$				
Symbol	Initial	**Optimized**	min	max
β	0.035	**0.0387**	0.01	0.06

3.1.5.3 Results

Based on the optimization results, the largest fitness function value ($F_{opt} = 2.1206$) corresponds to the performance of the Madgwick filter (the smaller the value, the better the performance). This drawback is related to the filter's constant gain property, meaning that it is unable to adapt to dynamic circumstances and modify its parameter based on the magnitudes of both the instantaneous vibration and the external acceleration. The KF discussed in subsection 3.1.3 provided a slightly more robust estimation performance. The filter parameters are also constant values, but the combination of the optimized noise variances (ρ, q_{00} and q_{11}) results in a slightly better fitness function value ($F_{opt} = 1.9077$). The advantage of the KF can be related to its higher flexibility (three filter parameters) and its state-space model based property, which is characterized by noise statistics. The Mahony filter display the second-most competitive performance with a $F_{opt} = 1.7849$ fitness function value. This nonlinear complementary filter has overcame the effect of dynamic motion and disturbances despite its constant gain property. The well-tuned proportional and integral controller (K_P and K_I parameters) have allowed it to achieve satisfactory filter performance. However, the most robust filter performance in the high accelerating and vibrating test environment is attained by the adaptive KF discussed in subsection 3.1.4 ($F_{opt} = 1.699$). The improved fit is achieved through the application of adaptive gains that are modified according to the perceived external disturbances.

In order to show the generality and robustness of the obtained adaptive KF, the performances of the analyzed filters have been evaluated on four independent measurements (Measurement 1-4 lasted for 120, 170, 155, 150 sec, respectively). The executed measurements are characterized by the presence of magnitudes of external accelerations, angular velocities and oscillation frequencies. The dynamic circumstances in which the filter performance has been investigated are depicted on normalized histograms in Fig.3.11. The first row shows the presence of different external acceleration magnitudes. It can be observed, that in approximately 65% of every measurement, external acceleration has been applied in the range $(0, 3.85]$ g, where the most intense circumstances appear in the fourth measurement (indicated by the purple curve in Fig. 3.11). The second row illustrates that angular velocities varied in the range $(0, 735]$ degs^{-1} in about 80% of each measurement. Finally, the third row shows the different IB oscillation frequencies, that were present during these measurements. It can be seen that, in the range of $[0, 9]$ Hz, the analyzed oscillation frequencies are present roughly in the same ratio.

Table 3.6 summarizes the filters' performances based on the mean squared error (MSE) and standard deviation (STD) of the attitude estimation error results, proving that the adaptive KF introduced in subsection 3.1.4 outperforms the other filtering methods in each measurement.

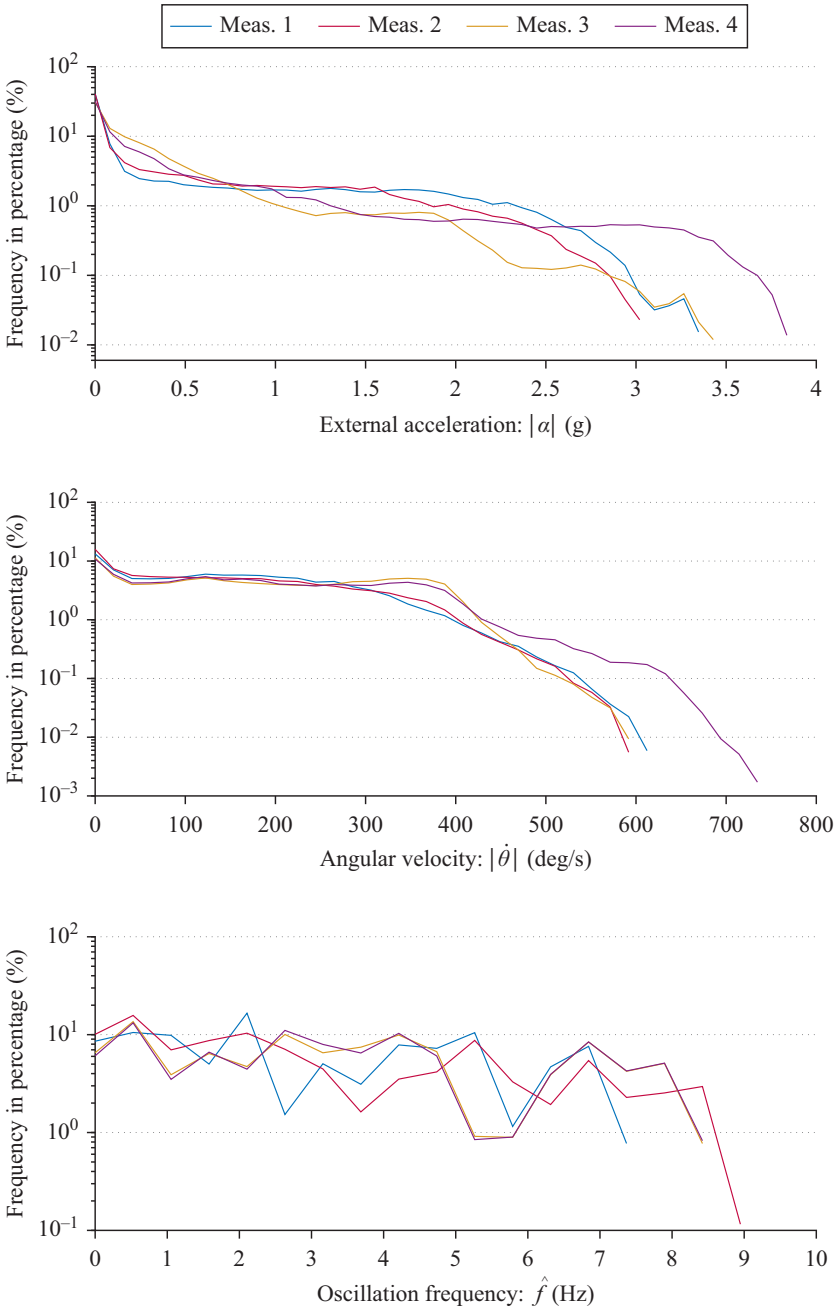

Figure 3.11: Characterization of the executed measurements.

Table 3.6: MSE and STD results of the investigated filters.

Filter	Measurement 1		Measurement 2		Measurement 3		Measurement 4	
	MSE	STD	MSE	STD	MSE	STD	MSE	STD
KF	1.5525	1.2452	1.7138	1.3089	2.2762	1.4860	2.6376	1.4754
Madgwick	2.1219	1.3316	4.1010	1.8919	2.4844	1.5762	2.6097	1.6017
Mahony	1.5772	1.1694	1.7591	1.2295	2.0404	1.4283	2.3340	1.5080
Adaptive KF	**1.4310**	**1.1896**	**1.5485**	**1.2160**	**1.9109**	**1.3810**	**2.2614**	**1.4357**

The results in Table 3.6 validate the performance of the proposed filtering approach. Nevertheless, it is worth mentioning that the generality and flexibility of this adaptive KF allows for further improvements. Some potential improvements are as follows.

1. Employing a more sophisticated fuzzy inference machine in which the fuzzy input-output ranges are partitioned into additional fuzzy sets (resulting in an advanced rule base).

2. Optimizing the shapes and ranges of the membership functions and the weights of the applied rules.

3. Extending the fuzzy inference machine with an additional output (two-input two-output fuzzy machine) that also weights the noise variances of the gyro measurements.

4. Varying the window size in the calculation of external disturbance magnitudes in order to obtain more precise estimates of the vibration frequency and the average external acceleration.

5. Extending the filter structure with additional sensor information, e.g., with a tri-axis magnetometer.

6. Employing an acceleration model in the state space equations (e.g., similar to reference Lee *et al.* (2012)), where the driving noise varies based on the disturbance magnitudes.

These issues are left open for investigation in future studies. I have demonstrated that the methods for measuring external disturbance magnitudes provide relevant system behavior information. These methods can be applied to any motorized robotic system (e.g., one involving UAVs), where vibrations and external acceleration are the two primary sources of disturbance. I have also demonstrated that fuzzy logic provided a simple, expert-oriented solution to establishing complex relations between the aforementioned disturbances and the filter parameters by formulating a set of heuristic IF-THEN rules. In my case, the KF was based on a simple two-dimensional state-space model of IMU data in which the measurement noise variance was manipulated based on the system behavior. Both the proposed fuzzy inference machine and the proposed disturbance measurement methods can be used to tune other filters in real time. This means that novel adaptive (and nonlinear) complementary filters (e.g., similar to reference Euston *et al.* (2008)) can be formed and their performances can be investigated for different mechatronic applications. Additionally, the proposed disturbance measurement methods can be employed in the elaboration of adaptive control (e.g., adaptive PID) solutions.

3.2 MARG-based Attitude Estimation

The original source is Odry *et al.* (2020b): Odry, Á., Kecskes, I., Sarcevic, P., Vizvari, Z., Toth, A., and Odry, P. A Novel Fuzzy-Adaptive Extended Kalman Filter for Real-Time Attitude Estimation of Mobile Robots. *Sensors*, **20**(3), 803.

The previous section validated the developed techniques for one-dimensional attitude estimation using a linear KF. Since the investigation showed promising results, thereby it is motivating to extend the estimation problem to the complete orientation based on MARG systems. Therefore, this section addresses the reliable and robust attitude estimation problem in the three-dimensional space and develops a novel qAEKF, in which new methods are employed to measure the external disturbances and their effect is suppressed with adaptation laws described with fuzzy logic-based IF-THEN rules.

3.2.1 Quaternion-Based Attitude Formulation

Let $\mathcal{E}$ and $\mathcal{S}$ denote the earth and sensor frames, also called the global non-moving inertial and local mobile frames, respectively. These frames can be defined with the conventional North-East-Down (NED) configuration often applied for robotic applications Liu *et al.* (2019); Roh and Kang (2018); Zhang and Liao (2017). Namely, the x-axis points north and y is directed east, whereas z completes the right-handed coordinate system by pointing down in the inertial reference frame (see Fig. 3.12). Additionally, the origin of the right-handed sensor frame is attached to the center of mass of the moving body, where the x-axis points forward and the y-axis is directed to the right of the body. The mapping between these frames $\mathcal{E}$ and $\mathcal{S}$ is described by a rotation matrix as

$$^{\mathcal{E}}x = {}^{\mathcal{E}}_{\mathcal{S}}R\,{}^{\mathcal{S}}x, \tag{3.25}$$

where $^{\mathcal{E}}x$ and $^{\mathcal{S}}x$ denote the 3×1 vector observations in the earth and sensor frames, respectively. Moreover, ${}^{\mathcal{E}}_{\mathcal{S}}R \in SO\,(3)$ indicates the 3×3 special orthogonal matrix, where the inverse transformation is defined as ${}^{\mathcal{E}}_{\mathcal{S}}R^{-1} = {}^{\mathcal{E}}_{\mathcal{S}}R^{T} = {}^{\mathcal{S}}_{\mathcal{E}}R$.

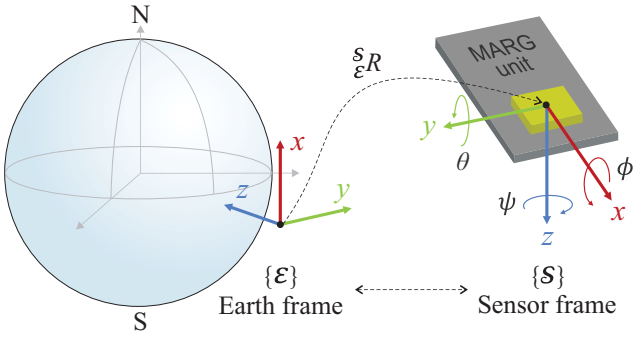

Figure 3.12: Relative orientation between the earth frame ($\mathcal{E}$) and sensor frame ($\mathcal{S}$).

The quaternion representation provides an effective way to both formulate the aforementioned rotation matrix and describe the attitude of the coordinate frames in three-dimensional space Kuipers *et al.* (1999). The advantageous structure both provides fast computation (compared to DCM) and completely avoids the well-known singularity problem of Euler angles (also known as the gimbal lock problem) Diebel (2006). The unit quaternion formulated by the four-dimensional vector ${}^{\mathcal{E}}_{\mathcal{S}}q \in \mathcal{R}^4$, $\left\|{}^{\mathcal{E}}_{\mathcal{S}}q\right\| = 1$ describes the attitude of frame $\mathcal{E}$ relative to frame $\mathcal{S}$ as a rotation by an angle μ about the unit vector $e = (e_x, e_y, e_z)^T$, which represents the rotation axis in $\mathcal{S}$. This rotation quaternion is interpreted as ${}^{\mathcal{E}}_{\mathcal{S}}q = \left(\cos\frac{\mu}{2}, e^T \cdot \sin\frac{\mu}{2}\right)^T = (q_0, \varrho)^T$, where q_0 and $\varrho = (q_1, q_2, q_3)^T$ denote the scalar and vector part terms, respectively. Co-ordinate transformation is performed by the non-commutative quaternion product denoted by $\otimes$:

$$^{\mathcal{E}}x = {}^{\mathcal{E}}_{\mathcal{S}}q \otimes {}^{\mathcal{S}}x \otimes {}^{\mathcal{E}}_{\mathcal{S}}q^{*}. \tag{3.26}$$

In equation (3.26), ${}^{\mathcal{E}}_{\mathcal{S}}q^{*} = (q_0, -\varrho)^T$ denotes the conjugate quaternion that describes the attitude of frame $\mathcal{S}$ relative to frame $\mathcal{E}$ (i.e., the inverse rotation is formulated as ${}^{\mathcal{E}}_{\mathcal{S}}q^{*} = {}^{\mathcal{S}}_{\mathcal{E}}q$). Moreover, $^{\mathcal{E}}x$ and $^{\mathcal{S}}x$ indicate the quaternions associated with the vector observations by their

augmentation with zero scalar parts ($q_0 = 0$) as $x = \left(0, x^T\right)^T$. The rotation can be rearranged into the initial equation (3.25) with the quaternion-parameterized rotation matrix

$$\begin{aligned} {}^{\mathcal{E}}_{\mathcal{S}}R\left(q\right) &= \left(q_0^2 - \varrho^T\varrho\right) I_3 + 2\varrho\varrho^T + 2q_0[\varrho\times] \\ &= \begin{bmatrix} q_0^2 + q_1^2 - q_2^2 - q_3^2 & 2\left(q_1q_2 - q_0q_3\right) & 2\left(q_1q_3 + q_0q_2\right) \\ 2\left(q_1q_2 + q_0q_3\right) & q_0^2 - q_1^2 + q_2^2 - q_3^2 & 2\left(q_2q_3 - q_0q_1\right) \\ 2\left(q_1q_3 - q_0q_2\right) & 2\left(q_2q_3 + q_0q_1\right) & q_0^2 - q_1^2 - q_2^2 + q_3^2 \end{bmatrix}, \end{aligned} \tag{3.27}$$

where I_3 is the identity matrix of size 3 and $[\varrho\times]$ denotes the antisymmetric matrix of ϱ, defined for the vector cross product $\varrho \times x = [\varrho\times]x$ as

$$[\varrho\times] = \begin{bmatrix} 0 & -q_3 & q_2 \\ q_3 & 0 & -q_1 \\ -q_2 & q_1 & 0 \end{bmatrix}. \tag{3.28}$$

Let ${}^{\mathcal{S}}\omega = \left(0, \omega_x, \omega_y, \omega_z\right)^T$ denote the four-dimensional quaternion formed by the angular velocities about the x, y, and z axes in the sensor frame. The time derivative of the quaternion ${}^{\mathcal{E}}_{\mathcal{S}}q$ represents the rate of change of attitude $\mathcal{E}$ relative to frame $\mathcal{S}$, according to the vector differential equation

$${}^{\mathcal{E}}_{\mathcal{S}}\dot{q} = \frac{1}{2}\,{}^{\mathcal{E}}_{\mathcal{S}}q \otimes {}^{\mathcal{S}}\omega = \frac{1}{2}Q\left(q\right){}^{\mathcal{S}}\omega, \quad Q\left(q\right) = \begin{bmatrix} q_0 & -\varrho^T \\ \varrho & q_0 I_3 + [\varrho\times] \end{bmatrix}, \tag{3.29}$$

where the matrix-vector product is indicated by the quaternion matrix $Q\left(q\right)$. The attitude of frame $\mathcal{E}$ relative to $\mathcal{S}$ is obtained by integrating the quaternion derivative ${}^{\mathcal{E}}_{\mathcal{S}}\dot{q}$. Therefore forth, the sub- and super-scripts are omitted, for the sake of simplicity.

I chose to use the Euler angles for the quality evaluation of attitude estimation, as their interpretation is straightforward for the reader. Euler angles (including yaw, pitch, and roll) describe the attitude as a sequence of three rotations, where ψ, θ, and ϕ denote the rotation angles about the z, y, and x axes, respectively. The quaternion output provided by the analyzed filters is converted to Euler representation as follows.

$$\begin{aligned} \phi &= \arctan2\left(2q_2q_3 - 2q_0q_1, 2q_0^2 + 2q_3^2 - 1\right), \\ \theta &= -\tan^{-1}\left(\frac{2q_0q_2 + 2q_1q_3}{\sqrt{1 - \left(2q_0q_2 + 2q_1q_3\right)^2}}\right), \\ \psi &= \arctan2\left(2q_1q_2 - 2q_0q_3, 2q_0^2 + 2q_1^2 - 1\right). \end{aligned} \tag{3.30}$$

3.2.2 Algorithm

Each sensor of a MEMS-based MARG unit provides useful information of the instantaneous attitude; however, none of the sensors are capable of providing reliable attitude results alone. As it was discussed in subsection 3.1.1, gyroscopes measure angular velocities; therefore, gyroscope-based attitude realization is obtained through numerical integration, but both the temperature-

dependent bias and noise contained in the measurements cause cumulative errors. An accelerometer measures the sum of gravitational and external accelerations. In stationary states, long-term stable attitude realization can be obtained based on the decomposition of the sensed gravity vector but, as external accelerations increase as a result of dynamic motion, the quality of attitude realization drastically deteriorates, making accelerometer-based realization highly unreliable. Magnetometers measure the geomagnetic field, which is used to determine heading information. However, the magnetic fluctuation of the environment caused by the perturbation of ferromagnetic objects highly disturbs the magnetometer output.

To provide reliable attitude estimation results, the individual features of each sensor are carefully addressed in the following.

3.2.2.1 Gyroscope model

Let Ω_k denote the raw measurement vector of a tri-axis MEMS gyroscope in the kth time instance. This measurement vector is composed of a 3×1 vector ω_k of true angular velocities around the x, y, and z axes, a vector $\bar{\omega}_k$ containing the non-static bias terms, and a vector μ_k of additive measurement noises. The imperfections of manufacturing results, in that the sensor model is extended with axis misalignment and scale factor errors, are represented by the 3×3 matrices M_Ω and ΔS_Ω, respectively. Moreover, the temperature sensitivity of the sensor makes the slowly varying bias vector $\bar{\omega}_k$ propagate as a random walk process characterized by a driving noise vector η_k, and therefore Aggarwal (2010)

$$\begin{aligned} \Omega_k &= (I + \Delta S_\Omega) M_\Omega \omega_k + \bar{\omega}_k + \mu_k, \\ \bar{\omega}_k &= \bar{\omega}_{k-1} + \eta_k. \end{aligned} \tag{3.31}$$

In the above measurement model, the rate noise vectors contain zero-mean white Gaussian variables for each axis (i.e., $E[\mu_k] = E[\eta_k] = 0$) and the covariance matrices are defined as $E\left[\mu_k \mu_l^T\right] = \Sigma_{\mu,k}\delta_{kl}$, $\Sigma_{\mu,k} \geq 0$, and $E\left[\eta_k \eta_l^T\right] = \Sigma_{\eta,k}\delta_{kl}$, $\Sigma_{\eta,k} \geq 0$, where δ_{kl} denotes the Kronecker delta.

Gyroscope-based (gyro-based) attitude realization is obtained by numerical integration of the true angular velocity vector ω_k in equation (3.31). Common calibration procedures performed in laboratories allow for the determination and compensation of the scale factor and misalignment errors. This process exceeds the scope of this article; therefore, I assume that the compensation has already been performed ($M_\Omega = I$ and $\Delta S_\Omega = 0$) Höflinger *et al.* (2013); Markley and Crassidis (2014); Nowicki *et al.* (2015). Based on equation (3.29), the gyro-based attitude realization is given in quaternion form as

$$q_{k+1} = q_k + \frac{T_s}{2} Q(q_k) \begin{bmatrix} 0 \\ \Omega_k - \bar{\omega}_k \end{bmatrix}, \tag{3.32}$$

where $T_s = 1/f_s$ is the sampling time. However, this method yields only short-tem accuracy, due to the presence of bias and measurement noise terms ($\bar{\omega}_k$ and μ_k) resulting in boundless drift in the attitude propagation.

3.2.2.2 Accelerometer and Magnetometer Models

The accelerometer and magnetometer sensors provide absolute reference observations, and therefore their measurements can be combined to determine the complete attitude of the sensor. The raw output A_k of a tri-axis MEMS accelerometer consists of four main components: the gravitational and external acceleration vectors g_k and α_k measured in the sensor frame ($\mathcal{S}$), the vector a_0 of bias terms, and the vector ν_k of additive measurement noises. Additionally, the raw measurement vector H_k of the tri-axis MEMS magnetometer model is composed of the true local magnetic field h_k sensed in $\mathcal{S}$, the sensor bias vector h_0, and the measurement noise vector ϵ_k:

$$\begin{aligned} A_k &= (I + \Delta S_A)\, M_A\, (\alpha_k + g_k) + a_0 + \nu_k, \\ H_k &= (I + \Delta S_H)\, M_H\, (B_{si} h_k + b_{hi}) + h_0 + \epsilon_k. \end{aligned} \tag{3.33}$$

Similarly to the gyroscope model, Gaussian noises are considered in the aforementioned models; therefore, $E[\nu_k] = E[\epsilon_k] = 0$ and the covariance matrices are $E\left[\nu_k \nu_l^T\right] = \Sigma_{\nu,k}\delta_{kl}$, $\Sigma_{\nu,k} \geq 0$ and $E\left[\epsilon_k \epsilon_l^T\right] = \Sigma_{\epsilon,k}\delta_{kl}$, $\Sigma_{\epsilon,k} \geq 0$. Beside the scaling and misalignment errors (ΔS_A, ΔS_H, M_A, and M_H), the magnetometer measurements are disturbed by magnetic soft iron and hard iron errors caused by the local environment, represented by the 3×3 matrix B_{si} and the 3×1 vector b_h, respectively. These model errors are determined via self-calibration procedures which address the time-invariant nature of the vector fields and map the distribution of the measurements on an ellipsoid Kok *et al.* (2012); Papafotis and Sotiriadis (2019); Sarcevic *et al.* (2019). We assume that the compensation has already been performed (therefore, $h_k := B_{si}^{-1} h_k - b_{hi}$), the bias and scale errors are zero, and the misalignment errors are identity matrices.

If a mobile mechatronic system stays in stationary states (i.e., no external acceleration is performed; $\alpha_k \approx 0$) and, moreover, if the local magnetic field is not perturbed by ferromagnetic objects, then the locally constant reference vectors can express the observations, with the help of the rotation matrix, as

$$\begin{aligned} {}^{\mathcal{S}}A_k &= {}^{\mathcal{S}}_{\mathcal{E}}R\,(q_k)\, {}^{\mathcal{E}}g, \\ {}^{\mathcal{S}}H_k &= {}^{\mathcal{S}}_{\mathcal{E}}R\,(q_k)\, {}^{\mathcal{E}}h. \end{aligned} \tag{3.34}$$

In the aforementioned configuration, the gravity vector is given as ${}^{\mathcal{E}}g = (0, 0, 9.81)^T$, whereas the magnetic field vector is ${}^{\mathcal{E}}h = (b\cos(\sigma), 0, b\sin(\sigma))^T$ in SI units, where b and σ denote the magnitude of the Earth's geomagnetic field and inclination angle, respectively.

Let the components of an inertial frame in both $\mathcal{S}$ and $\mathcal{E}$ be expressed by constructing two triads of orthonormal unit vectors. The first triad is defined with the reference vectors in $\mathcal{E}$ as

$$\hat{s}_1 = \frac{{}^{\mathcal{E}}g}{\|{}^{\mathcal{E}}g\|}, \quad \hat{s}_2 = \frac{{}^{\mathcal{E}}g \times {}^{\mathcal{E}}h}{\left\|{}^{\mathcal{E}}g \times {}^{\mathcal{E}}h\right\|}, \quad \hat{s}_3 = \hat{s}_1 \times \hat{s}_2. \tag{3.35}$$

The second triad is constructed with the observation vectors in frame $\mathcal{S}$, where

$$\hat{r}_1 = \frac{{}^{\mathcal{S}}A_k}{\left\|{}^{\mathcal{S}}A_k\right\|}, \quad \hat{r}_2 = \frac{{}^{\mathcal{S}}A_k \times {}^{\mathcal{S}}H_k}{\left\|{}^{\mathcal{S}}A_k \times {}^{\mathcal{S}}H_k\right\|}, \quad \hat{r}_3 = \hat{r}_1 \times \hat{r}_2. \tag{3.36}$$

Based on equations (3.34), (3.35), and (3.36), first the measurement (observation) and reference matrices are formed, then the rotation matrix is determined as:

$$M_{\text{mea}} = \left[\hat{r}_1\, \hat{r}_2\, \hat{r}_3\right], \quad M_{\text{ref}} = \left[\hat{s}_1\, \hat{s}_2\, \hat{s}_3\right], \quad {}^{\mathcal{S}}_{\mathcal{E}}R\left(q_k\right) = M_{\text{mea}} M_{\text{ref}}^T. \tag{3.37}$$

The determined rotation matrix ${}^{\mathcal{S}}_{\mathcal{E}}R\left(q_k\right) = \left(r_{ij}\right)$ enables the calculation of the quaternion representing the attitude of the sensor frame:

$$q_0 = \frac{1}{2}\sqrt{1 + r_{11} + r_{22} + r_{33}}, \quad q_1 = \frac{r_{23} - r_{32}}{4q_0}, \quad q_2 = \frac{r_{31} - r_{13}}{4q_0}, \quad q_3 = \frac{r_{12} - r_{21}}{4q_0}. \tag{3.38}$$

The aforementioned algorithm is the well-known TRIAD Shuster and Oh (1981); Markley and Crassidis (2014), which produces the raw attitude realization based on accelerometer and magnetometer measurements. The attitude realization, which is described by equation (3.38), is denoted by $q_{k,\text{TRIAD}} = \left(q_0, q_1, q_2, q_3\right)^T$ and can also be considered as the sum of the real attitude characterized by the quaternion q_k in the kth time instance and an additive Gaussian white noise, v_k, which represents the effects of ν_k and ϵ_k from equation (3.33) after the TRIAD output is evaluated:

$$q_{k,\text{TRIAD}} = q_k + v_k, \quad E\left[v_k\right] = 0, \quad E\left[v_k v_l^T\right] = \Sigma_{v,k}\delta_{kl}, \Sigma_{v,k} > 0. \tag{3.39}$$

This algorithm is characterized by a simple and straightforward implementation and, therefore, it is a popular choice for raw attitude determination Wen *et al.* (2019); Roh and Kang (2018). However, it has a disadvantage in producing large errors when dynamic conditions are present or external magnetism disturbs the sensor readings. As a result, if external acceleration is performed ($\alpha_k \neq 0 \rightarrow {}^{\mathcal{S}}A \neq R\,{}^{\mathcal{E}}g$) or ferromagnetic materials distort the geomagnetic field (${}^{\mathcal{S}}H \neq R\,{}^{\mathcal{E}}h$), then the attitude realization becomes unreliable with drastically reduced accuracy. This implementation method does not include any explicit models of external disturbances. Instead, the effects of external disturbances are absorbed by v_k in equation (3.39); that is, the additive noise is characterized by a significantly larger noise variance in disturbed environments.

3.2.2.3 Sensor fusion with Extended Kalman Filter

The MARG sensor-based attitude realizations described by equations (3.32) and (3.39) are utilized in a sensor fusion algorithm, which both synthesize the individual advantages and features of each sensor and provides attitude results with higher reliability and accuracy. First, this sensor fusion algorithm utilizes the gyroscope-based realization to propagate the attitude results, then these results are updated with the most recent quaternion realization derived from

accelerometer and magnetometer readings. This propagate-update mechanism provides both a smooth output and stability in the attitude results by compensating for the drift error generated in equation (3.32). The fusion of the sensor models is executed with an EKF.

The EKF effectively combines the noisy measurements and dynamic model-based predictions; moreover, in a recursive filter structure, it provides an approximate maximum-likelihood state estimate $\hat{x}$ of the stochastic nonlinear state-space model Markley and Crassidis (2014). In fact, the filter linearizes the nonlinear dynamic model around the last estimated state vector using the Jacobian matrix and, for the linearized dynamics, the linear KF is utilized, which is an optimal state estimator.

The mathematical models and statistical assumptions of MARG sensors, as introduced in the previous subsections, fully match the process and measurement equations of a stochastic nonlinear state-space model. Namely, the process model describes the quaternion propagation with both the discrete-time integrated angular velocities (equation (3.32)) and the random walk process of the bias term (equation (3.31)). Therefore, the dynamic model is defined with the 7×1 state vector $x_k = (q_k, \bar{\omega}_k)^T$, the 3×1 input vector $u_k = \Omega_k$, and the 7×1 process noise vector $w_k = \left(\mu_k^q, \eta_k\right)^T$, where μ_k^q represents the quaternion noise generated due to the gyroscope measurement noise μ_k. For the sake of comprehensiveness and to foster a straightforward implementation, I give the full description of state propagation in equation (3.40):

$$
\begin{aligned}
x_{k+1} &= f\left(x_k, u_k, w_k\right), \quad x\left(0\right) \\
\begin{bmatrix} q_0 \\ q_1 \\ q_2 \\ q_3 \\ \bar{\omega}_x \\ \bar{\omega}_y \\ \bar{\omega}_z \end{bmatrix}_{k+1} &= \begin{bmatrix} q_{0,k} + \frac{T_s}{2}\left(q_{1,k}\left(\bar{\omega}_{x,k} - \Omega_{x,k}\right) + q_{2,k}\left(\bar{\omega}_{y,k} - \Omega_{y,k}\right) + q_{3,k}\left(\bar{\omega}_{z,k} - \Omega_{z,k}\right)\right) + \mu_{0,k}^q \\ q_{1,k} - \frac{T_s}{2}\left(q_{0,k}\left(\bar{\omega}_{x,k} - \Omega_{x,k}\right) - q_{3,k}\left(\bar{\omega}_{y,k} - \Omega_{y,k}\right) + q_{2,k}\left(\bar{\omega}_{z,k} - \Omega_{z,k}\right)\right) + \mu_{1,k}^q \\ q_{2,k} - \frac{T_s}{2}\left(q_{3,k}\left(\bar{\omega}_{x,k} - \Omega_{x,k}\right) + q_{0,k}\left(\bar{\omega}_{y,k} - \Omega_{y,k}\right) - q_{1,k}\left(\bar{\omega}_{z,k} - \Omega_{z,k}\right)\right) + \mu_{2,k}^q \\ q_{3,k} + \frac{T_s}{2}\left(q_{2,k}\left(\bar{\omega}_{x,k} - \Omega_{x,k}\right) - q_{1,k}\left(\bar{\omega}_{y,k} - \Omega_{y,k}\right) - q_{0,k}\left(\bar{\omega}_{z,k} - \Omega_{z,k}\right)\right) + \mu_{3,k}^q \\ \bar{\omega}_{x,k} + \eta_{x,k} \\ \bar{\omega}_{y,k} + \eta_{y,k} \\ \bar{\omega}_{z,k} + \eta_{z,k} \end{bmatrix}
\end{aligned}
\tag{3.40}
$$

According to equation (3.39), the measurement model is characterized by a linear quaternion mapping. Therefore, it is formed with the 4×1 output vector $z_k = q_{k,\mathrm{TRIAD}}$ which provides the quaternion update as the TRIAD output, the measurement noise vector v_k, and the output matrix H, as

$$
\begin{aligned}
z_k &= Hx_k + v_k, \\
q_{k,\mathrm{TRIAD}} &= \begin{bmatrix} I_4 & 0_{4\times 3} \end{bmatrix} \begin{bmatrix} q_k \\ \bar{\omega}_k \end{bmatrix} + v_k.
\end{aligned}
\tag{3.41}
$$

If the $x\left(0\right)$ Gaussian vector in equation (3.40) is known along with its mean and covariance matrix; that is, if

$$
\hat{x}_0 = E\left[x\left(0\right)\right], \quad P_0 = E\left[\left(x\left(0\right) - \hat{x}_0\right)\left(x\left(0\right) - \hat{x}_0\right)^T\right], \tag{3.42}
$$

then the MARG sensor models fully satisfy the stochastic hypothesis. Namely, the process and measurement noise vectors are zero-mean white Gaussian variables, $x(0)$ is uncorrelated to w_k and v_k, and, moreover,

$$E\left[w_k v_l^T\right] = 0, \quad E\left[w_k w_l^T\right] = Q\delta_{kl}, \quad E\left[v_k v_l^T\right] = R\delta_{kl}, \tag{3.43}$$

where $Q \geq 0$ and $R > 0$ are the well-known process and measurement noise covariance matrices, respectively. The EKF algorithm provides a suboptimal state estimation $\hat{x}_k$ with minimized estimation error covariance. The state propagation, processing of the observations, and the covariance estimate update are performed through time and measurement update equations in the recursive filter structure; namely, the time update equations utilize the input variable u_k, the state estimation and error covariance obtained in the previous step ($\hat{x}_{k-1}$ and P_{k-1}), and the state dynamics $f(\hat{x}_{k-1}, u_k)$ to calculate the a priori state estimate ($\hat{x}_k^-$) and the corresponding error covariance (P_k^-):

$$\begin{aligned} \hat{x}_k^- &= f\left(\hat{x}_{k-1}, u_k\right), \\ P_k^- &= \Phi P_{k-1} \Phi^T + Q, \quad \Phi = \left.\frac{\partial f}{\partial x}\right|_{\hat{x}_{k-1}}. \end{aligned} \tag{3.44}$$

In equation (3.44), the Jacobian Φ is applied in the a priori covariance matrix update. To foster straightforward implementation, I give its full form as follows,

$$\Phi = \begin{bmatrix} 1 & \frac{T_s}{2}(\bar{\omega}_x - \Omega_x) & \frac{T_s}{2}(\bar{\omega}_y - \Omega_y) & \frac{T_s}{2}(\bar{\omega}_z - \Omega_z) & \frac{T_s}{2}q_1 & \frac{T_s}{2}q_2 & \frac{T_s}{2}q_3 \\ \frac{T_s}{2}(\Omega_x - \bar{\omega}_x) & 1 & \frac{T_s}{2}(\Omega_z - \bar{\omega}_z) & \frac{T_s}{2}(\bar{\omega}_y - \Omega_y) & -\frac{T_s}{2}q_0 & \frac{T_s}{2}q_3 & -\frac{T_s}{2}q_2 \\ \frac{T_s}{2}(\Omega_y - \bar{\omega}_y) & \frac{T_s}{2}(\bar{\omega}_z - \Omega_z) & 1 & \frac{T_s}{2}(\Omega_x - \bar{\omega}_x) & -\frac{T_s}{2}q_3 & -\frac{T_s}{2}q_0 & \frac{T_s}{2}q_1 \\ \frac{T_s}{2}(\Omega_z - \bar{\omega}_z) & \frac{T_s}{2}(\Omega_y - \bar{\omega}_y) & \frac{T_s}{2}(\bar{\omega}_x - \Omega_x) & 1 & \frac{T_s}{2}q_2 & -\frac{T_s}{2}q_1 & -\frac{T_s}{2}q_0 \\ 0 & 0 & 0 & 0 & 1 & 0 & 0 \\ 0 & 0 & 0 & 0 & 0 & 1 & 0 \\ 0 & 0 & 0 & 0 & 0 & 0 & 1 \end{bmatrix}. \tag{3.45}$$

The measurement update equations utilize both the observation vector, z_k (accelerometer and magnetometer-based attitude realization), and the measurement noise covariance, R, to correct the a priori state estimate. First, the Kalman gain matrix G_k is obtained, then the state estimate $\hat{x}_k$ and its error covariance P_k are corrected. The a posteriori estimation results are obtained in the following steps.

$$\begin{aligned} G_k &= P_k^- H^T \left(H P_k^- H^T + R\right)^{-1}, \\ \hat{x}_k &= \hat{x}_k^- + G_k\left(z_k - H\hat{x}_k^-\right), \\ P_k &= \left(I - G_k H\right) P_k^-. \end{aligned} \tag{3.46}$$

The estimation performance of EKF is mostly determined by the noise covariance matrices Q and R. Unfortunately, in practice, these parameters (i.e., the statistical description of the state and observation noises) are not fully measurable (or require time consuming, complex,

and extensive verification and validation procedures); especially in the case of MARG sensors, as the effects of both different noise sources and disturbances are represented with general noise vectors v_k and w_k in equations (3.40) and (3.41). Generally, the parameters Q and R are tuned based on engineering intuition through trial-and-error analysis; however as it was shown in the previous section, that method yields only a compromise solution between the estimation accuracy and filter dynamics. To overcome this compromise solution, I developed numerical optimization-based approaches in the previous section. As it was shown, that method both allows for evaluation of the best possible (achievable) estimation quality and provides the optimized parameters which maximize the filter performance. I recall this approach to find the optimized parameters of EKF in subsection 3.2.4.

3.2.3 Fuzzy-Adaptive Strategy

The adaptive approach varies the noise variances, according to both the instantaneous dynamical behavior and external disturbances, thus providing filter performance superior to that provided by the standard EKF. The instantaneous dynamics are characterized by the magnitudes of vibration and external acceleration of the sensor frame. Moreover, the adaptive strategy incorporates the magnitude of the distorted geomagnetic field as an external disturbance. The following subsections present the structure of the adaptive strategy, in which the extended measurement methods of external disturbances and the novel sophisticated fuzzy logic-based inference machine are implemented for the real-time tuning of the noise covariances.

The measurement methods for vibration and external acceleration calculation have been described in detail, with multiple examples and figures, in subsection 3.1.4 for the one-dimensional, IMU-based attitude estimation case. Since the application of these methods for the MARG-based case is straightforward, therefore only the essential information are repeated in the following subsections.

3.2.3.1 Measuring Vibration Magnitude

The system vibration magnitude is described by the oscillation frequency of the sensor frame. For estimation of the instantaneous oscillation frequency, gyroscope readings are utilized, as the sensors provides reliable angular rate measurements for both static and highly dynamic motions. The oscillation frequency is obtained by fast Fourier transform-based (FFT-based) evaluation of short angular rate measurement packets. Let L denote the length of these packets. Then, an oscillation frequency estimation $\hat{f}$ is calculated, in four steps; see the developed algorithm in subsection 3.1.4.1.

3.2.3.2 Measuring External Acceleration and Magnetic Perturbation Magnitudes

The external acceleration magnitude is calculated based on the accelerometer measurements. The system stays in stationary states (non-accelerating mode) if the magnitude of accelerometer readings is approximately equal to the norm of the reference vector $\left\|{}^{\mathcal{E}}g\right\|$. Therefore, the external acceleration magnitude $\Delta\alpha_k$ can be calculated as the difference between the norms of ${}^{\mathcal{S}}A_k$ and ${}^{\mathcal{E}}g$ in each sampling epoch. As it was discussed in subsection 3.1.4.2, the instantaneous difference does not provide an overall picture of the system dynamics, an accumulated measure

is thus utilized to describe the external acceleration magnitude. The accumulated measure $\hat{\alpha}_{\text{ext}}$ is formulated as the integrated scalar external acceleration for a window of length L (see equation (3.47)). This average external acceleration measure provides both useful and broad information of the instantaneous system dynamics.

$$\hat{\alpha}_{\text{ext}} = \frac{1}{L}\sum_{k=1}^{L} |\Delta\alpha_k| \,, \quad \Delta\alpha_k = \left\| {}^{\mathcal{S}}A_k \right\| - \left\| {}^{\mathcal{E}}g \right\| . \tag{3.47}$$

The magnetic perturbation magnitude is characterized based on the evaluation of the difference between the norms of ${}^{\mathcal{S}}H_k$ (instantaneous magnetometer measurement at epoch k) and ${}^{\mathcal{E}}h$ (reference magnetic field). If no magnetic disturbance is present, then the magnitude of magnetometer measurement is approximately equal to the norm of the reference vector. Otherwise, the magnitude of their difference gives an instantaneous measure of the perturbation magnitude. As it is difficult to draw conclusions based on this brief and instantaneous result at each epoch, similarity to the accelerometer readings, an accumulated measure, is thus applied to quantify the magnetic perturbation magnitude $\hat{h}_{\text{ext}}$:

$$\hat{h}_{\text{ext}} = \frac{1}{L}\sum_{k=1}^{L} |\Delta h_k| \,, \quad \Delta h_k = \left\| {}^{\mathcal{S}}H_k \right\| - \left\| {}^{\mathcal{E}}h \right\| . \tag{3.48}$$

Similarly to accelerometer and gyroscope sensors, the magnetic perturbation magnitude is determined by collecting data packets of length L from the magnetometer and computing the average magnetic field difference using equation (3.48).

3.2.3.3 Fuzzy Inference Machine

The measures $\hat{f}$, $\hat{\alpha}_{\text{ext}}$, and $\hat{h}_{\text{ext}}$ fully characterize both the instantaneous system dynamics and disturbance magnitudes. These results can be utilized in an inference system in which the noise covariance manipulation of the EKF is described according to the external effects. As a result, an adaptive strategy is established that (online) tunes the noise covariances as a function of the measures $\hat{f}$, $\hat{\alpha}_{\text{ext}}$, and $\hat{h}_{\text{ext}}$.

The relationships between the aforementioned measures and the EKF parameters are defined with fuzzy reasoning. As it was shown in the previous section, fuzzy logic does not require complex mathematical models from the system designer but, instead, it enables the implementation of deductions easily and effectively by using fuzzy sets and simple IF-THEN linguistic rules. Therefore, heuristic knowledge and a collection of deductions make such an inference system realizable. The main parts of the fuzzy inference machine has been discussed in subsection 2.2.2.1. Observations related to the system behavior and human common-sense contribute to collecting the empirical IF-THEN rules (deductions) that define the fuzzy inference machine. In the case of attitude estimation with MARG sensors, the two main deductions are as follows.

1. IF the sensor frame stays in stationary (non-accelerating and non-perturbed) mode, THEN a well-chosen ratio between the noise covariances Q and R yields satisfactory state estimation performance.

2. As the external disturbance effects are absorbed by the measurement noise v_k in equation (3.41), IF vibration, external acceleration, and magnetic perturbations disturb the MARG-based attitude realization, THEN the measurement noise covariance R should be increased according to the intensity of the measures $\hat{f}$, $\hat{\alpha}_{\text{ext}}$, and $\hat{h}_{\text{ext}}$ (i.e., higher noise variance characterizes the attitude realization $q_{k,\text{TRIAD}}$ with higher uncertainty).

The overall FAEKF structure is depicted in Fig. 3.13, where a three-input one-output fuzzy inference machine executes the online tuning of noise variances. The inputs of the fuzzy system are the measures $\hat{f}$, $\hat{\alpha}_{\text{ext}}$, and $\hat{h}_{\text{ext}}$, whereas weighting factors, denoted by K_R, are output weights for the R parameter (i.e., the adaptive strategy varies the measurement noise covariance matrix in each epoch k as $R_k = K_{R,k}R$). The ranges of the input variables $\hat{f}$ (Hz), $\hat{\alpha}_{\text{ext}}$ (g), and $\hat{h}_{\text{ext}}$ (normalized unit, nu), as well as the output variable K_R, ha been selected based on research results obtained in the one-dimensional case. Three Gaussian membership functions cover each input range, where the magnitudes of $\hat{f}$, $\hat{\alpha}_{\text{ext}}$ and $\hat{h}_{\text{ext}}$ are characterized by Z (zero), S (small), and B (big) fuzzy sets. The output ranges are covered with seven singleton consequents $(K_1, \cdots, K_7)$, which represent the scaling magnitudes. Both the applied membership functions and fuzzy inference system properties are depicted in Fig. 3.14. The fuzzy surfaces expressing the relationships between the crisp inputs and outputs are depicted in Fig. 3.15.

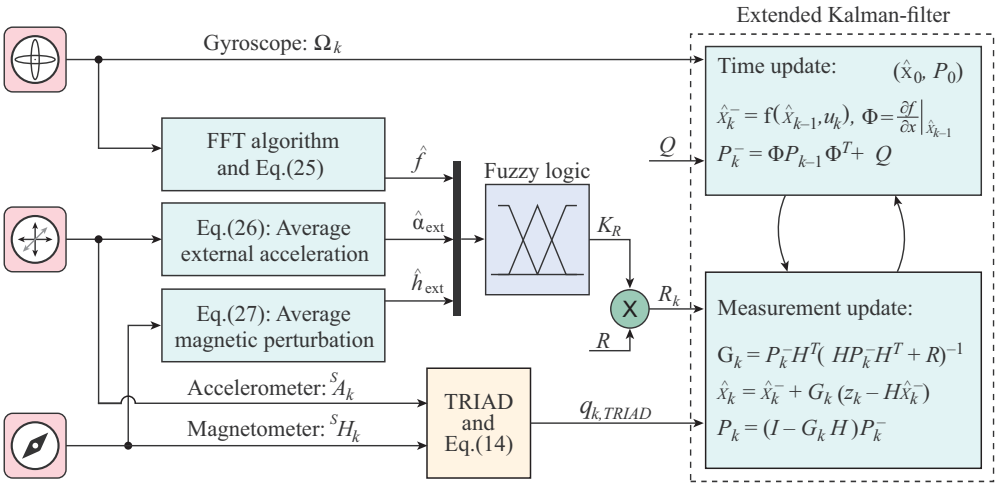

Figure 3.13: Structure of the FAEKF.

A sophisticated inference system is implemented, where the initial deductions described above are expanded into 27 rules. These simple IF-THEN linguistic rules completely describe the scaling of noise variances, according to the magnitudes of the external acceleration, vibration, and magnetic perturbation. The implemented rule base for K_R is summarized in Table 3.7. Two examples describe the interpretation of the implemented inference system, as follows:

1. IF the oscillation frequency $\hat{f}$ is zero (Z) and the external acceleration $\hat{\alpha}_{\text{ext}}$ and magnetic perturbation $\hat{h}_{\text{ext}}$ magnitudes are big (B), THEN a fairly large scaling factor ($K_R = K_5$) is applied for the measurement noise covariance. This collocation of the system state means that the observation is expected to have rather large uncertainty and, therefore, the algorithm relies more heavily on the state propagation (left side, second row, second column).

2. IF $\hat{f}$ is small (S) and the $\hat{\alpha}_{\text{ext}}$ and $\hat{h}_{\text{ext}}$ measures are close to zero (Z), THEN a smaller weight of $K_R = K_2$ is applied for R. Therefore, the algorithm considers the observation with higher reliability and maintains the correction of the state propagation by processing the measurements with higher significance (middle, first row, first column).

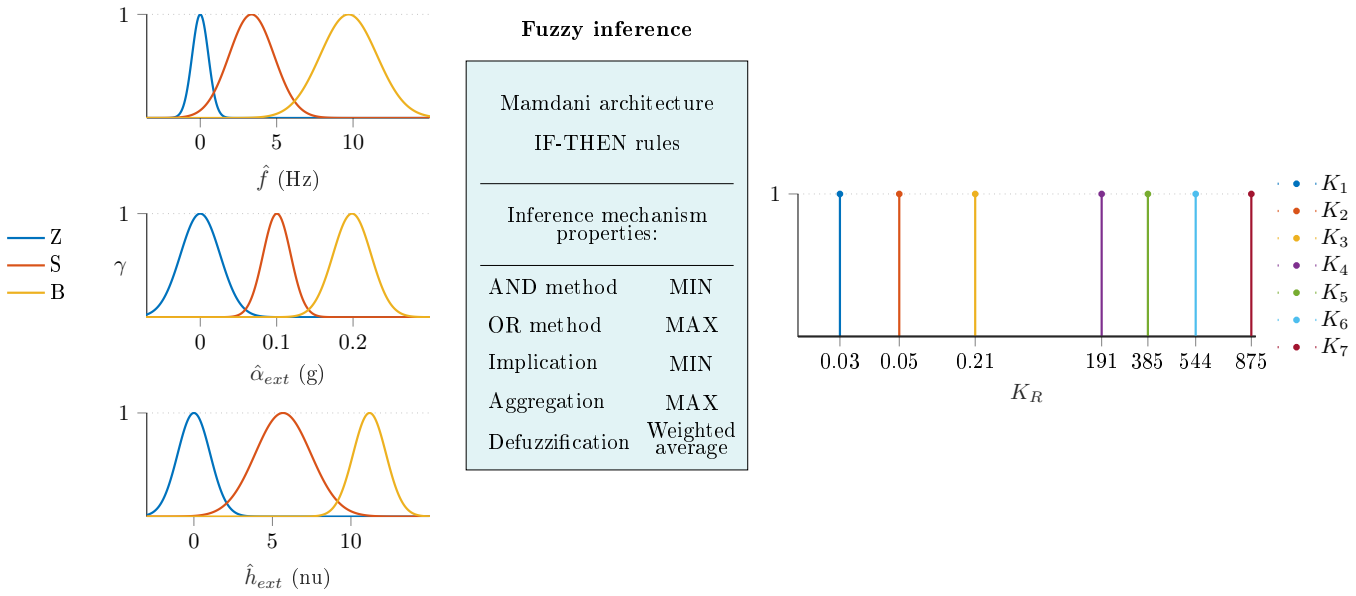

Figure 3.14: Properties of the applied fuzzy inference machine.

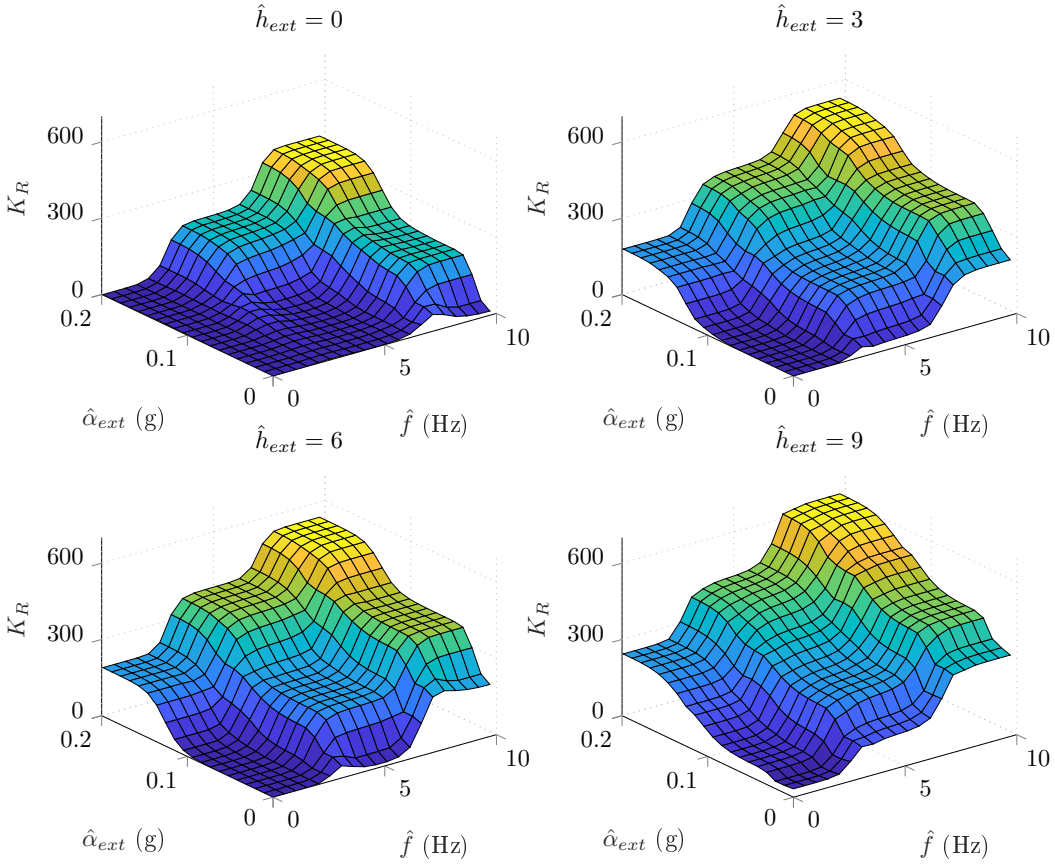

Figure 3.15: Generated surfaces related to the fuzzy rule base.

The crisp scaling factor is computed by weighted average-based defuzzification of the fuzzy output, in three steps (see the algorithm description in subsection 2.2.2.1). The proposed fuzzy inference machine is a zero-order Sugeno system. Therefore, the complete inference for the adaptive measurement noise covariances in each epoch k can be given in a compact form as

$$K\left(\kappa,\hat{f},\hat{\alpha}_{\text{ext}},\hat{h}_{\text{ext}}\right)=\frac{\sum_{i=1}^{27}\kappa^{i}\cdot\min\left(\gamma^{i}\left(\hat{f}\right),\min\left(\gamma^{i}\left(\hat{\alpha}_{\text{ext}}\right),\gamma^{i}\left(\hat{h}_{\text{ext}}\right)\right)\right)}{\sum_{i=1}^{27}\min\left(\gamma^{i}\left(\hat{f}\right),\min\left(\gamma^{i}\left(\hat{\alpha}_{\text{ext}}\right),\gamma^{i}\left(\hat{h}_{\text{ext}}\right)\right)\right)},$$
$$R_{k}=K_{R,k}R,\quad K_{R,k}=K\left(\kappa_{R},\hat{f}_{k},\hat{\alpha}_{ext,k},\hat{h}_{ext,k}\right),\quad \kappa_{R}=\left(K_{1},...,K_{7}\right)^{T}, \tag{3.49}$$

where $\gamma^{i}(\hat{f})$, $\gamma^{i}(\hat{\alpha}_{\text{ext}})$, and $\gamma^{i}(\hat{h}_{\text{ext}})$ are the ith-rule fired membership function values and κ^{i} denotes the singleton value of the consequent weighting factor of the ith rule for scaling the noise covariance R (see Figs. 3.13 and 3.14).

Table 3.7: Rule base of the fuzzy inference machine.

Vibration $\hat{f}=Z$		Mag. pert. $\hat{h}_{ext}$ Z	S	B
Ext. acc. $\hat{\alpha}_{ext}$	Z	K_1	K_2	K_3
	S	K_2	K_3	K_4
	B	K_3	K_4	K_5

Vibration $\hat{f}=S$		Mag. pert. $\hat{h}_{ext}$ Z	S	B
Ext. acc. $\hat{\alpha}_{ext}$	Z	K_2	K_3	K_4
	S	K_3	K_4	K_5
	B	K_4	K_5	K_6

Vibration $\hat{f}=B$		Mag. pert. $\hat{h}_{ext}$ Z	S	B
Ext. acc. $\hat{\alpha}_{ext}$	Z	K_3	K_4	K_5
	S	K_4	K_5	K_6
	B	K_5	K_6	K_7

3.2.4 Experimental Validation

This subsection describes the test platform employed in the evaluation of filter performance, the optimization approach utilized to tune the filter parameters, and the attitude determination results during different dynamic motions and external perturbations.

3.2.4.1 Test Environment

A comprehensive framework has been designed, in which a 6 DOF test bench dynamically alters the pose (position and orientation) of a MARG unit. This 6 DOF test bench is utilized to both simulate various (accelerating, non-accelerating, and vibrating) dynamic behaviors and measure the real attitude of the sensor frame, along with the raw MARG data. The framework is based on the widely used Robot Operating System (ROS) and the Gazebo open source dynamics simulator, which utilizes physics engines to consider the effects of gravity, friction, and forces Koenig and Howard (2004). As a result, this framework enables the evaluation of state estimation error, quantification of the filter performance, and tuning of filter parameters.

The designed test bench consists of three prismatic joints and three revolute joints. The prismatic joints make the sensor frame slide back and forth, up and down in the three dimensional (3D) space by three 3m long rails. The revolute joints set the instantaneous attitude (Euler angles) of the sensor frame. The MARG unit is attached to a plate at the end of this kinematic chain and, so, the 6 DOF system enables both the spatial coordinates and orientation of the sensor frame to be set and measured. Moreover, this 6 DOF mechanism enables the

generation of external accelerations simultaneously with sensor frame oscillations. Therefore, a variety of dynamic (vibrating and accelerating) system conditions can be simulated, where both the raw sensor data and real joint states are recorded. Fig. 3.16 shows the model of the test environment in Gazebo.

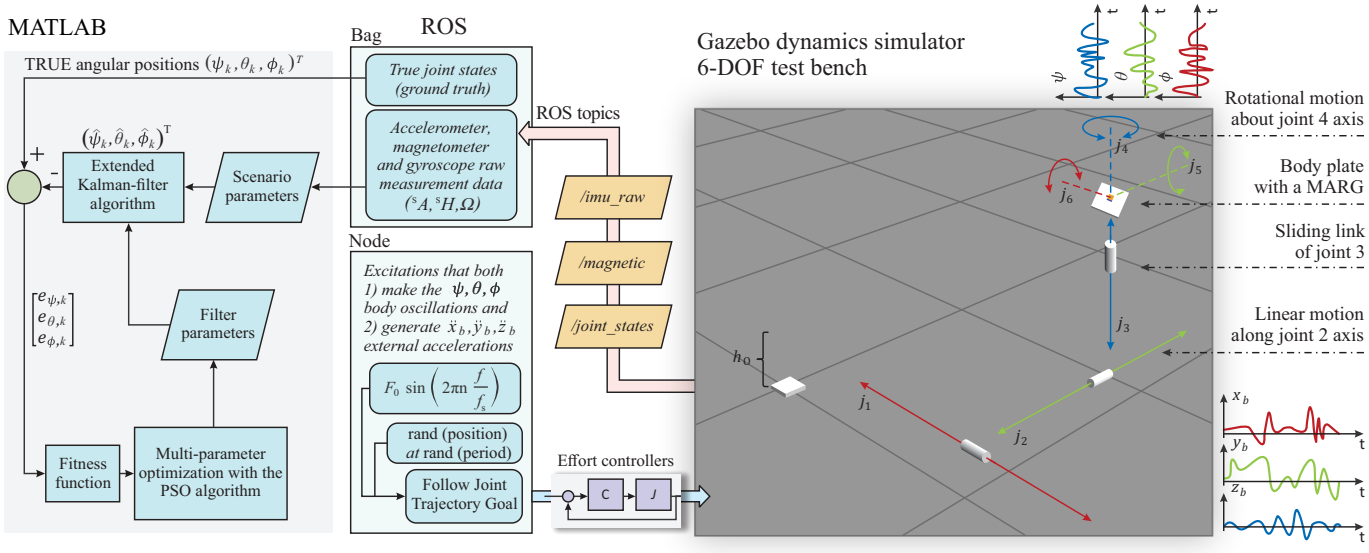

Figure 3.16: Block diagram of the test environment and filter tuning procedure (video of the closed-loop in Odry (2019a)).

Let x_b, y_b, and z_b denote the spatial coordinates of the body plate (i.e., the origin of the MARG unit). Then, the total kinetic energy T of the test platform is given as

$$T = \frac{1}{2}\dot{q}^T M_{\text{mass}} \dot{q}, \quad M_{\text{mass}} = \text{diag}\left((m_j + I_{3\times 1} m_b, J_b)\right), \tag{3.50}$$

where $m_j = (m_{j,1}, m_{j,2}, m_{j,3})^T$, $m_{j,i}$ denotes the mass of each prismatic joint for $i = \{1, 2, 3\}$, whereas m_b and $J_b = (J_{b,\phi}, J_{b,\theta}, J_{b,\psi})^T$ indicate the mass and moment of inertia of the body plate, respectively. Moreover, $q = (x_b, y_b, z_b, \phi, \theta, \psi)^T$ denotes the vector of generalized coordinates. The potential energy stored in the system is approximated as $P = \left(m_b + \sum_i^3 m_{j,i}\right) g h_0 + (m_b + m_{j,3})\, g z_b - m_{j,3} g h_1$, where the constants h_0 and h_1 denote the base height and distance between the body plate and third prismatic joint, respectively. The Lagrange function of the system is $\mathcal{L} = T - P$, where the motion of the system can be determined with the help of the Lagrange equations Bloch (2003). As a result, the equations of motion can be written in the following well-known form,

$$M(q)\,\ddot{q} + V(q, \dot{q}) = \tau_a - \tau_f, \tag{3.51}$$

where $M(q)$ is the inertia matrix, $V(q, \dot{q})$, including the Coriolis, centrifugal, and potential force terms, whereas τ_a and τ_f indicate the generalized external torques and friction effects, respectively.

The aforementioned dynamics are implemented in an Unified Robot Description Format (URDF) file Furrer *et al.* (2016). This file enables the specification of the whole geometric description of the system, including the robot kinematics, motion ranges, location of frames, mass

properties, and collisions. Each joint (DOF) is driven in a closed-loop with an independent PID effort controller. Each effort controller is implemented, using the *ros controllers* meta-package, as a single-input single-output (SISO) low-level controller, in which torque control action is applied to the joint. The PID parameters have been set up heuristically by iterative tuning in Gazebo. The true linear and angular positions of each joint are supplied by the *joint state controller*, a sensor controller that publishes the joint state information (i.e., true positions, velocities, and efforts are represented in double-precision floating-point format without measurement noise, discrepancy, or delay) Quigley *et al.* (2015); Koubâa (2017). In this application, the joint state information is obtained with a $f_s = 1$ kHz sampling frequency. The sensor measurements are provided by independent Gazebo plugins, developed in reference Meyer *et al.* (2012). These IMU and magnetic field sensor plugins are attached to the body plate of the 6 DOF test bench by including them in the URDF file.

To execute different acceleration and vibration dynamic motions, on one hand, random desired values are generated with random frequencies for the PID controllers of the three prismatic joints in their configuration space. On the other hand, different sinusoidal signals are supplied as reference values to the PID controllers of the three revolute joints, where both the amplitude and frequency are varied randomly. Therefore, the closed-loop system causes the 6 DOF mechanism to execute a wide variety of dynamic movements in the 3D space, with continuously varying oscillations and accelerations. Simultaneously, the three prismatic joints make the sensor frame slide back and forth, as well as up and down; simulating various external accelerations. The true joint states, along with the instantaneous MARG sensor data, have been collected to evaluate the attitude estimation performance.

Video demonstrations of the closed-loop dynamics have been shared online. Moreover, the whole ROS package, which includes the test bench properties, URDF files, applied effort controllers, and Gazebo configuration files, have been made publicly available in the supplementary online material, to help other lab teams evaluate similar experiments Odry (2019a).

3.2.4.2 Magnetic perturbations

Magnetic perturbations are generated artificially, as the Gazebo simulation environment does not contain such a feature. Therefore, based on the experimental results with magnetic disturbances conducted in Sarcevic and Pletl (2018); Borbás *et al.* (2018); Wu *et al.* (2019); Wu (2019), a simple algorithm has been developed to generate magnetic perturbations. The algorithm is composed of three main steps, which are described as follows.

1. Generate a perfect artificial signal m of length L_m as a mixture of square, saw-tooth, triangle, and two sinusoidal signals. Both the sequence of these signals and their parameters (i.e., the amplitude and frequency) are randomly selected.

2. Obtain the analytic signal m_a from m, where the real part is the original signal, while the imaginary part contains the Hilbert transform (i.e., the original signal with a $\pi/2$ phase shift Marple (1999)). Then, generate the artificial perturbation m_p as the sum of the imaginary part and absolute value of the Hilbert transformed complex signal, where the

sequence of absolute values is reversed in time:

$$\begin{aligned} m_{a,k} &= m_{r,k} + jm_{i,k}, \quad k = 1, ..., L_m, \\ m_{p,k} &= m_{i,k} + |m_{a,l}|, \quad k = 1, ..., L_m, \quad l = L_m, ..., 1. \end{aligned} \tag{3.52}$$

3. Remove the continuous linear trend of m_p and low-pass filter the detrended signal with a first order Butterworth infinite impulse response (IIR) filter.

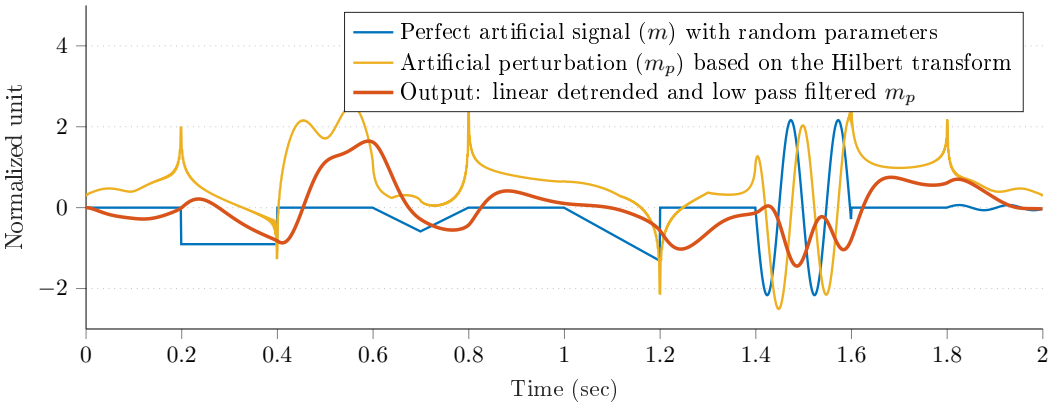

Figure 3.17: Demonstration of the proposed magnetic perturbation generator algorithm.

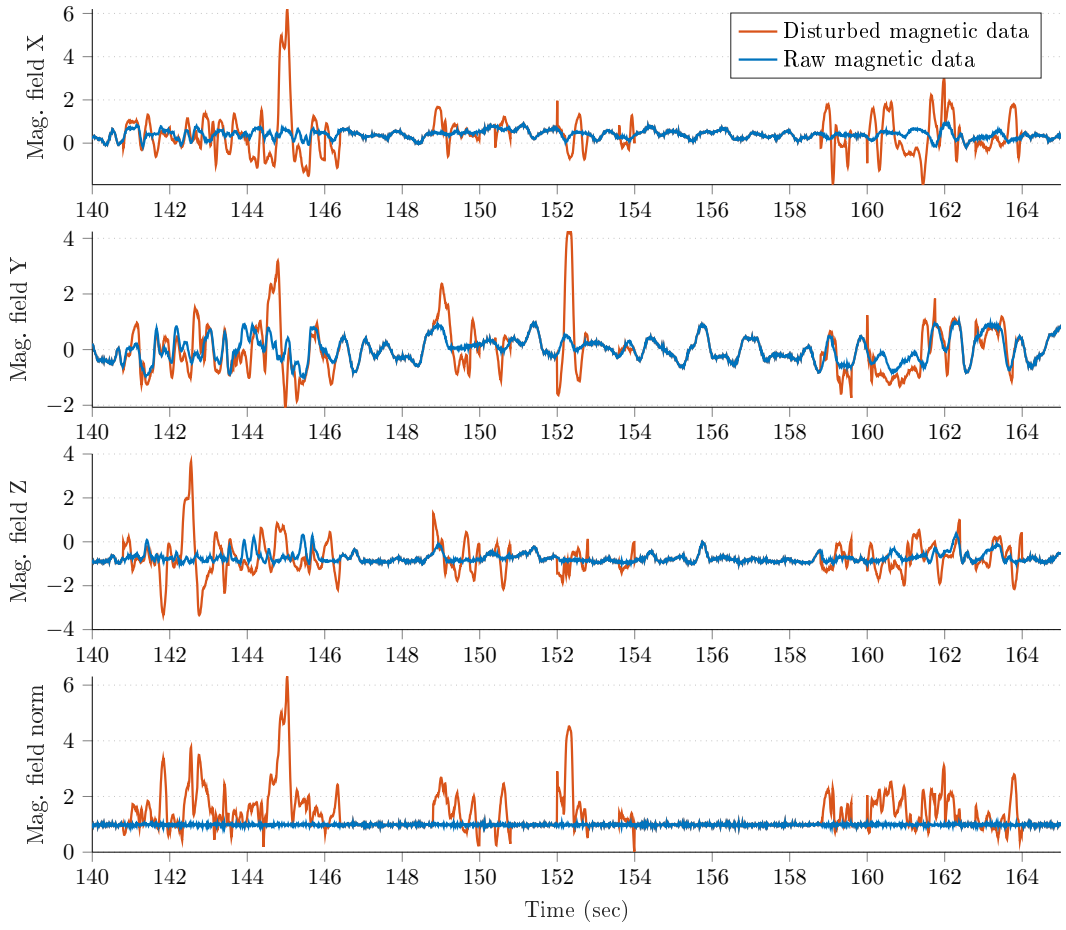

Figure 3.18: Magnetic field measurements before and after the application of the magnetic perturbation generator algorithm.

Each step of the aforementioned algorithm is depicted in Fig. 3.17. Moreover, Fig. 3.18 highlights the effect of the artificial perturbation on both the norm and each component of the raw magnetometer signal. The blue curves in Fig. 3.18 represent the raw (calibrated, undisturbed, and normalized) magnetometer measurements and the red curves show random sections, where the magnetometer is disturbed artificially with the proposed algorithm. These figures illustrate that the algorithm enables both generation of realistic magnetic perturbation effects and incorporation of effects of this type of disturbance into the analysis of attitude estimation.

3.2.4.3 Tuning of Filter Parameters

I recall the results of the initial parameter optimization problem addressed in subsection 3.1.3. Therefore, the tuning of filter parameters is executed in MATLAB on a training data set collected in the aforementioned test environment. The heuristic PSO algorithm is utilized for the filter tuning problem, as it does not require gradient information, guides the search well even in nonlinear noisy systems, and has demonstrated greater effectiveness and robustness than other optimization methods Kecskés and Odry (2014); Modares *et al.* (2010a); Kennedy *et al.* (2001). Both the algorithm and applied PSO-based optimization procedure have been presented in detail in subsection 3.1.3; therefore, only key information is described in the following paragraphs.

The inputs of the optimization problem are the real angular positions (i.e., the true Euler angles ϕ_k, θ_k, and ψ_k provided by the 6 DOF test bench) and MARG sensor data (i.e., the acceleration, angular velocity, and magnetic field measurements), whereas its outputs are the estimation errors $e_{\phi,k} = \phi_k - \hat{\phi}_k$, $e_{\theta,k} = \theta_k - \hat{\theta}_k$, and $e_{\psi,k} = \psi_k - \hat{\psi}_k$, where $\hat{\phi}_k$, $\hat{\theta}_k$, and $\hat{\phi}_k$ denote the estimated Euler angles (i.e., the outputs of the implemented filter algorithm). The PSO is a population-based search algorithm that guides the search in the search space by employing a fitness function. A complex fitness function is formulated for the problem to both quantify the differences between the true and estimated Euler angles and measure the overall filter performance. Three mean squared errors (MSE) are combined to evaluate the filtration quality. The PSO-based minimization of the following fitness function has enabled the filter parameters to be successfully tuned:

$$F = \sqrt[3]{\prod_{j=1}^{k_{\text{sce}}} \left(\frac{\sum_{k=1}^{N_j} e_{\phi,k}^2}{N_j} \right) \left(\frac{\sum_{k=1}^{N_j} e_{\theta,k}^2}{N_j} \right) \left(\frac{\sum_{k=1}^{N_j} e_{\psi,k}^2}{N_j} \right)}, \tag{3.53}$$

where k_{sce} denotes the number of scenarios taken into account in the optimization problem; N_j is the measurement length in the k_{sce}th scenario; and $e_{\phi,k}$, $e_{\theta,k}$, and $e_{\psi,k}$ indicate the roll, pitch, and yaw estimation errors, respectively. The optimization algorithm determines the optimal possible filter parameters, corresponding to the lowest possible fitness function value. The block diagram of the filter parameter optimization procedure is depicted in Fig. 3.16.

The optimization can begin running once the parameters are initialized. Both the PSO and filter parameters ($\hat{x}_0$, P_0, Q, and R) are initialized by employing the results presented in subsection 3.1.3. As the sampling time in the ROS-based framework is relatively low ($T_s = 1$ms), the adaptive strategy can be executed with bigger window size of $L = 400$; moreover, the

length of the transform is $L_{\mathrm{FFT}} = 2^9$ and the threshold oscillation frequency and amplitude are $f_{\mathrm{thr}} = 10$ Hz and $|\Omega|_{\mathrm{thr}} = 0.26$ rads^{-1}, respectively. The process noises μ_k^q and ν_k in equation (3.40) are considered to be statistically independent Lee *et al.* (2012); Nowicki *et al.* (2015); therefore, diagonal matrices are applied for both the process and measurement noise covariances with the following characteristics,

$$Q = \begin{bmatrix} I_4 \cdot Q_q & 0_{3\times4} \\ 0_{4\times3} & I_3 \cdot Q_{\bar{\omega}} \end{bmatrix}, \quad R = I_4 \cdot \rho, \tag{3.54}$$

where the Q_q, $Q_{\bar{\omega}}$, and ρ constant noise variances are tuned with PSO. As a result, the optimization has converged the quaternion measurement noise variance to a higher value of $\rho = 3.53$. This outcome was expected, as intense accelerations and vibrations have been applied with the 6 DOF test bench and the effects of these external disturbances are absorbed in the measurement noise v_k in equation (3.41). This high-noise variance value indicates that the TRIAD-based attitude realization is significantly more unreliable than the gyro-based state propagation, especially in highly dynamic states of the system. At the same time, the process noise variances has converged to noticeably small values (i.e., $Q_q = 1.45 \cdot 10^{-6}$ and $Q_{\bar{\omega}} = 9.71 \cdot 10^{-10}$), resulting in the state-space dynamics (equation (3.40)) becoming much more reliable than the measurement correction equations. The successful optimization contributes to finding the tuned EKF parameters which provide satisfactory attitude estimation quality with the help of the adaptive strategy described in subsection 3.2.3 for both static and extreme (vibrating and accelerating) dynamic conditions.

3.2.4.4 Results

The attitude estimation performance of the FAEKF is evaluated on three measurements performed in the test environment (Measurements 1–3 lasted for approximately 160s, 210s, and 315s, respectively). The dynamic motions executed by the 6 DOF test bench during these measurements included stationary states, slow and fast changes in angular positions, mild and intense oscillations, and external accelerations. The dynamic circumstances in which the filter performance is investigated are characterized by the following ranges; $0 - 8$ Hz for sensor frame oscillation frequency, ± 50 rads^{-1} for angular velocity, ± 16 g for external spatial acceleration, and $0 - 5$ nu for magnetic perturbation magnitude.

The robust filter performance in the highly disturbed (accelerating and vibrating) test environment is highlighted in Figs. 3.19–3.22. The first three rows of each figure show the roll (ϕ), pitch (θ), and yaw (ψ) angles, where the blue curve indicates the true Euler angles (obtained by the joint states ROS topic), whereas the red and yellow curves highlight the attitude estimation with and without the proposed fuzzy adaptive strategy, respectively. The fourth rows depict both the instantaneous external acceleration (blue curves) executed by the 6 DOF test bench and average dynamic acceleration (red curves) determined by equation (3.47). Similarly, the blue curve of the fifth row of each figure shows the instantaneous magnetic perturbation generated by equation (3.52), whereas the red curve indicates the average magnetic field difference calculated by equation (3.48). Finally, the sixth row depicts both the instantaneous angular rate magnitude (blue curves) and the oscillation frequency of the sensor frame (red curves). The last

three rows illustrate that the employed measurement methods in the adaptive strategy provide useful information related to the external acceleration, vibration, and magnetic disturbance magnitudes.

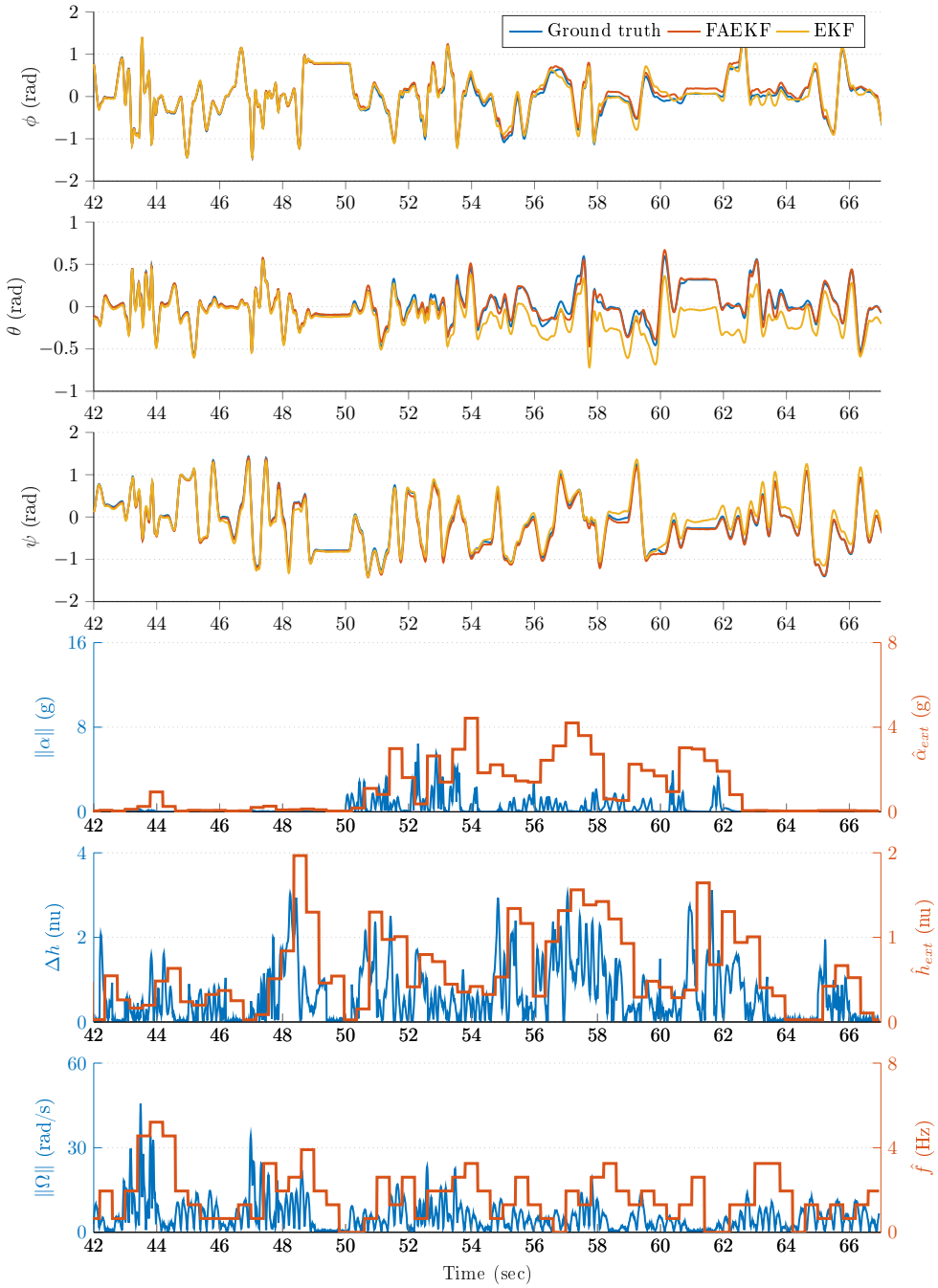

Figure 3.19: First time slot from the measurements. **(a-c)** show the roll, pitch and yaw angles; **(d-e)** show the external acceleration and magnetic perturbation magnitudes; **(f)** shows the oscillation frequency of the sensor frame.

The noticeable performance improvement provided by the fuzzy-adaptive strategy is highlighted both by the figures and the results included in Table 3.8. The curves corresponding to the FAEKF output fit to the true Euler angles to a satisfactory degree, both in frequencies and amplitudes; even when extreme external perturbations are present. The effects of these disturbances drastically decrease the performance of the standard EKF. For example, Fig. 3.19

highlights that, at approximately 50 sec, an increased external acceleration and magnetic perturbation influence the attitude estimation over a 15 sec long period. During this period, the effects of these disturbances are effectively suppressed by the FAEKF; the adaptation laws enable it to achieve satisfactory filter accuracy and convergence. It is also shown that, without the fuzzy-adaptive strategy, an unsatisfactory EKF performance is provided (Euler angles indicated with yellow curves). A similar outcome can be observed in Fig. 3.20; namely, the external acceleration and magnetic perturbation effects in the high vibrating environment contribute to a significant decrease in the EKF estimation quality (e.g., see the yellow curves at ˜140 sec).

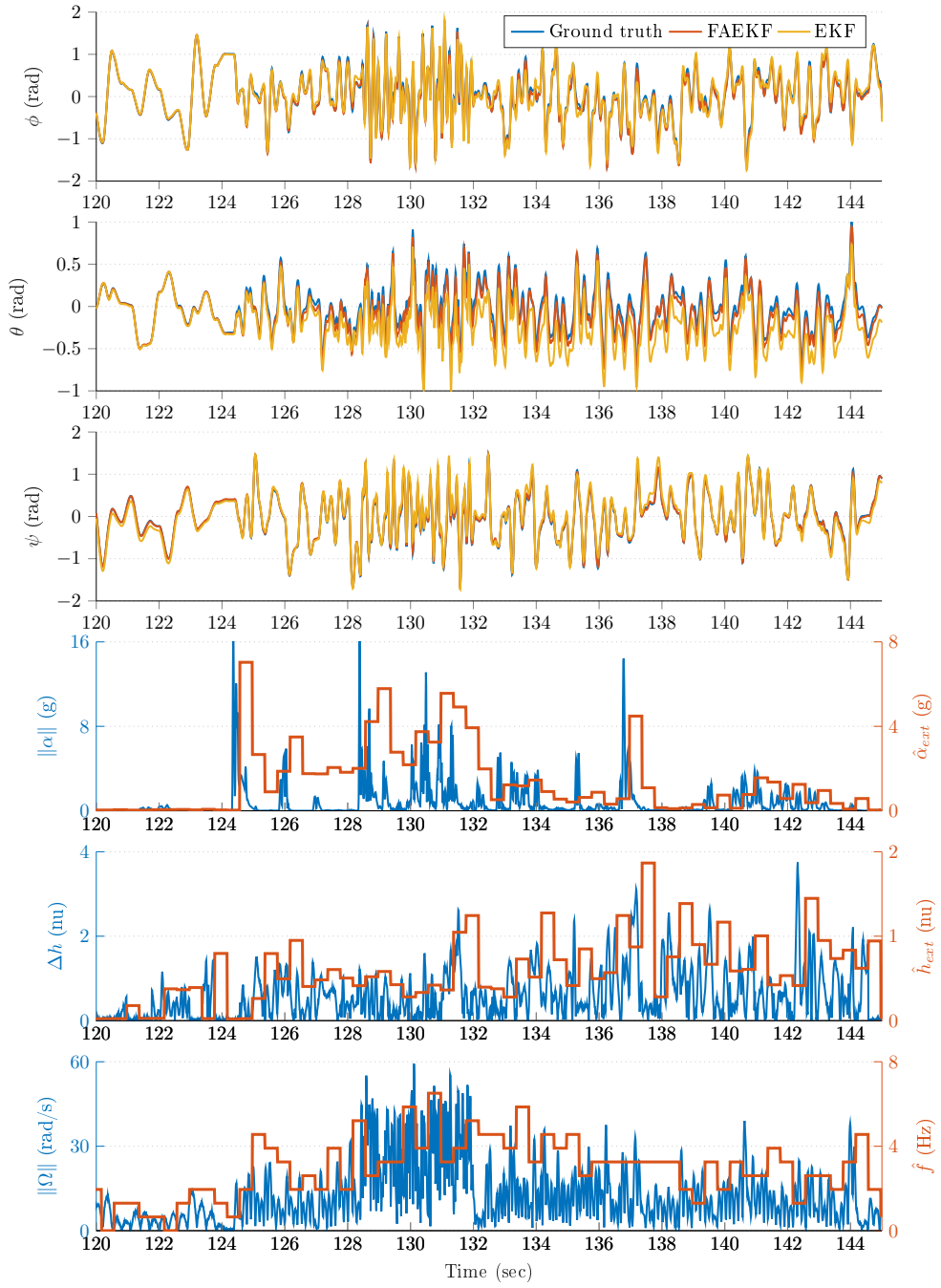

Figure 3.20: Second time slot from the measurements. **(a-c)** show the roll, pitch and yaw angles; **(d-e)** show the external acceleration and magnetic perturbation magnitudes; **(f)** shows the oscillation frequency of the sensor frame.

However, it is also shown that the adaptation laws enable cancellation of these effects, even under diverse dynamic conditions. Under static conditions, both EKF and FAEKF provide approximately the same performance levels; these results are highlighted in Figs. 3.21 and 3.22. As low-frequency oscillations along with no magnetic perturbation nor external acceleration enable the accelerometer- and magnetometer-based attitude realization (TRIAD output) to be characterized with high accuracy, the EKF can therefore provide satisfactory estimation quality based on the implemented state-space model. In these static cases, the adaptive strategy does not modify the noise variances, as the well-chosen ratio between the covariance parameters yields a satisfactory estimation quality.

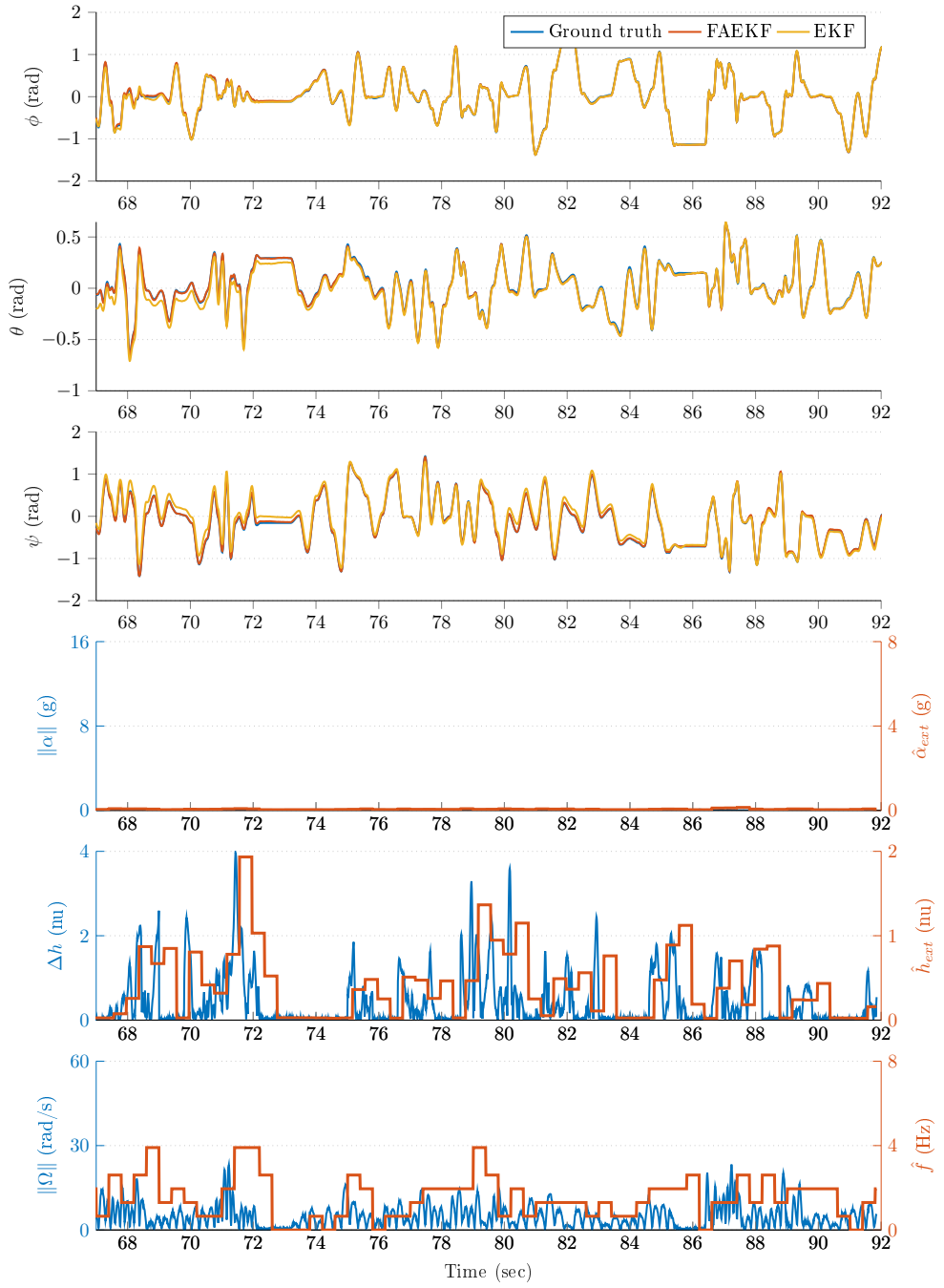

Figure 3.21: Third time slot from the measurements. **(a-c)** show the roll, pitch and yaw angles; **(d-e)** show the external acceleration and magnetic perturbation magnitudes; **(f)** shows the oscillation frequency of the sensor frame.

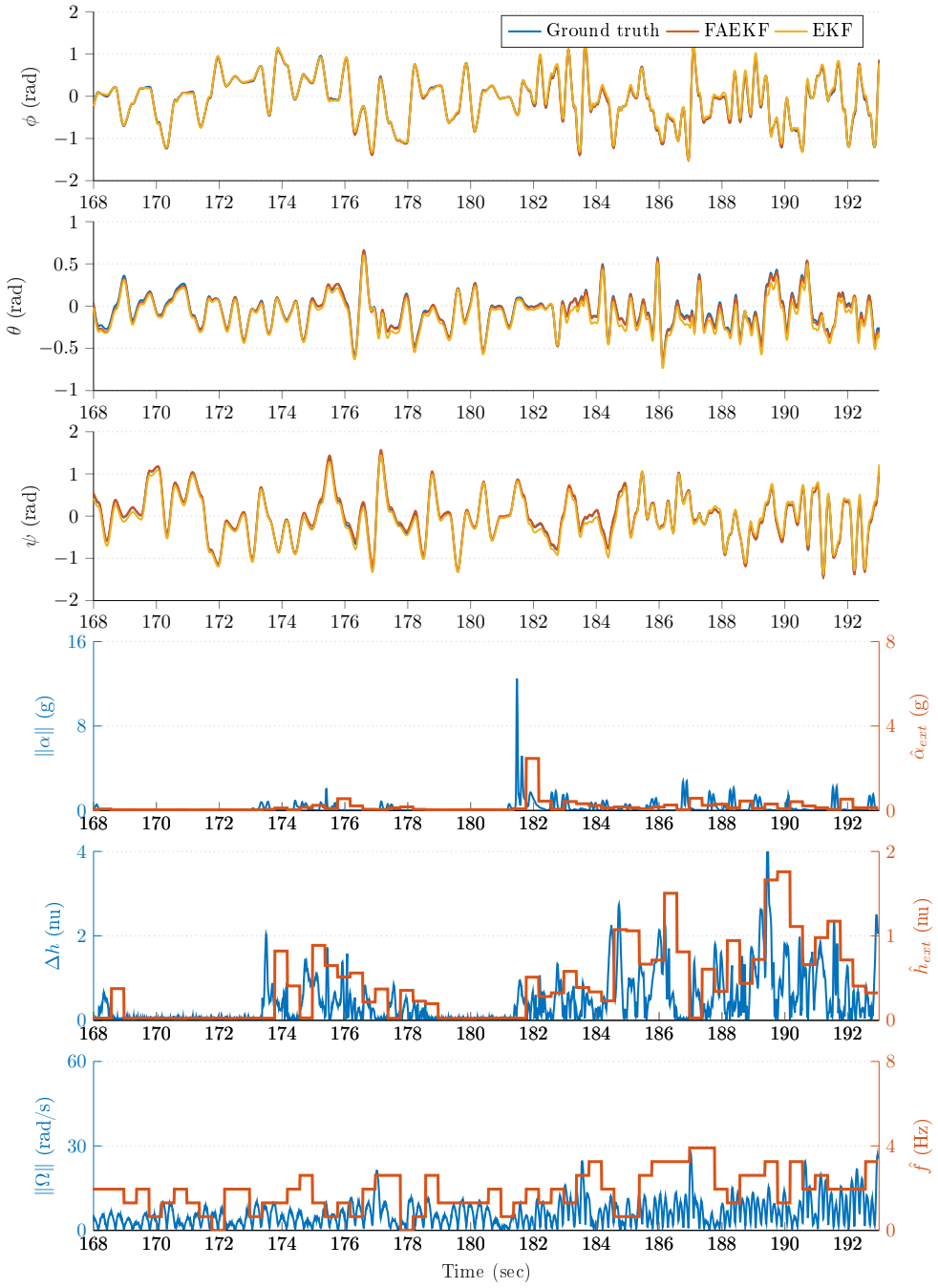

Figure 3.22: Fourth time slot from the measurements. **(a-c)** show the roll, pitch and yaw angles; **(d-e)** show the external acceleration and magnetic perturbation magnitudes; **(f)** shows the oscillation frequency of the sensor frame.

The filter performance is quantified with MSE and STD of the estimation error. These results are calculated for each measurement (M1, M2, and M3) and are summarized in Table 3.8. Based on the results, a significant improvement in the overall filter performance can be observed. In each measurement case, the yaw angle estimation is characterized by the smallest errors, while slightly less robust outputs are provided for the roll and pitch angle estimation. This outcome was expected in our configuration and is related to the TRIAD algorithm's characteristics. Namely, the impact of magnetometer readings relative to the vertical axis is eliminated in $\hat{s}_2$ and $\hat{r}_2$ (see equations (3.35) and (3.36)), therefore the pitch and roll angles are determined

based on only the accelerometer measurements Yun *et al.* (2008). As the accelerometer measurements have been disturbed much more heavily (via both the measurement noise and frequent external accelerations) than the magnetometer readings, therefore the disturbances influenced slightly more the roll and pitch estimation performance of the filter. Based on both the figures and Table 3.8, it can be concluded that a superior estimation convergence is achieved with the introduced adaptive strategy, thereby validating the performance of the proposed FAEKF approach.

Table 3.8: Mean squared error (MSE) and standard deviation (STD) results of the investigated filters.

Condition		roll (ϕ)		pitch (θ)		yaw (ψ)	
		MSE	STD	MSE	STD	MSE	STD
M1	**FAEKF**	0.0010	0.0301	0.0026	0.0421	0.0004	0.0188
	EKF	0.0037	0.0605	0.0127	0.0927	0.0099	0.0688
M2	**FAEKF**	0.0020	0.0433	0.0040	0.0536	0.0007	0.0261
	EKF	0.0089	0.0937	0.0252	0.1261	0.0085	0.0916
M3	**FAEKF**	0.0050	0.0695	0.0056	0.0548	0.0016	0.0405
	EKF	0.0046	0.0669	0.0102	0.0650	0.0089	0.0944

Nevertheless, some potential improvements are left open for investigation in future studies:

1. Employing a more robust deterministic approach to determine the quaternion from accelerometer and magnetometer observations in the measurement update state of the EKF.
2. Partitioning the fuzzy inputs and outputs into additional fuzzy sets, thereby implementing a more advanced fuzzy inference system.
3. Tuning the shapes of the applied fuzzy sets, the ranges of input and output variables, and the weights of the IF-THEN rules with the aid of optimization.
4. Varying the window size in the determination of external disturbance magnitudes, thereby providing more accurate measures for the adaptation laws.
5. Extending the state space model with external acceleration and magnetic perturbation models, where the driving Gaussian variables vary according to the external disturbance magnitudes.
6. Applying an additional output in the fuzzy inference system which weights the process noise covariance matrix.

Throughout the results, it has been demonstrated that the developed methods in the adaptive strategy provide relevant information of the environment in which attitude estimation is performed. The obtained external disturbance magnitudes has enabled to form an inference mechanism that effectively manipulate the noise variances on-the-fly, thereby providing superior filter performance. As external accelerations, magnetic perturbations, and vibration are common disturbance sources in motorized mechatronic systems, the developed method can be advantageously applied in such mechatronic systems. This work also demonstrates the benefits

of fuzzy logic, as it has provided an expert-oriented approach to implementing complex relations with the help of simple heuristic IF-THEN rules. The developed adaptation laws can be universally applied for the online tuning of any filter structure. Moreover, both the measurement methods and fuzzy inference mechanism can be intelligently employed in adaptive control solutions for mechatronic systems performing motions in unknown and/or disturbed environments (e.g., wheeled/legged robots moving on uneven terrain or UAVs maneuvering in windy environments).

3.3 Theses

This thesis group deals with the development and analysis of such soft computing-based methods, which provide enhanced state estimation performance in terms of robustness and accuracy for agile mechatronic systems executing both static and extreme dynamic motions.

3.3.1 Thesis 2.1

A fuzzy-adaptive KF has been established, which varies the filter parameters in real time based on the instantaneous system dynamics characterized by the magnitudes of external accelerations and vibrations. In this filter structure, the mapping between the instantaneous dynamics and KF parameters is realized by fuzzy-logic based heuristic IF-THEN rules. The proposed adaptive approach significantly improves the overall filter performance compared to the standard KF.

Publication pertaining to the thesis: Odry *et al.* (2018).

3.3.2 Thesis 2.2

A FAEKF structure has been derived, which incorporates both an EKF operating on quaternion-based orientation propagation and a sophisticated fuzzy inference machine. In this structure, the fuzzy inference system forms the relationship between the external disturbance (external acceleration, magnetic perturbation and vibration) magnitudes and EKF parameters and consistently modifies the noise variance values based on the instantaneous system dynamics. The developed adaptive structure effectively suppresses the effects of external disturbances, thereby enabling the FAEKF to provide reliable attitude estimation results, even in extreme dynamic and/or perturbed situations.

Publication pertaining to the thesis: Odry *et al.* (2020b).

Remark: The byproduct of these theses is a free-to-use ROS package I developed during my research work. This package enables both the generation of MARG-based measurements and the testing of different filter performances. I made this ROS package (which includes the developed test bench properties, URDF files, applied effort controllers, Gazebo configuration files and MATLAB scripts for the generation of artificial magnetic perturbation) publicly available in the supplementary online material Odry (2019a), with the aim of helping other laboratory teams with both performing and developing similar experiments. The complete project along with the software tools have been developed by the author of this PhD dissertation.

4 Conclusion

This research work addressed the enhancement of the closed loop performance of control systems and presented novel soft computing-based solutions to 1) improve the performance of control algorithms implemented for the stabilization of dynamical systems and 2) provide accurate and robust state estimation results even if variable, dynamic-dependent operating system conditions are present. The problems were both examined and validated on an unstable underactuated mechatronic system, i.e., a real WMP robot prototype enabled to embed, test and validate the developed techniques.

Chapter 2 described the elaboration and optimization procedures of linear and fuzzy control techniques for the unstable WMP robot. The obtained results highlighted that the developed fuzzy control structure enabled to achieve satisfying overall control quality with both fast closed loop behavior and small current peaks and jerks in the driving mechanism of the plant. The benchmark against the equivalent, linear counterpart control structure indicated that the flexibility of the proposed protective fuzzy technique allowed it to compete and even outperform the benchmark controller. As a result, the developed fuzzy-based technique represents a novel heuristic-type technique to provide satisfying reference tracking to robots and simultaneously protect the electro-mechanical parts against jerks and vibrations along with smaller energy consumption transients. Section 2.1 derived the nonlinear mathematical model of the plant and validated its applicability in control system design via implementation and measurement results of the real closed-loop dynamics. Section 2.2 reviewed the LQG control approach first and described the complete elaboration of the linear control strategy for the stabilization of the plant (subsection 2.2.1). Then, the fuzzy control method was discussed in subsection 2.2.2 and a cascade-connected fuzzy control scheme was established. Finally, the control structures were implemented and the initial, heuristically derived closed-loop performances were evaluated using both time-domain analysis and different error integrals (subsection 2.2.3). Both control structures stabilized the system, however the controllers were designed and tuned empirically (in case of the linear approach the Q and R matrices were selected heuristically, while in case of the fuzzy approach the membership function parameters and input-output ranges were defined based on human common sense). Therefore, the control performances were further improved by capitalizing on the linguistic-based flexibility of fuzzy logic, moreover, numerical optimization was employed for performance maximization. Namely, section 2.3 analyzed the enhancement of the achieved initial control performances. First, a protective fuzzy control strategy was developed in subsection 2.3.1 where the instantaneous motor currents were also considered in control action calculation via heuristic IF-THEN rules. Then, both the linear and fuzzy control structures were employed in an optimization environment, where a complex fitness function was formulated for control quality analysis and PSO-based minimization resulted in the optimal possible controller parameters (subsection 2.3.3). Based on the comparison, the achieved (maximized) control performances were analyzed and the characteristics of control techniques were discussed in subsection 2.3.4.

Chapter 3 presented novel solutions for low-cost MEMS-IMU and MEMS-MARG based attitude estimation. First, a test bench was introduced that both allows simulations of various system behaviors and measures the true system states along with the MEMS sensor data. Based on the collected measurements, the optimization of KF parameters was elaborated. Moreover, an adaptive fuzzy-logic based KF was developed in which the filter parameters were modified in real time based on the system dynamics. Two measurement approaches were employed for determining the magnitudes of the external acceleration and vibrations and a fuzzy inference machine was designed to modify the filter parameters as a function of these measures. Experiments demonstrated the efficacy of the proposed approaches for one-dimensional attitude estimation. Then, the developed techniques were generalized for three-dimensional attitude estimation, and a result, a novel quaternion-based fuzzy-adaptive EKF (FAEKF) was established. This filter structure both employed three new measurement techniques for the determination of instantaneous acceleration, vibration and magnetic perturbation magnitudes and a heuristic fuzzy inference machine to tune the noise covariances in real time. A special test environment was created for filter performance evaluation, in which a 6 DOF test bench executed various system (vibrating, accelerating) behaviors and simple algorithms generated magnetic perturbations artificially. The experimental results showed that the developed FAEKF improved the overall filter convergence significantly both in static and extremely vibrating and accelerating environments, thereby demonstrating its efficacy as an accurate and robust attitude filter. Subsection 3.1.1 introduced mathematical models related to MEMS IMU measurements and formulated a two-dimensional KF. Namely, subsection 3.1.2 described the designed test environment in which measurements can be collected under various dynamic conditions. In subsection 3.1.3, I discussed the procedure for optimizing the KF noise covariance values, while subsection 3.1.4 described methods for measuring external disturbances and elaborated on the adaptive KF approach. In subsection 3.1.5, the filter performances were compared against other common orientation estimation methods. The generalization of the techniques started with subsection 3.2.1, where an introduction to quaternion representation was given and the important relationships were highlighted. In subsection 3.2.2, the stochastic models of MARG sensor arrays were discussed and a suitable EKF formulation for attitude estimation was described. Subsection 3.2.3 presented the fuzzy adaptive strategy for MARG systems in detail, in which external disturbance magnitudes were measured with three novel methods; additionally, a sophisticated fuzzy inference machine was employed to manipulate the noise variances consistently. Subsection 3.2.4 introduced the 6 DOF test bench which was designed for estimation quality evaluation, the optimization-aided tuning of filter parameters, and the experimental results of the proposed approaches.

Future work may include multiple development directions. The derived nonlinear mathematical model of WMPs provides a compact, state space-based simulation environment and forms the basis for the analyses of both robustness and stability issues of different control strategies. The included nonlinear mechanical effects allow the developer to predict system behaviors even outside of the equilibrium points. Although the model responses showed realistic system behaviors, discrepancies could be observed between the measured system dynamics and simulation outputs. These discrepancies are related to the fact that nominal and derived model

parameters (e.g., inertia, mass, impedance and friction) were utilized during the numerical simulations. Therefore, a model validation process for WMPs can be a potential improvement in future studies in which both the robot parameters are identified and the derived model is qualified for multiple closed-loop scenarios. The developed protective-type fuzzy control strategy along with its LUT-based implementation represent a novel heuristic-type technique to provide satisfying reference tracking with smaller energy consumption transients. The proposed approach can be universally applied in such mechatronic systems (robots), where it is required to supply smooth control and thereby protecting the electro-mechanical parts effectively against jerks and vibrations. The presented filter structures provide accurate state estimation both in static and extreme dynamic conditions, therefore the algorithms can be beneficially applied in the closed-loop architecture of agile dynamic systems. The inference machine of these adaptive algorithms has been set up heuristically, therefore the optimization-based tuning of the fuzzy system (e.g., input-output ranges and membership functions) can be a potential improvement to achieve maximized filter performance. Additionally, the augmentation of the employed state space model can bring further advantages in state estimation, where the instantaneous external acceleration is both identified and incorporated in the state propagation. The presented test bench highly fosters the effective development of MARG-based algorithms, however only its ROS-based implementation is available in the supplementary online material. Since MATLAB forms the backbone of algorithm development processes in engineering applications, therefore it is also planned to elaborate the MATLAB-based realization of the proposed 6-DOF test environment, with the aim to provide a universal platform for the effective development of MARG-based techniques.

Bibliography

Aggarwal, P. (2010). *MEMS-based integrated navigation*. Artech House.

Ahmad, I., El Hadri, A., Benziane, L., and Benallegue, A. (2019). Globally asymptotic attitude estimation for accelerated aerial vehicles. *Aerospace Science and Technology*, **84**, 1175–1181.

Ahmed, K., Yahaya, N., Asirvadam, V., Ramani, K., and Ibrahim, O. (2016). Comparison of fuzzy logic control and pi control for a three-level rectifier based on voltage oriented control. In *2016 IEEE International Conference on Power and Energy (PECon)*, pages 127–132. IEEE.

Al Mansour, M., Chouaib, I., Jafar, A., and Potapov, A. (2019). Analytical algorithm for attitude and heading estimation aided by maneuver classification. *Gyroscopy and Navigation*, **10**(2), 77–89.

Al-Younes, Y. M., Al-Jarrah, M. A., and Jhemi, A. A. (2010). Linear vs. nonlinear control techniques for a quadrotor vehicle. In *7th International Symposium on Mechatronics and its Applications*, pages 1–10. IEEE.

Alfi, A. and Fateh, M.-M. (2011). Intelligent identification and control using improved fuzzy particle swarm optimization. *Expert Systems with Applications*, **38**(10), 12312–12317.

Alıcı, G., Jagielski, R., Şekercioğlu, Y. A., and Shirinzadeh, B. (2006). Prediction of geometric errors of robot manipulators with particle swarm optimisation method. *Robotics and Autonomous Systems*, **54**(12), 956–966.

Alireza, A. (2011). Pso with adaptive mutation and inertia weight and its application in parameter estimation of dynamic systems. *Acta Automatica Sinica*, **37**(5), 541–549.

AN3182 (2010). Tilt measurement using a low-g 3-axis accelerometer. *ST Microelectronics*.

Anisimov, D., Dang, T. S., *et al.* (2018). Development of a microcontroller-based adaptive fuzzy controller for a two-wheeled self-balancing robot. *Microsystem Technologies*, **24**(9), 3677–3687.

Araar, O. and Aouf, N. (2014). Full linear control of a quadrotor uav, lq vs hinf. In *2014 UKACC International Conference on Control (CONTROL)*, pages 133–138. IEEE.

Assad, A., Khalaf, W., and Chouaib, I. (2019). Novel adaptive fuzzy extended kalman filter for attitude estimation in gps-denied environment. *Gyroscopy and Navigation*, **10**(3), 131–146.

Baldi, T. L., Farina, F., Garulli, A., Giannitrapani, A., and Prattichizzo, D. (2019). Upper body pose estimation using wearable inertial sensors and multiplicative kalman filter. *IEEE Sensors Journal*.

Barton, G. (1996). Process control: Designing processes and control systems for dynamic performance: by thomas e. marlin (mcgraw-hill, new york, 1995, isbn 0-07-040491-7, pp 954+ xxii).

Battiston, A., Sharf, I., and Nahon, M. (2019). Attitude estimation for collision recovery of a quadcopter unmanned aerial vehicle. *The International Journal of Robotics Research*, **38**(10-11), 1286–1306.

Benini, A., Senatore, R., D'Angelo, F., Orsini, D., Quatraro, E., Verola, M., and Pizzarulli, A. (2015). A closed-loop procedure for the modeling and tuning of kalman filter for fog ins. In *Inertial Sensors and Systems Symposium (ISS), 2015 DGON*, pages 1–19. IEEE.

Bloch, A. M. (2003). Nonholonomic mechanics. In *Nonholonomic mechanics and control*, pages 207–276. Springer.

Borbás, K., Kiss, T., Klincsik, M., Kvasznicza, Z., Máthé, K., Vér, C., Vizvári, Z., and Odry, P. (2018). Process and measuring system for data acquisition and processing in soft-tomography studies. US Patent App. 16/062,319.

Bouabdallah, S., Noth, A., and Siegwart, R. (2004). Pid vs lq control techniques applied to an indoor micro quadrotor. In *2004 IEEE/RSJ International Conference on Intelligent Robots and Systems (IROS)(IEEE Cat. No. 04CH37566)*, volume 3, pages 2451–2456. IEEE.

Carbone, G. (2011). Stiffness analysis and experimental validation of robotic systems. *Frontiers of Mechanical Engineering*, **6**(2), 182–196.

Cavallo, A., Cirillo, A., Cirillo, P., De Maria, G., Falco, P., Natale, C., and Pirozzi, S. (2014). Experimental comparison of sensor fusion algorithms for attitude estimation. *IFAC Proceedings Volumes*, **47**(3), 7585–7591.

Cazzolato, B., Harvey, J., Dyer, C., Fulton, K., Schumann, E., Zhu, T., Prime, Z., Davis, B., Hart, S., Pearce, E., *et al.* (2011). Modeling, simulation and control of an electric diwheel. In *Australasian Conference on Robotics and Automation*, pages 1–10.

Chan, R. P. M., Stol, K. A., and Halkyard, C. R. (2013). Review of modelling and control of two-wheeled robots. *Annual Reviews in Control*, **37**(1), 89–103.

Chatterjee, A., Pulasinghe, K., Watanabe, K., and Izumi, K. (2005). A particle-swarm-optimized fuzzy-neural network for voice-controlled robot systems. *IEEE Transactions on Industrial Electronics*, **52**(6), 1478–1489.

Chiella, A. C., Teixeira, B. O., and Pereira, G. A. (2019). Quaternion-based robust attitude estimation using an adaptive unscented kalman filter. *Sensors*, **19**(10), 2372.

Code, G. (2013). Particle swarm toolbox for matlab (psomatlab). Available from: code.google.com.

Crassidis, J. L., Markley, F. L., and Cheng, Y. (2007). Survey of nonlinear attitude estimation methods. *Journal of guidance, control, and dynamics*, **30**(1), 12–28.

Csaba, G. and Vamossy, Z. (2012). Fuzzy based obstacle avoidance for mobil robots with kinect sensor. In *2012 4th IEEE International Symposium on Logistics and Industrial Informatics*, pages 135–144. IEEE.

Cui, R., Guo, J., and Mao, Z. (2015). Adaptive backstepping control of wheeled inverted pendulums models. *Nonlinear Dynamics*, **79**(1), 501–511.

Dai, F., Gao, X., Jiang, S., Guo, W., and Liu, Y. (2015). A two-wheeled inverted pendulum robot with friction compensation. *Mechatronics*, **30**, 116–125.

Das, T. and Kar, I. N. (2006). Design and implementation of an adaptive fuzzy logic-based controller for wheeled mobile robots. *IEEE Transactions on Control Systems Technology*, **14**(3), 501–510.

Diebel, J. (2006). Representing attitude: Euler angles, unit quaternions, and rotation vectors. *Matrix*, **58**(15-16), 1–35.

Divelbiss, A. W. and Wen, J. T. (1997). Trajectory tracking control of a car-trailer system. *IEEE Transactions on Control systems technology*, **5**(3), 269–278.

dos Santos Coelho, L. (2009). Tuning of pid controller for an automatic regulator voltage system using chaotic optimization approach. *Chaos, Solitons & Fractals*, **39**(4), 1504–1514.

Dubois, D. and Prade, H. (2015). The legacy of 50 years of fuzzy sets: A discussion. *Fuzzy Sets and Systems*, **281**, 21–31.

Duraffourg, C., Bonnet, X., Dauriac, B., and Pillet, H. (2019). Real time estimation of the pose of a lower limb prosthesis from a single shank mounted imu. *Sensors*, **19**(13), 2865.

El-Sheimy, N., Hou, H., and Niu, X. (2008). Analysis and modeling of inertial sensors using allan variance. *IEEE Transactions on instrumentation and measurement*, **57**(1), 140–149.

Euston, M., Coote, P., Mahony, R., Kim, J., and Hamel, T. (2008). A complementary filter for attitude estimation of a fixed-wing uav. In *Intelligent Robots and Systems, 2008. IROS 2008. IEEE/RSJ International Conference on*, pages 340–345. IEEE.

Fan, B., Li, Q., and Liu, T. (2018). Improving the accuracy of wearable sensor orientation using a two-step complementary filter with state machine-based adaptive strategy. *Measurement Science and Technology*, **29**(11), 115104.

Feng, K., Li, J., Zhang, X., Shen, C., Bi, Y., Zheng, T., and Liu, J. (2017). A new quaternion-based kalman filter for real-time attitude estimation using the two-step geometrically-intuitive correction algorithm. *Sensors*, **17**(9), 2146.

Fourati, H., Manamanni, N., Afilal, L., and Handrich, Y. (2010). A nonlinear filtering approach for the attitude and dynamic body acceleration estimation based on inertial and magnetic sensors: Bio-logging application. *IEEE sensors journal*, **11**(1), 233–244.

Franklin, G. F., Powell, J. D., Emami-Naeini, A., and Powell, J. D. (1994). *Feedback control of dynamic systems*, volume 3. Addison-Wesley Reading, MA.

Fukuda, T. and Kubota, N. (1999). An intelligent robotic system based on a fuzzy approach. *Proceedings of the IEEE*, **87**(9), 1448–1470.

Fullér, R. (2000). *Introduction to neuro-fuzzy systems*, volume 2. Springer Science & Business Media.

Furrer, F., Burri, M., Achtelik, M., and Siegwart, R. (2016). Robot operating system (ros): The complete reference (volume 1). *Cham: Springer International Publishing*, pages 595–625.

Ghaffari, A., Shariati, A., and Shamekhi, A. H. (2016). A modified dynamical formulation for two-wheeled self-balancing robots. *Nonlinear Dynamics*, **83**(1-2), 217–230.

Gośliński, J., Nowicki, M., and Skrzypczyński, P. (2015). Performance comparison of ekf-based algorithms for orientation estimation on android platform. *IEEE Sensors Journal*, **15**(7), 3781–3792.

Grasser, F., D'arrigo, A., Colombi, S., and Rufer, A. C. (2002). Joe: a mobile, inverted pendulum. *IEEE Transactions on industrial electronics*, **49**(1), 107–114.

Guo, Z.-Q., Xu, J.-X., and Lee, T. H. (2014). Design and implementation of a new sliding mode controller on an underactuated wheeled inverted pendulum. *Journal of the Franklin Institute*, **351**(4), 2261–2282.

Habbachi, S., Sayadi, M., Fnaiech, F., Rezzoug, N., Gorce, P., and Benbouzid, M. (2018). Estimation of imu orientation using linear kalman filter based on correntropy criterion. In *IEEE International Conference on Industrial Technology (ICIT)*, pages 1340–1344. IEEE.

Hendrix, E. M. and Boglárka, G. (2010). *Introduction to nonlinear and global optimization*. Springer New York.

Ho, W. K., Hang, C. C., and Cao, L. S. (1995). Tuning of pid controllers based on gain and phase margin specifications. *Automatica*, **31**(3), 497–502.

Höflinger, F., Müller, J., Zhang, R., Reindl, L. M., and Burgard, W. (2013). A wireless micro inertial measurement unit (imu). *IEEE Transactions on Instrumentation and Measurement*, **62**(9), 2583–2595.

Hou, Z.-G., Zou, A.-M., Cheng, L., and Tan, M. (2009). Adaptive control of an electrically driven nonholonomic mobile robot via backstepping and fuzzy approach. *IEEE Transactions on Control Systems Technology*, **17**(4), 803–815.

Huang, C.-H., Wang, W.-J., and Chiu, C.-H. (2011). Design and implementation of fuzzy control on a two-wheel inverted pendulum. *IEEE Transactions on Industrial Electronics*, **58**(7), 2988–3001.

Jeong, S. and Takahashi, T. (2007). Wheeled inverted pendulum type assistant robot: inverted mobile, standing, and sitting motions. In *2007 IEEE/RSJ International Conference on Intelligent Robots and Systems*, pages 1932–1937. IEEE.

Jeong, S. and Takahashi, T. (2008). Wheeled inverted pendulum type assistant robot: design concept and mobile control. *Intelligent Service Robotics*, **1**(4), 313–320.

Ji, J.-K. and Sul, S.-K. (1995). Kalman filter and lq based speed controller for torsional vibration suppression in a 2-mass motor drive system. *IEEE Transactions on industrial electronics*, **42**(6), 564–571.

Jouybari, A., Amiri, H., Ardalan, A. A., and Zahraee, N. K. (2019). Methods comparison for attitude determination of a lightweight buoy by raw data of imu. *Measurement*, **135**, 348–354.

Kang, D., Jang, C., and Park, F. C. (2019). Unscented kalman filtering for simultaneous estimation of attitude and gyroscope bias. *IEEE/ASME Transactions on Mechatronics*, **24**(1), 350–360.

Kazimierski, W. and Łubczonek, J. (2012). Verification of marine multiple model neural tracking filter for the needs of shore radar stations. In *2012 13th International Radar Symposium*, pages 554–559. IEEE.

Kecskés, I. and Odry, P. (2014). Optimization of pi and fuzzy-pi controllers on simulation model of szabad (ka)-ii walking robot. *International Journal of Advanced Robotic Systems*, **11**(11), 186.

Kecskés, I. and Odry, P. (2018). Multi-scenario multi-objective optimization of a fuzzy motor controller for the szabad (ka)-ii hexapod robot. *Acta Polytechnica Hungarica*, **15**(7).

Kecskés, I., Burkus, E., Király, Z., Odry, Á., and Odry, P. (2017a). Competition of motor controllers using a simplified robot leg: Pid vs fuzzy logic. In *2017 Fourth International Conference on Mathematics and Computers in Sciences and in Industry (MCSI)*, pages 37–43. IEEE.

Kecskés, I., Burkus, E., Bazsó, F., and Odry, P. (2017b). Model validation of a hexapod walker robot. *Robotica*, **35**(2), 419—-462.

Kennedy, J. F., Kennedy, J., Eberhart, R. C., and Shi, Y. (2001). *Swarm intelligence*. Morgan Kaufmann.

Khankalantary, S., Rafatnia, S., and Mohammadkhani, H. (2019). An adaptive constrained type-2 fuzzy hammerstein neural network data fusion scheme for low-cost sins/gnss navigation system. *Applied Soft Computing*, page 105917.

Kim, Y., Kim, S., and Kwak, Y. (2006). Improving driving ability for a two-wheeled inverted-pendulum-type autonomous vehicle. *Proceedings of the Institution of Mechanical Engineers, Part D: Journal of Automobile Engineering*, **220**(2), 165–175.

Kóczy, L. T., Tikk, D., *et al.* (2000). Fuzzy rendszerek. *TypoTEX, Budapest*.

Koenig, N. and Howard, A. (2004). Design and use paradigms for gazebo, an open-source multi-robot simulator. In *2004 IEEE/RSJ International Conference on Intelligent Robots and Systems (IROS)(IEEE Cat. No. 04CH37566)*, volume 3, pages 2149–2154. IEEE.

Kok, M., Hol, J. D., Schön, T. B., Gustafsson, F., and Luinge, H. (2012). Calibration of a magnetometer in combination with inertial sensors. In *2012 15th International Conference on Information Fusion*, pages 787–793. IEEE.

Korniyenko, O. V., Sharawi, M. S., and Aloi, D. N. (2005). Neural network based approach for tuning kalman filter. In *Electro Information Technology, 2005 IEEE International Conference on*, pages 1–5. IEEE.

Koubâa, A. (2017). *Robot Operating System (ROS)*. Springer.

Kownacki, C. (2011). Optimization approach to adapt kalman filters for the real-time application of accelerometer and gyroscope signals' filtering. *Digital Signal Processing*, **21**(1), 131–140.

Kuipers, J. B. *et al.* (1999). *Quaternions and rotation sequences*, volume 66. Princeton university press Princeton.

Kulikov, G. Y. and Kulikova, M. (2018). Estimation of maneuvering target in the presence of non-gaussian noise: A coordinated turn case study. *Signal Processing*, **145**, 241–257.

Kumar, N., Takács, M., and Vámossy, Z. (2017). Robot navigation in unknown environment using fuzzy logic. In *2017 IEEE 15th International Symposium on Applied Machine Intelligence and Informatics (SAMI)*, pages 000279–000284. IEEE.

Kumon, M., Udo, Y., Michihira, H., Nagata, M., Mizumoto, I., and Iwai, Z. (2006). Autopilot system for kiteplane. *IEEE/ASME Transactions on Mechatronics*, **11**(5), 615–624.

Kwok, N., Ha, Q., Nguyen, T., Li, J., and Samali, B. (2006). A novel hysteretic model for magnetorheological fluid dampers and parameter identification using particle swarm optimization. *Sensors and Actuators A: Physical*, **132**(2), 441–451.

Lantos, B. (2001). Irányítási rendszerek elmélete és tervezése i. *Egyváltozós szabályozások. Akadémia kiadó, Budapest*.

Lee, C. and Gonzalez, R. (2008). Fuzzy logic versus a pid controller for position control of a muscle-like actuated arm. *Journal of Mechanical Science and Technology*, **22**(8), 1475–1482.

Lee, H. and Jung, S. (2012). Balancing and navigation control of a mobile inverted pendulum robot using sensor fusion of low cost sensors. *Mechatronics*, **22**(1), 95–105.

Lee, J. K., Park, E. J., and Robinovitch, S. N. (2012). Estimation of attitude and external acceleration using inertial sensor measurement during various dynamic conditions. *IEEE transactions on instrumentation and measurement*, **61**(8), 2262–2273.

Li, W. and Wang, J. (2013). Effective adaptive kalman filter for mems-imu/magnetometers integrated attitude and heading reference systems. *Journal of Navigation*, **66**(01), 99–113.

Li, Y.-b., Liu, W.-z., and Song, Q. (2011). Improved lqg control for small unmanned helicopter based on active model in uncertain environment. In *2011 International Conference on Electronics, Communications and Control (ICECC)*, pages 289–292. IEEE.

Li, Z., Yang, C., and Fan, L. (2012). *Advanced control of wheeled inverted pendulum systems*. Springer Science & Business Media.

Ligorio, G. and Sabatini, A. M. (2015). A novel kalman filter for human motion tracking with an inertial-based dynamic inclinometer. *IEEE Transactions on Biomedical Engineering*, **62**(8), 2033–2043.

Lilienkamp, K. A. (2003). *Lab experiences for teaching undergraduate dynamics*. Ph.D. thesis, Massachusetts Institute of Technology.

Liu, F., Li, J., Wang, H., and Liu, C. (2014). An improved quaternion gauss–newton algorithm for attitude determination using magnetometer and accelerometer. *Chinese Journal of aeronautics*, **27**(4), 986–993.

Liu, S., Lyu, P., Lai, J., Yuan, C., and Wang, B. (2019). A fault-tolerant attitude estimation method for quadrotors based on analytical redundancy. *Aerospace Science and Technology*, **93**, 105290.

López-Guauque, J. A. and Gil-Lafuente, A. M. (2020). Fifty years of fuzzy research: A bibliometric analysis and a long-term comparative overview. *Journal of Intelligent and Fuzzy Systems*, **Preprint**(Preprint), 1–13.

Madgwick, S. (2010). An efficient orientation filter for inertial and inertial/magnetic sensor arrays. *Report x-io and University of Bristol (UK)*, **25**.

Madgwick, S. O., Harrison, A. J., and Vaidyanathan, R. (2011). Estimation of imu and marg orientation using a gradient descent algorithm. In *Rehabilitation Robotics (ICORR), 2011 IEEE International Conference on*, pages 1–7. IEEE.

Mahony, R., Hamel, T., and Pflimlin, J.-M. (2008). Nonlinear complementary filters on the special orthogonal group. *IEEE Transactions on automatic control*, **53**(5), 1203–1218.

Makni, A., Fourati, H., and Kibangou, A. Y. (2015). Energy-aware adaptive attitude estimation under external acceleration for pedestrian navigation. *IEEE/ASME Transactions On Mechatronics*, **21**(3), 1366–1375.

Markley, F. L. and Crassidis, J. L. (2014). *Fundamentals of spacecraft attitude determination and control*, volume 33. Springer.

Marple, L. (1999). Computing the discrete-time" analytic" signal via fft. *IEEE Transactions on signal processing*, **47**(9), 2600–2603.

Márton, L., Hodel, A. S., Lantos, B., and Hung, J. Y. (2008). Underactuated robot control: comparing lqr, subspace stabilization, and combined error metric approaches. *IEEE Transactions on Industrial Electronics*, **55**(10), 3724–3730.

Maruki, Y., Kawano, K., Suemitsu, H., and Matsuo, T. (2014). Adaptive backstepping control of wheeled inverted pendulum with velocity estimator. *International Journal of Control, Automation and Systems*, **12**(5), 1040–1048.

Mazza, C., Donati, M., McCamley, J., Picerno, P., and Cappozzo, A. (2012). An optimized kalman filter for the estimate of trunk orientation from inertial sensors data during treadmill walking. *Gait & posture*, **35**(1), 138–142.

McLean, D. and Matsuda, H. (1998). Helicopter station-keeping: comparing lqr, fuzzy-logic and neural-net controllers. *Engineering Applications of Artificial Intelligence*, **11**(3), 411–418.

Meyer, J., Sendobry, A., Kohlbrecher, S., Klingauf, U., and Von Stryk, O. (2012). Comprehensive simulation of quadrotor uavs using ros and gazebo. In *International conference on simulation, modeling, and programming for autonomous robots*, pages 400–411. Springer.

Michel, T., Genevès, P., Fourati, H., and Layaïda, N. (2018). Attitude estimation for indoor navigation and augmented reality with smartphones. *Pervasive and Mobile Computing*, **46**, 96–121.

Modares, H., Alfi, A., and Sistani, M.-B. N. (2010a). Parameter estimation of bilinear systems based on an adaptive particle swarm optimization. *Engineering Applications of Artificial Intelligence*, **23**(7), 1105–1111.

Modares, H., Alfi, A., and Fateh, M.-M. (2010b). Parameter identification of chaotic dynamic systems through an improved particle swarm optimization. *Expert Systems with Applications*, **37**(5), 3714–3720.

Mourcou, Q., Fleury, A., Franco, C., Klopcic, F., and Vuillerme, N. (2015). Performance evaluation of smartphone inertial sensors measurement for range of motion. *Sensors*, **15**(9), 23168–23187.

Nagarajan, U. (2012). *Fast and graceful balancing mobile robots*. Ph.D. thesis, Carnegie Mellon University.

Nagaya, S., Morikawa, T., Takami, I., and Chen, G. (2013). Robust lq control for parallel wheeled inverted pendulum. In *2013 Australian Control Conference*, pages 189–194. IEEE.

Nasir, A., Ahmad, M., and Ismail, R. R. (2010). The control of a highly nonlinear two-wheels balancing robot: A comparative assessment between lqr and pid-pid control schemes. *World Academy of Science, Engineering and Technology*, **70**, 227–232.

National, I. (2018). Labview help: Fuzzy controllers. Available from: http://zone.ni.com/reference/en-XX/help/371361R-01/lvpidmain/fuzzy-controllers/.

Nourmohammadi, H. and Keighobadi, J. (2018). Fuzzy adaptive integration scheme for low-cost sins/gps navigation system. *Mechanical Systems and Signal Processing*, **99**, 434–449.

Nowicki, M., Wietrzykowski, J., and Skrzypczyński, P. (2015). Simplicity or flexibility? complementary filter vs. ekf for orientation estimation on mobile devices. In *Cybernetics (CYBCONF), 2015 IEEE 2nd International Conference on*, pages 166–171. IEEE.

Odry, Á. (2019a). Fuzzy-adaptive Extended Kalman filter supplementary material. Available from: http://appl-dsp.com/faekf/.

Odry, Á. (2019b). Self-balancing robot supplementary material. Available from: http://appl-dsp.com/self-balancing-robot-kit/.

Odry, Á. (2019c). Two-wheeled mobile pendulum system supplementary material. Available from: http://appl-dsp.com/lqg-and-fuzzy-control-of-a-mobile-wheeled-pendulum/.

Odry, À. and Fullér, R. (2018). Comparison of optimized pid and fuzzy control strategies on a mobile pendulum robot. In *2018 IEEE 12th International Symposium on Applied Computational Intelligence and Informatics (SACI)*, pages 207–212. IEEE.

Odry, Á., Harmati, I., Király, Z., and Odry, P. (2015a). Design, realization and modeling of a two-wheeled mobile pendulum system. *14th International Conference on Instrumentation, Measurement, Circuits and Systems (IMCAS '15)*, pages 75–79.

Odry, Á., Burkus, E., and Odry, P. (2015b). Lqg control of a two-wheeled mobile pendulum system. *The Fourth International Conference on Intelligent Systems and Applications (INTELLI 2015)*, pages 105–112.

Odry, Á., Burkus, E., Kecskés, I., Fodor, J., and Odry, P. (2016a). Fuzzy control of a two-wheeled mobile pendulum system. In *Applied Computational Intelligence and Informatics (SACI), 2016 IEEE 11th International Symposium on*, pages 99–104. IEEE.

Odry, Á., Fodor, J., and Odry, P. (2016b). Stabilization of a two-wheeled mobile pendulum system using lqg and fuzzy control techniques. *International Journal On Advances in Intelligent Systems*, **9**(1,2), 223–232.

Odry, Á., Kecskes, I., Burkus, E., Kiraly, Z., and Odry, P. (2017a). Optimized fuzzy control of a two-wheeled mobile pendulum system. *International Journal of Control Systems and Robotics*, **2**, 73–79.

Odry, Á., Kecskés, I., Burkus, E., and Odry, P. (2017b). Protective fuzzy control of a two-wheeled mobile pendulum robot: Design and optimization. *WSEAS Transactions on Systems and Control*, **12**, 297–306.

Odry, Á., Fullér, R., Rudas, I. J., and Odry, P. (2018). Kalman filter for mobile-robot attitude estimation: Novel optimized and adaptive solutions. *Mechanical systems and signal processing*, **110**, 569–589.

Odry, Á., Fullér, R., Rudas, I. J., and Odry, P. (2020a). Fuzzy control of self-balancing robots: A control laboratory project. *Computer Applications in Engineering Education*, pages 1–24.

Odry, Á., Kecskes, I., Sarcevic, P., Vizvari, Z., Toth, A., and Odry, P. (2020b). A novel fuzzy-adaptive extended kalman filter for real-time attitude estimation of mobile robots. *Sensors*, **20**(3), 803.

Oh, S.-K., Jang, H.-J., and Pedrycz, W. (2011). A comparative experimental study of type-1/type-2 fuzzy cascade controller based on genetic algorithms and particle swarm optimization. *Expert Systems with Applications*, **38**(9), 11217–11229.

Papafotis, K. and Sotiriadis, P. P. (2019). Mag. ic al.–a unified methodology for magnetic and inertial sensors calibration and alignment. *IEEE Sensors Journal*.

Pathak, K., Franch, J., and Agrawal, S. K. (2005). Velocity and position control of a wheeled inverted pendulum by partial feedback linearization. *IEEE Transactions on robotics*, **21**(3), 505–513.

Powell, T. D. (2002). Automated tuning of an extended kalman filter using the downhill simplex algorithm. *Journal of Guidance, Control, and Dynamics*, **25**(5), 901–908.

Prasad, L. B., Tyagi, B., and Gupta, H. O. (2014). Optimal control of nonlinear inverted pendulum system using pid controller and lqr: performance analysis without and with disturbance input. *International Journal of Automation and Computing*, **11**(6), 661–670.

Quaranta, G., Monti, G., and Marano, G. C. (2010). Parameters identification of van der pol–duffing oscillators via particle swarm optimization and differential evolution. *Mechanical Systems and Signal Processing*, **24**(7), 2076–2095.

Quigley, M., Gerkey, B., and Smart, W. D. (2015). *Programming Robots with ROS: a practical introduction to the Robot Operating System*. " O'Reilly Media, Inc.".

Raffo, G. V., Ortega, M. G., Madero, V., and Rubio, F. R. (2015). Two-wheeled self-balanced pendulum workspace improvement via underactuated robust nonlinear control. *Control Engineering Practice*, **44**, 231–242.

Roh, M.-S. and Kang, B.-S. (2018). Dynamic accuracy improvement of a mems ahrs for small uavs. *International Journal of Precision Engineering and Manufacturing*, **19**(10), 1457–1466.

Ruck, M., Herreros, I., Maffei, G., Sánchez-Fibla, M., and Verschure, P. (2016). Learning to balance while reaching: A cerebellar-based control architecture for a self-balancing robot. In *Conference on Biomimetic and Biohybrid Systems*, pages 214–226. Springer.

Sabatini, A. M. (2006). Quaternion-based extended kalman filter for determining orientation by inertial and magnetic sensing. *IEEE Transactions on Biomedical Engineering*, **53**(7), 1346–1356.

Sabatini, A. M. (2011). Kalman-filter-based orientation determination using inertial/magnetic sensors: Observability analysis and performance evaluation. *Sensors*, **11**(10), 9182–9206.

Salerno, A. and Angeles, J. (2003). On the nonlinear controllability of a quasiholonomic mobile robot. In *2003 IEEE International Conference on Robotics and Automation (Cat. No. 03CH37422)*, volume 3, pages 3379–3384. IEEE.

Salerno, A. and Angeles, J. (2007). A new family of two-wheeled mobile robots: Modeling and controllability. *IEEE Transactions on Robotics*, **23**(1), 169–173.

Salvatore, N., Caponio, A., Neri, F., Stasi, S., and Cascella, G. L. (2010). Optimization of delayed-state kalman-filter-based algorithm via differential evolution for sensorless control of induction motors. *IEEE Transactions on Industrial Electronics*, **57**(1), 385–394.

Santos, M., Lopez, V., and Morata, F. (2010). Intelligent fuzzy controller of a quadrotor. In *2010 IEEE international conference on intelligent systems and knowledge engineering*, pages 141–146. IEEE.

Sarcevic, P. and Pletl, S. (2018). False detection filtering method for magnetic sensor-based vehicle detection systems. In *2018 IEEE 16th International Symposium on Intelligent Systems and Informatics (SISY)*, pages 000277–000282. IEEE.

Sarcevic, P., Kincses, Z., and Pletl, S. (2019). Online human movement classification using wrist-worn wireless sensors. *Journal of Ambient Intelligence and Humanized Computing*, **10**(1), 89–106.

Sciavicco, L. and Siciliano, B. (2012). *Modelling and control of robot manipulators*. Springer Science & Business Media.

Segway (2020). Segway personal transporter. Available from: http://www.segway.com/.

Shao, Z. and Liu, D. (2010). Balancing control of a unicycle riding. In *Proceedings of the 29th Chinese Control Conference*, pages 3250–3254. IEEE.

Shi, K., Chan, T., Wong, Y., and Ho, S. (2002). Speed estimation of an induction motor drive using an optimized extended kalman filter. *IEEE Transactions on Industrial Electronics*, **49**(1), 124–133.

Shomin, M. (2016). *Navigation and physical interaction with balancing robots*. Ph.D. thesis, Carnegie Mellon University.

Shuster, M. D. and Oh, S. D. (1981). Three-axis attitude determination from vector observations. *Journal of guidance and Control*, **4**(1), 70–77.

Stateczny, A. (2001). Neural manoeuvre detection of the tracked target in arpa systems. *IFAC Proceedings Volumes*, **34**(7), 209–214.

Stateczny, A. and Kazimierski, W. (2008). A comparison of the target tracking in marine navigational radars by means of grnn filter and numerical filter. In *2008 IEEE Radar Conference*, pages 1–4. IEEE.

Sun, J. and Li, Z. (2015). Development and implementation of a wheeled inverted pendulum vehicle using adaptive neural control with extreme learning machines. *Cognitive Computation*, **7**(6), 740–752.

Tamir, D. E., Rishe, N. D., and Kandel, A. (2015). *Fifty years of fuzzy logic and its applications*, volume 326. Springer.

Tang, K.-S., Man, K. F., Chen, G., and Kwong, S. (2001). An optimal fuzzy pid controller. *IEEE transactions on industrial electronics*, **48**(4), 757–765.

Tian, Y., Wei, H., and Tan, J. (2012). An adaptive-gain complementary filter for real-time human motion tracking with marg sensors in free-living environments. *IEEE Transactions on Neural Systems and Rehabilitation Engineering*, **21**(2), 254–264.

Tsagarakis, N. G., Caldwell, D. G., Negrello, F., Choi, W., Baccelliere, L., Loc, V., Noorden, J., Muratore, L., Margan, A., Cardellino, A., *et al.* (2017). Walk-man: A high-performance humanoid platform for realistic environments. *Journal of Field Robotics*, **34**(7), 1225–1259.

Valenti, R. G., Dryanovski, I., and Xiao, J. (2015). Keeping a good attitude: A quaternion-based orientation filter for imus and margs. *Sensors*, **15**(8), 19302–19330.

Vasudevan, H., Dollar, A. M., and Morrell, J. B. (2015). Design for control of wheeled inverted pendulum platforms. *Journal of Mechanisms and Robotics*, **7**(4), 041005.

Verbruggen, H. B. and Bruijn, P. (1997). Fuzzy control and conventional control: What is (and can be) the real contribution of fuzzy systems? *Fuzzy sets and Systems*, **90**(2), 151–160.

Visioli, A. (2001). Optimal tuning of pid controllers for integral and unstable processes. *IEE Proceedings-Control Theory and Applications*, **148**(2), 180–184.

Wahba, G. (1965). A least squares estimate of satellite attitude. *SIAM review*, **7**(3), 409–409.

Wang, L.-X. (1997). A course in fuzzy systems and control, prentice-hall ptr. *Englewood Cliffs, NJ*.

Welch, G. and Bishop, G. (2001). An introduction to the kalman filter. Tech. rep. tr 95-041, Department of Computer Science, University of North Carolina, USA.

Wen, X., Liu, C., Huang, Z., Su, S., Guo, X., Zuo, Z., and Qu, H. (2019). A first-order differential data processing method for accuracy improvement of complementary filtering in micro-uav attitude estimation. *Sensors*, **19**(6), 1340.

Wilson, S., Eberle, H., Hayashi, Y., Madgwick, S. O., McGregor, A., Jing, X., and Vaidyanathan, R. (2019). Formulation of a new gradient descent marg orientation algorithm: Case study on robot teleoperation. *Mechanical Systems and Signal Processing*, **130**, 183–200.

Wu, J. (2019). Real-time magnetometer disturbance estimation via online nonlinear programming. *IEEE Sensors Journal*, **19**(12), 4405–4411.

Wu, J. and Shan, S. (2019). Dot product equality constrained attitude determination from two vector observations: Theory and astronautical applications. *Aerospace*, **6**(9), 102.

Wu, J., Zhou, Z., Chen, J., Fourati, H., and Li, R. (2016). Fast complementary filter for attitude estimation using low-cost marg sensors. *IEEE Sensors Journal*, **16**(18), 6997–7007.

Wu, J., Zhou, Z., Fourati, H., and Cheng, Y. (2018). A super fast attitude determination algorithm for consumer-level accelerometer and magnetometer. *IEEE Transactions on Consumer Electronics*, **64**(3), 375–381.

Wu, J., Zhou, Z., Fourati, H., Li, R., and Liu, M. (2019). Generalized linear quaternion complementary filter for attitude estimation from multisensor observations: An optimization approach. *IEEE Transactions on Automation Science and Engineering*.

Xi, L., Chen, B., Zhao, H., Qin, J., and Cao, J. (2017). Maximum correntropy kalman filter with state constraints. *IEEE Access*, **5**, 25846–25853.

Xiong, L., Xia, X., Lu, Y., Liu, W., Gao, L., Song, S., Han, Y., and Yu, Z. (2019). Imu-based automated vehicle slip angle and attitude estimation aided by vehicle dynamics. *Sensors*, **19**(8), 1930.

Xu, J.-X., Guo, Z.-Q., and Lee, T. H. (2013a). Design and implementation of a takagi–sugeno-type fuzzy logic controller on a two-wheeled mobile robot. *IEEE Transactions on Industrial Electronics*, **60**(12), 5717–5728.

Xu, J.-X., Guo, Z.-Q., and Lee, T. H. (2013b). Design and implementation of a takagi–sugeno-type fuzzy logic controller on a two-wheeled mobile robot. *IEEE Transactions on industrial electronics*, **60**(12), 5717–5728.

Xu, J.-X., Guo, Z.-Q., and Lee, T. H. (2014). Design and implementation of integral sliding-mode control on an underactuated two-wheeled mobile robot. *IEEE Transactions on Industrial Electronics*, **61**(7), 3671–3681.

Xu, Q., Stepan, G., and Wang, Z. (2015). Balancing a wheeled inverted pendulum with a single accelerometer in the presence of time delay. *Journal of Vibration and Control*, page 1077546315583400.

Yang, C., Li, Z., Cui, R., and Xu, B. (2014). Neural network-based motion control of an underactuated wheeled inverted pendulum model. *IEEE Transactions on Neural Networks and Learning Systems*, **25**(11), 2004–2016.

Ye, Y., Yin, C.-B., Gong, Y., and Zhou, J.-j. (2017). Position control of nonlinear hydraulic system using an improved pso based pid controller. *Mechanical Systems and Signal Processing*, **83**, 241–259.

Yoshida, K., Sekikawa, M., and Hosomi, K. (2016). Nonlinear analysis on purely mechanical stabilization of a wheeled inverted pendulum on a slope. *Nonlinear Dynamics*, **83**(1-2), 905–917.

Yuan, Q., Asadi, E., Lu, Q., Yang, G., and Chen, I.-M. (2019). Uncertainty-based imu orientation tracking algorithm for dynamic motions. *IEEE/ASME Transactions on Mechatronics*, **24**(2), 872–882.

Yue, M., Wei, X., and Li, Z. (2014). Adaptive sliding-mode control for two-wheeled inverted pendulum vehicle based on zero-dynamics theory. *Nonlinear Dynamics*, **76**(1), 459–471.

Yue, M., An, C., and Sun, J. (2016). Zero dynamics stabilisation and adaptive trajectory tracking for wip vehicles through feedback linearisation and lqr technique. *International Journal of Control*, pages 1–10.

Yun, X., Bachmann, E. R., and McGhee, R. B. (2008). A simplified quaternion-based algorithm for orientation estimation from earth gravity and magnetic field measurements. *IEEE TRANSACTIONS ON INSTRUMENTATION AND MEASUREMENT*, **57**(3).

Zadeh, L. A. (1965). Fuzzy sets. *Information and control*, **8**(3), 338–353.

Zhang, T. and Liao, Y. (2017). Attitude measure system based on extended kalman filter for multi-rotors. *Computers and electronics in agriculture*, **134**, 19–26.

Zhang, X. and Xiao, W. (2018). A fuzzy tuned and second estimator of the optimal quaternion complementary filter for human motion measurement with inertial and magnetic sensors. *Sensors*, **18**(10), 3517.

Zhao, H., Zhang, L., Qiu, S., Wang, Z., Yang, N., and Xu, J. (2019). Pedestrian dead reckoning using pocket-worn smartphone. *IEEE Access*, **7**, 91063–91073.

Zhaoqin, G. (2012). *Development and control of an underactuated two-wheeled mobile robot*. Ph.D. thesis, National University Of Singapore.

Zhou, Y. and Wang, Z. (2016a). Motion controller design of wheeled inverted pendulum with an input delay via optimal control theory. *Journal of Optimization Theory and Applications*, **168**(2), 625–645.

Zhou, Y. and Wang, Z. (2016b). Robust motion control of a two-wheeled inverted pendulum with an input delay based on optimal integral sliding mode manifold. *Nonlinear Dynamics*, pages 1–10.

.1 Appendix: System dynamics equations

This section describes both the Lagrangian $\mathcal{L}$ of the system and the exact elements of matrices $M(q)$ and $V(q,\dot{q})$. The Lagrangian is given as:

$$\begin{aligned}\mathcal{L}(q) = &\sum_{i=1}^{2}\left(\frac{6m_w r^2 + m_b r^2}{8} + \frac{m_b l^2 r^2 \sin^2\theta_3 + J_{\mathcal{B}} r^2}{2d^2} + \frac{k^2 J_r}{2}\right)\dot{\theta}_i^2 \\ &+ \left(\frac{m_b l^2 + J_{\mathcal{A}}}{2} + k^2 J_r\right)\dot{\theta}_3^2 + \sum_{i=1}^{2}\left(\frac{m_b l r\cos\theta_3}{2} - k^2 J_r\right)\dot{\theta}_3\dot{\theta}_i \\ &+ \left(\frac{m_b r^2}{4} - \frac{m_b l^2 r^2 \sin^2\theta_3 + J_{\mathcal{B}} r^2}{d^2}\right)\dot{\theta}_1\dot{\theta}_2 \\ &- 2m_w g r - m_b g\left(r - l\cos\theta_3\right).\end{aligned} \tag{1}$$

The elements of the inertia matrix $M(q) = (m_{ij})_{3\times 3}$ are:

$$\begin{aligned} m_{11} &= \frac{3}{2}m_w r^2 + \frac{1}{4}m_b r^2 + k^2 J_r + \frac{l^2 r^2}{d^2}m_b \sin^2\theta_3 + J_{\mathcal{B}}\frac{r^2}{d^2}, \\ m_{22} &= m_{11}, \quad m_{33} = m_b l^2 + J_{\mathcal{A}} + 2k^2 J_r, \\ m_{12} &= m_{21} = \frac{1}{4}m_b r^2 - \frac{l^2 r^2}{d^2}m_b \sin^2\theta_3 - J_{\mathcal{B}}\frac{r^2}{d^2}, \\ m_{13} &= m_{23} = m_{31} = m_{32} = \frac{1}{2}m_b l r\cos\theta_3 - k^2 J r. \end{aligned} \tag{2}$$

Similarly, the elements of the vector $V(q,\dot{q}) = (v_1, v_2, v_3)^T$ are:

$$\begin{aligned} v_1 &= 2\frac{l^2 r^2}{d^2}m_b \sin\theta_3\cos\theta_3\dot{\theta}_3\left(\dot{\theta}_1 - \dot{\theta}_2\right) - \frac{1}{2}m_b l r\sin\theta_3\dot{\theta}_3^2, \\ v_2 &= 2\frac{l^2 r^2}{d^2}m_b \sin\theta_3\cos\theta_3\dot{\theta}_3\left(\dot{\theta}_2 - \dot{\theta}_1\right) - \frac{1}{2}m_b l r\sin\theta_3\dot{\theta}_3^2, \\ v_3 &= -\frac{l^2 r^2}{d^2}m_b \sin\theta_3\cos\theta_3\left(\dot{\theta}_1 - \dot{\theta}_2\right)^2 + m_b g l\sin\theta_3. \end{aligned} \tag{3}$$